Project No. 10-875

Failure Predictions for VHTR Core Components using a Probabilistic Continuum Damage Mechanics Model

Reactor Concepts RD&D

Dr. Alex Fok
University of Minnesota

William Corwin, Federal POC
William Windes, Technical POC

NEUP Nuclear Energy University Programs
U.S. Department of Energy

FAILURE PREDICTIONS FOR VHTR CORE COMPONENTS USING A PROBABILISTIC CONTINUUM DAMAGE MECHANICS MODEL

Covering Period: September 01, 2010 – August 30, 2013

Date of Report: October 30, 2013

Recipient: University of Minnesota, Twin Cities

Minneapolis MN 55455

Contract Number: 101845

Project Number: 10-875

Principal Investigator: Alex Fok

TPOCs: William Windes

Federal POC: William Corwin

Project Objective: This project aims to address the key research need for the development of constitutive models and overall failure models for graphite and high temperature structural materials, with the long-term goal being to maximize the design life of the Next Generation Nuclear Plant (NGNP). To this end, the capability of Continuum Damage Mechanics (CDM) based models, which have been used successfully for modeling fracture of virgin graphite, will be extended as a predictive and design tool for the core components of the Very High Temperature Reactor (VHTR). Irradiation and environmental effects pertinent to the VHTR will be incorporated into the model to allow fracture of graphite and ceramic components under in-reactor conditions to be modeled explicitly using the finite element method. To reduce the arbitrariness and uncertainties associated with the current statistical approach, Monte Carlo analysis will be performed to address inherent variations in material properties. The results will potentially contribute to the current development of ASME codes for the design and construction of VHTR core components.

Abstract

When exposed to fast neutron irradiation, the graphite components in a Very High Temperature Reactor (VHTR) will undergo dimensional and physical property changes which may restrict the movement of control rods through the nuclear reactor core and produce stresses that undermine the structural integrity of the entire reactor core. Thus, it is imperative to assess the irradiation-induced stresses in the VHTR graphite components and the failure they may be caused.

Since graphite is a brittle material, its fracture properties show large variation. As a result, a probabilistic approach is required for the structural integrity analysis of graphite components. To determine the statistical parameters of graphite's fracture properties, three-point-bend tests were conducted on notched and un-notched beams of graphite. The dependence of the bulk fracture properties on the size of the graphite specimens was also studied through both experimental work and numerical simulation. Constitutive models for predicting the stresses in graphite components under irradiation were constructed and implemented in the finite element (FE) software ABAQUS using its user material subroutine (UMAT). The stress distributions in the components and their variations with time were determined from FE simulations. The Extended Finite Element Method (XFEM) was employed for modeling the failure of these components. The method was integrated with the UMAT on a common computational platform for modeling explicitly irradiation-induced failure of the components under in-reactor conditions. Monte Carlo failure analyses were performed to determine the failure probability of the components as a function of time. The developed UMAT was extended for performing stress analysis of VHTR components made of composite materials. The mechanical properties of a candidate composite were determined through nano-indentation and finite element simulation based on models created with Micro-computed tomography images.

The work addressed the key research need for the development of constitutive models and failure models for graphite, with the long-term goal being to maximize the design life of the Next Generation Nuclear Plant (NGNP). The results can potentially reduce the uncertainties and design margins associated

with the existing approaches and can contribute to the current development of ASME codes for the design and construction of VHTR core components.

Table of Contents

ABSTRACT 2

1. INTRODUCTION 8

1.1 Tasks 8

1.2 References 10

2. EVALUATION OF FRACTURE STATISTICS OF GRAPHITE 11

2.1 Methods 11

2.3 Fracture Toughness Results 13

2.4 Size Effect Results 15

2.5 Flexural Strength Results 18

2.6 References 21

3. VALIDATION OF CDM MODEL AND EXTENSION OF UEL FOR GRAPHITE 22

3.1 CDM Failure Model and the UEL 22

3.2 Study of Dependence of Statistical Parameters on Strain Gradient 25

3.2.1 Monte Carlo Analysis 26

3.2.2 Results and Conclusion 26

3.3 Failure Prediction of a SENB Specimen 28

3.3.1 Fracture parameters 28

3.3.2 FE results 29

3.4 References 31

4. CONSTITUTIVE MODEL FOR GRAPHITE AND ITS IMPLEMENTATION IN FEM 33

4.1 Constitutive Model 33

4.2 Verification of UMAT 34

4.3 References 37

5. MODELING RESIDUAL STRESSES IN VHTR GRAPHITE COMPONENTS 38

5.1 Load and boundary conditions.....38

5.2 Simulation results.....40

5.3 References 44

5.4 Appendix 44

6. EXTENDED FINITE ELEMENT METHOD (XFEM) FOR MODELING FAILURE IN GRAPHITE 46

6.1 Modeling Crack Propagation Using XFEM 46

6.2 Assessing the Viability of XFEM.....49
6.2.1 Mesh Sensitivity of XFEM Crack.....50
6.2.2 Effect of Mesh Type on XFEM Crack.....51
6.2.3 Results.....52
6.2.3.1 Effect of mesh type.....52
6.2.3.2 Effect of mesh size 55

6.3 Verification of XFEM for Simulating 3D Fracture 59
6.3.1 Three Point-Bend Test.....59
6.3.2 Results.....60

6.4 Conclusion.....61

6.5 References 62

7. MONTE CARLO 2D FAILURE ANALYSIS OF VHTR CORE COMPONENTS 63

7.1 Monte Carlo 2D Failure Analysis of a Cylindrical Graphite Brick.....63
7.1.1 Methods.....63
7.1.2 Stresses and Fracture Prediction.....64
7.1.3 Results and Discussion.....66
7.1.4 Conclusion 70

7.2 Monte Carlo 2D Failure Analysis of a Prismatic Reflector Graphite Brick.....71
7.2.1 Methods.....71
7.2.2 Stresses and Fracture Prediction.....72
7.2.3 Results and Discussion.....74
7.2.3 2D Failure Analysis of Prismatic Reflector Brick (IG-11 Graphite).....78
7.2.3.1 Methods.....78
7.2.3.2 Results and Discussion.....78
7.2.4 Conclusion 80

7.3 References **80**

8. MONTE CARLO 3D FAILURE ANALYSIS OF VHTR CORE COMPONENTS 82

8.1 Monte Carlo 3D Failure Analysis of a Cylindrical Brick **82**
8.1.1 FE simulation 82
8.1.2 Results and Discussion 85
8.1.3 Summary 89

8.2 Monte Carlo 3D Failure Analysis of a Prismatic Reflector Brick **90**
8.2.1 FE Simulation 91
8.2.2 Results and Discussion 93
8.2.3 Summary 96

8.3 References **97**

9. CHARACTERIZATION OF MECHANICAL PROPERTIES OF COMPOSITE 98

9.1 Graphite Fiber Test **98**
9.1.1 Method 98
9.1.2 Results and discussion 99

9.2 Evaluation of Mechanical Properties of Composites Through Finite Element Simulation **102**
9.2.1 Micro-Computed Tomography 102
9.2.2 Young's modulus of a single tow 105
9.2.3 Finite element model 107
9.2.4 Prediction of Young's modulus 109

9.3 Prediction of Residual Stresses Within the Composite Caused by Shrinkage of Graphite Fibers **111**

9.4 References **112**

10. EXTENSION OF UMAT FOR COMPOSITES 113

10.1 Verification of UMAT for Composite **113**
10.1.1 Constitutive Relationship for a Composite Material 113
10.1.2 Verification of UMAT 114
10.1.2.1 Problem Set-Up 114
10.1.2.2 Comparison of Numerical and Analytical Solution 116
10.1.3 Summary 117

10.2 Stress Analysis of a Composite Control Rod **117**
10.2.1 Methods 117
10.2.2 Results and Discussion 121
10.2.3 Summary 124

10.3 References..... 125

10.4 Appendix..... 125

1. INTRODUCTION

Due to its excellent mechanical and thermal properties, graphite will be used in the reactor core of the Very High Temperature Reactor (VHTR) where it serves as a moderator, reflector and structural material. Graphite has its limitations, though. When exposed to fast neutron irradiation, its dimensions and physical properties change. Because different parts of the VHTR components are located at different distances relative to the fuel elements, the changes occurring in their dimensions and physical properties are also different. It leads to development of stresses and possible failure of the components which can have serious implications to the safe operation of the VHTR. It is therefore important to be able to accurately predict the failure of these components.

Due to large variations in the failure properties (strength, fracture toughness) of graphite, deterministic approaches to predict failure do not work well and probabilistic approaches are preferred. Typically, stresses are predicted using a suitable constitutive model which defines the relationship between stresses and strains. The Weibull model is then used to calculate the failure probability of the component based on the predicted stress distribution [1]. Although the Weibull model is extensively used for this purpose, it has its shortcomings: (1) it does not handle stress concentrations well and overestimates the failure probability; and (2) the Weibull modulus, which is supposed to be a material constant, is actually dependent on the stress gradient [2]. Due to inaccuracy and uncertainties in the failure predictions, high safety margins will need to be used which increases the cost of the design and manufacturing of the components. Therefore, an alternative approach which can provide more accurate failure predictions is needed.

The work presented herein provides an alternative approach for predicting the failure probability of VHTR core components. The following tasks were conducted to accomplish the goals of the project.

1.1 TASKS

Task 1 - Evaluation of Fracture Statistics of Graphite. Experimental studies were conducted to measure the fracture toughness and the associated statistical properties of nuclear graphite NBG-18. Three-point-bending tests were conducted on single-edge notched beams to measure the fracture toughness. The digital image correlation (DIC) and acoustic emission (AE) techniques were also applied to monitor the damage evolution process during loading. In order to understand the effect of specimen size on the fracture toughness, specimens of three different sizes were employed in the three-point-bending tests. The flexural strength and its statistical characteristics were also evaluated by conducting three-point-bending tests on un-notched beams of NBG-18 graphite. The results were used for the probabilistic failure analysis of NBG-18 graphite components.

Task 2 - Validation using Virgin Graphite Tests. This task included validation of the Continuum Damage Mechanics (CDM) model and extension of the user-defined element (UEL) subroutine for the CDM model for graphite to include irradiation effects on the failure parameters, such as the fracture strength, critical strain energy release rate, the strain-softening parameter and their statistical variations. A Monte Carlo analysis was performed on the fracture simulation of L-shape specimens using the CDM

model, to see whether it can reproduce the reduced variation in the failure load (or increased Weibull modulus) with increasing strain concentration. Also, the failure of a single-edge-notched beam (SENB) with different irradiation histories was simulated.

Task 3 - Constitutive Models for Irradiated Graphite. Constitutive models for the irradiative behavior of nuclear graphite were constructed as User Material (UMAT) subroutines in ABAQUS. The strain components of the model included the irradiation-induced dimensional change strain, thermal strain, creep strain and elastic strain. Changes of the dimensions and material properties (Young's modulus, creep coefficient and coefficient of thermal expansion, etc.) with irradiation dose and temperature was incorporated based on existing data for VHTR candidate materials and other nuclear grade graphites which are available in the literature.

Task 4 - Modeling Residual Stresses in VHTR Graphite and Ceramic Components. The developed UMAT was verified for accuracy by simulating stresses in a section of a cylindrical graphite brick subjected to irradiation and comparing the predicted stresses with those reported in the literature. UMAT was employed to perform the stress analysis of a VHTR component.

Task 5 – Extended Finite Element Method for Failure Analysis. The new failure modeling technique, the Extended Finite Element Method (XFEM), has several advantages over the previous technique of failure modeling based on user-defined interface elements (UEL). Therefore, the UEL was replaced by XFEM for modeling failure of VHTR components. First, viability of the XFEM for modeling failure in graphite was assessed by using it to simulate standard three-point-bend tests. The simulation results were compared with the experimental results. Then, dependence of the simulated crack propagation on the mesh type and mesh size was studied. Through these tests, the accuracy and robustness of XFEM was evaluated.

Task 6 - Monte Carlo 2D Failure Analysis of VHTR Core Components. The XFEM was combined with the UMAT subroutine in ABAQUS to model explicitly the irradiation-induced fracture of VHTR components under in-reactor conditions. To account for the variations in the fracture properties of graphite, random properties based on the Weibull distribution were generated and assigned to create 2D component models with varying fracture properties. A Monte Carlo analysis was performed with these models and the failure probability was determined as a function of time.

Task 7 - Monte Carlo 3D Failure Analysis of VHTR Core Components. In this task, the failure modeling of VHTR core components was extended from 2D to 3D. To accomplish this step, the viability of XFEM for modeling graphite failure in 3D was assessed first by simulating three-point-bend test of graphite and comparing it with the experimental results. Thereafter, Monte Carlo 3D failure analyses were carried out to provide the failure statistics of VHTR components.

Task 8 – Implementation of Constitutive Models for Composites in UMAT. The UMAT subroutines, which were developed for graphite, were extended for predicting the mechanical behavior of a composite material (C-C or SiC-SiC) under irradiation. This required increasing the number of material parameters to account for anisotropy in composites. The UMAT was verified by modeling the mechanical behavior of a plate under irradiation and comparing the numerical solution with the analytical solution.

Task 9 - Mechanical Characterization of Composites. The mechanical properties of the graphite fibers (Young's modulus and hardness) of a C/C composite were evaluated through nano-indentation. A finite element (FE) model for a C/C woven composite was then developed and employed to predict the bulk mechanical properties of the composite and its internal stresses caused by dimensional changes of the carbon fibers resulted from neutron irradiation. The relative amounts of fiber and matrix were determined through Micro-computed tomography.

1.2 REFERENCES

1. Suyuan Yu, H. Li, C. Wang and Z. Zhang, Probability assessment of graphite brick in the HTR – 10, Nuclear Engineering and Design, 227, 133 – 142, (2004).

2. B.C. Mitchell, J. Smart, S.L. Fok and B.J. Marsden, The Mechanical Testing of Nuclear Graphite, Journal of Nuclear Materials, 322, 126-137, 2003.

2. EVALUATION OF FRACTURE STATISTICS OF GRAPHITE

The fracture strength of graphite and its variation as determined by flexural tests have been widely reported, with the associated Weibull modulus ranging from 10 to 20. There is far less information on the statistical variation of its fracture toughness or critical strain energy release rate. This information is required to be used to predict the failure probability of graphite components.

Experimental studies were conducted to measure the fracture toughness and the associated statistical properties of nuclear graphite NBG-18. Three-point-bending tests were conducted on single-edge notched beams to measure the fracture toughness. The digital image correlation (DIC) and acoustic emission (AE) techniques were also applied to monitor the damage evolution process during loading. In order to understand the effect of specimen size on the fracture toughness specimens of three different sizes were employed in the three point bending tests.

Flexural strength and its statistical characteristics were also evaluated by conducting three-point bending tests on un-notched beams of NBG-18 graphite. The results were used for the probabilistic failure analysis of NBG-18 graphite components

2.1 METHODS

Three groups of NBG-18 specimens with different dimensions were prepared. Figure 2.1 shows schematically the single-edge-notched beam (SENB). The dimensions of specimen in each group are listed in Table 2.1.

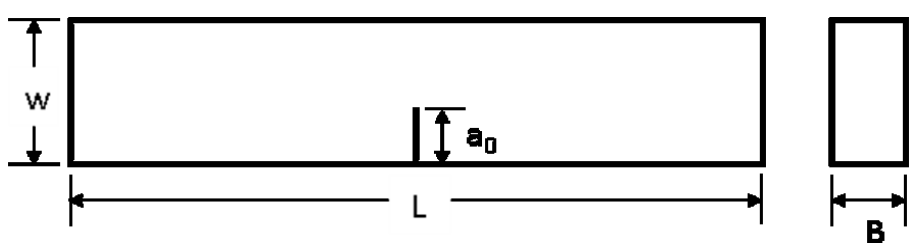

Figure 2.1 Schematic diagram of single-edge-notched beam

Table 2.1 Dimensions of the 3 groups of SENB specimens

Group	Number of specimens	L(mm)	w(mm)	B(mm)	a_0(mm)	Load Span S_0(mm)
I	26	220	50	25	21	200
II	20	110	20	10	8	100
III	19	45	10	5	4	40

Three-point-bending tests were conducted in a universal MTS test machine (858 Mini Bionix II, MTS, US). The test setup is shown in Figure 2.2. A compressive load was first applied to a specimen under stroke-control with a speed of v_{stroke} until the load reached a subcritical level of P_{stroke}. Afterwards, it was loaded to failure by controlling the crack mouth opening displacement (CMOD) with a rate of v_{cmod}. The loading parameters v_{stroke}, P_{stroke} and v_{cmod} for all specimens are listed in Table 2.2. Note that two different load speeds were applied to the specimens in Group II to study the influence of load speed on the measured fracture toughness. The CMOD was measured by an extensometer (Model 632.130-20, MTS, USA). The recorded data included time, load, stroke and CMOD.

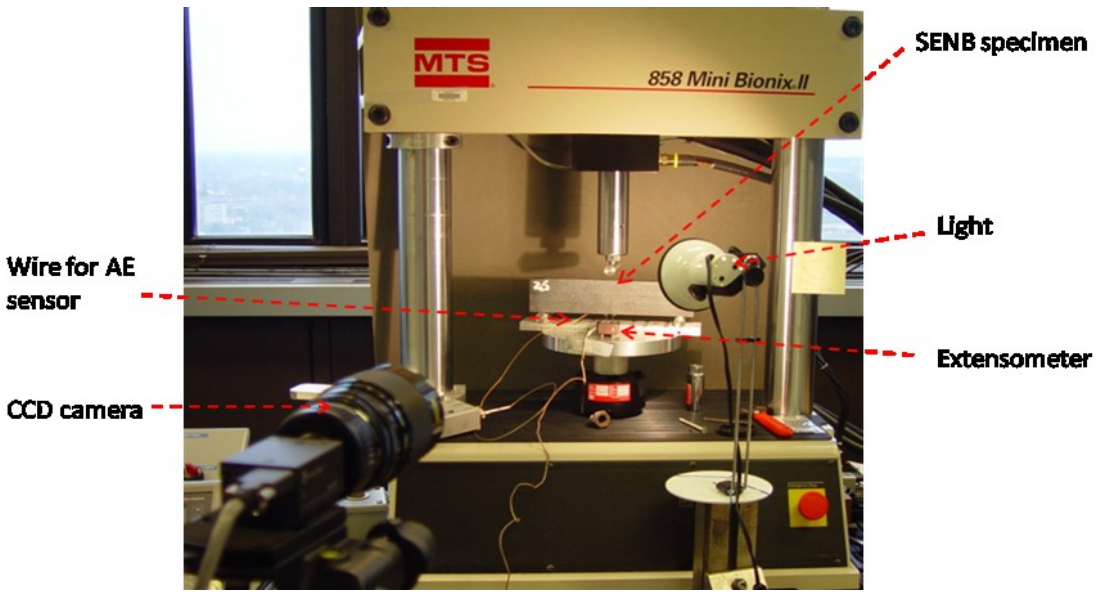

Figure 2.2: Setup of the three-point-bending test with a specimen in position

Table 2.2 Loading parameters

Group	v_{stroke} (mm/s)	P_{stroke} (N)	v_{cmod} (mm/s)
I	0.02	500	0.0025
II-a *1	0.02	100	0.0025
II-b *2	0.01	100	0.0015
III	0.005	40	0.0015

Notes: *1 for the first 10 specimens in Group II; *2 for the remaining 10 specimens in Group II.

The fracture toughness K_{IC} was calculated according to the following equations [1]:

$$K_{IC} = g \times \left[P_{max} \times S_0 \times \frac{10^{-6}}{Bw^{\frac{3}{2}}}\right] \times [3 \times \left(\frac{a}{w}\right)^{\frac{1}{2}} / (2 \times (1 - a/w)^{3/2})] \tag{2.1}$$

where

$$g = 1.9381 - 5.0947*(a/w) + 12.386*(a/w)^2 - 19.2142*(a/w)^3 + 15.7747*(a/w)^4 - 5.1270*(a/w)^5 \quad (2.2)$$

where P_{max} is the maximum load, S_0 is the load span, a is the notch length and B and w are the thickness and width of the specimen, respectively.

Flexural strength and its statistical characteristics were evaluated by conducting three-point bending tests on un-notched beams of NBG-18 graphite Twenty-four beam specimens with the dimensions of 114mm(L)x20mm(W)x10mm(H) were machined from the broken halves of the specimens used in the fracture toughness test conducted earlier. This was justified because the material away from the notched section had been subjected to a very low load. The support span for the three-point bending test was 100mm. The test was conducted on the same MTS test machine (858 Mini Bionix II, MTS, US) used for the fracture toughness test. The load was applied under stroke control with a speed of 0.02mm/s.

2.3 FRACTURE TOUGHNESS RESULTS

Table 2.3 lists the mean, standard deviation and Weibull parameters for the failure load and fracture toughness KIC. The calculated KIC was higher than the average fracture toughness of nuclear graphite which is around 1.0MPa·m1/2[2]. This might be caused by the finite notch root radius [3]. Efforts will be made to correct for this and other factors that may influence the KIC value.

Table 2.3: The mean value, standard deviation (std) and Weibull parameters ($\bar{\sigma}$ and m) for the maximum failure load and fracture toughness

	Mean (std)	Weibull parameter $\bar{\sigma}$ and m
Max failure load F_{max} (N)	1091.8 (23.61)	1103.9, m=41.1
Fracture toughness K_{IC} (MPa·m $^{1/2}$)	1.691(0.037)	1.710, m=41.1
Load for first AE event F_0 (N)	595.66 (81.3)	630.07, m=7.7

Fig. 2.3 shows the load vs. crack mouth opening displacement (CMOD) for the large sized specimens

Fig. 2.4 shows the strain field ε_{xx} around the notch tip of a specimen at different times of the loading process. These could provide more accurate measurements of the length of the propagating crack.

Fig. 2.5 shows the cumulative number of AE events against time for 11 specimens.

Fig. 2.6 plots the load, cumulative number of AE events and the amplitude of each AE event all together. The load for the first AE event was around 630N.

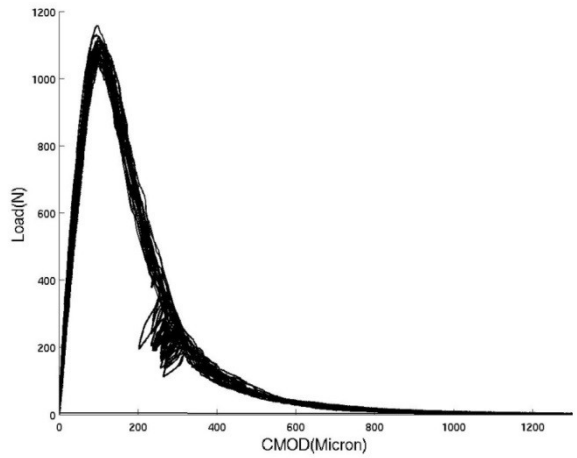

Fig. 2.3 Load vs. CMOD for all specimens

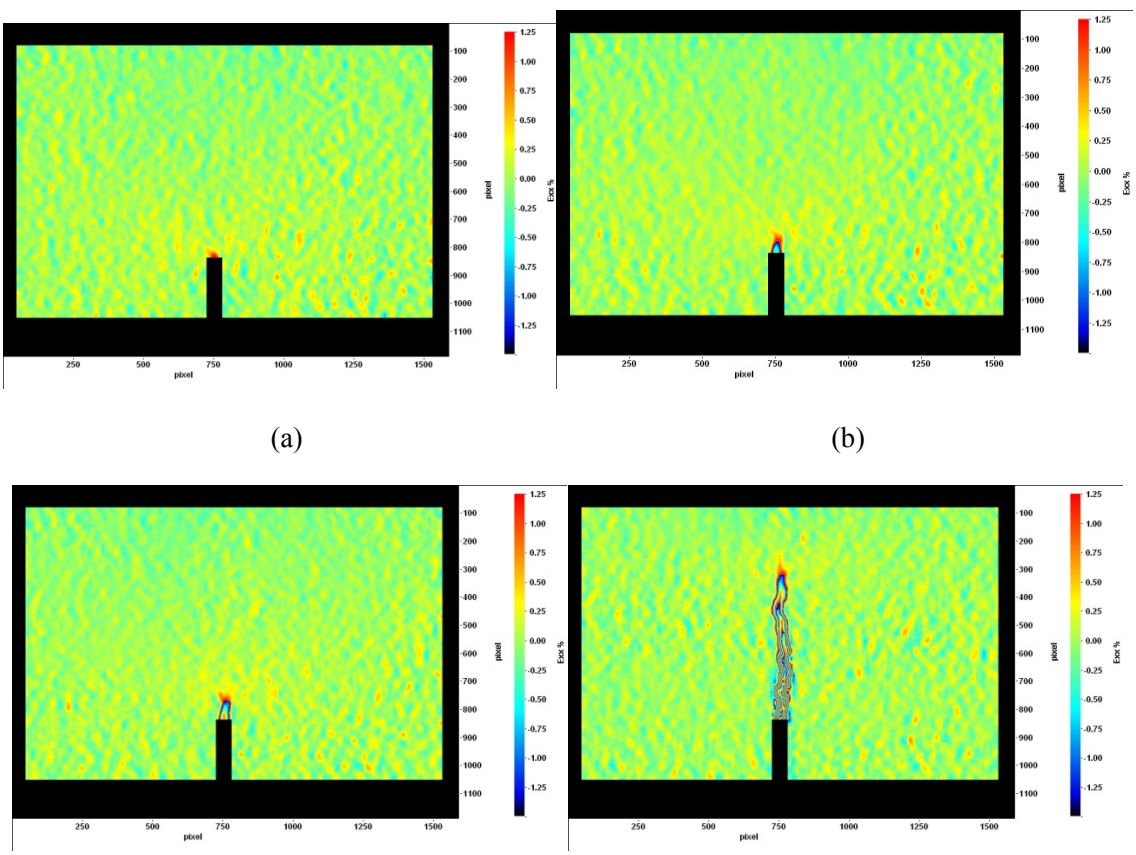

Fig. 2.4 Strain field ε_{xx} around the notch tip showing the damage evolution process

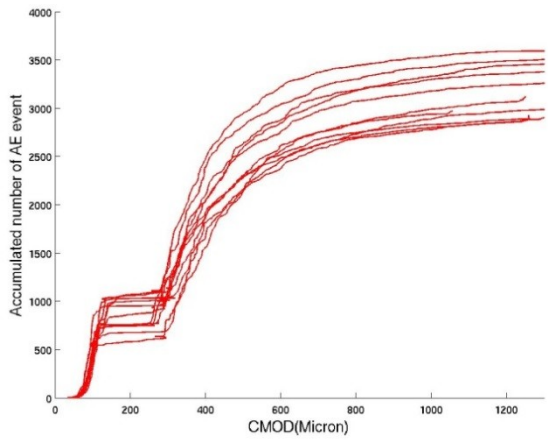

Fig. 2.5 Cumulative number of AE events vs. CMOD for 11 specimens

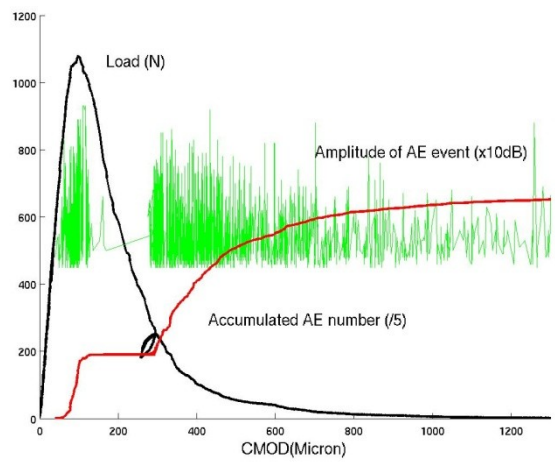

Fig. 2.6 Load, cumulative number of AE events and amplitude of each AE event vs. CMOD

2.4 SIZE EFFECT RESULTS

Figure 2.7 shows the load-displacement curves for all specimens. The maximum failure load and the fracture toughness and their statistical characteristics for each group are listed in Table 2.4. The Weibull plots of K_{IC} for the three groups are shown in Figure 2.8. They show that, with a decrease in the specimen size, the measured fracture toughness decreases, and the Weibull modulus *m* also decreases, indicating a bigger scatter in the results. The load speed did not seem to have a significant effect on the measured fracture toughness, but the lower load speed seemed to have caused a bigger scatter in the results.

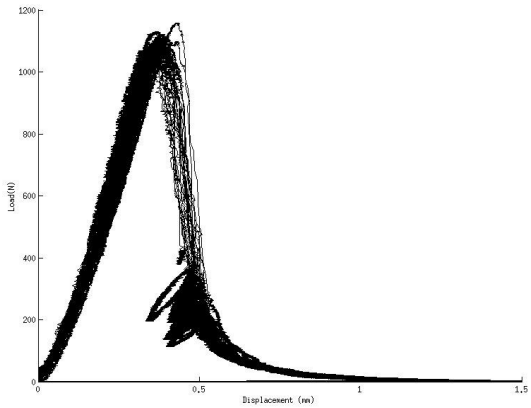

(a)

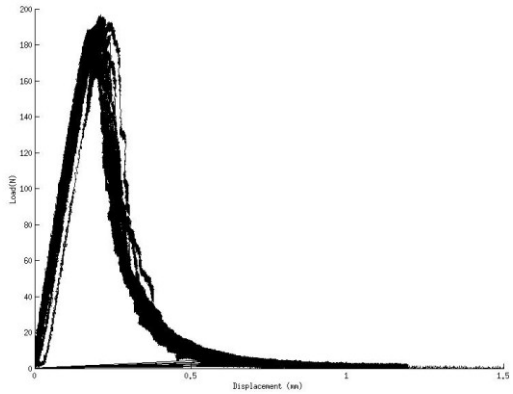

(b)

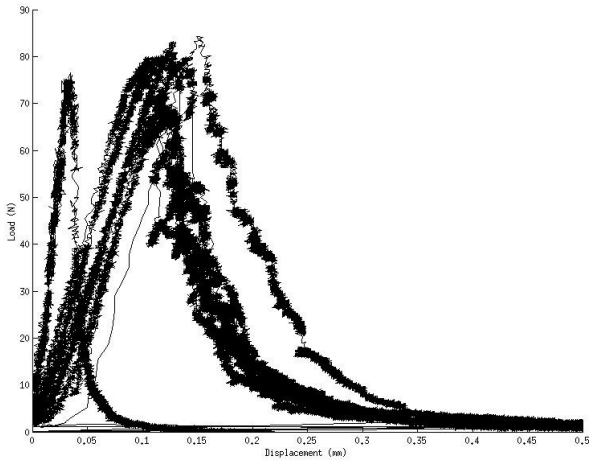

(c)

Figure 2.7: Load-displacement curves for all specimens: (a) Group I, (b) Group II and (c) Group III

Table 2.4 Test results – statistical characteristics of failure load and fracture toughness

Group	Failure load		K_{IC}	
	Mean, Std (N)	Weibull modulus *m*	Mean, Std ($MPa \cdot \sqrt{m}$)	Weibull modulus *m*
I	1092.8, 23.6	41.1	1.69, 0.04	41.1
II-a *[1]	188.2, 5.5	43.1	1.36, 0.04	43.1
II-b *[2]	186.5, 8.6	30.1	1.35, 0.06	30.1
II *[3]	187.4, 7.0	35.5	1.36, 0.05	35.5
III	77.6, 5.4	18.8	1.27, 0.09	18.1

Notes: *1 for the first 10 specimens in Group II;
*2 for the last 10 specimens in Group II;
*3 for all specimens in Group II.

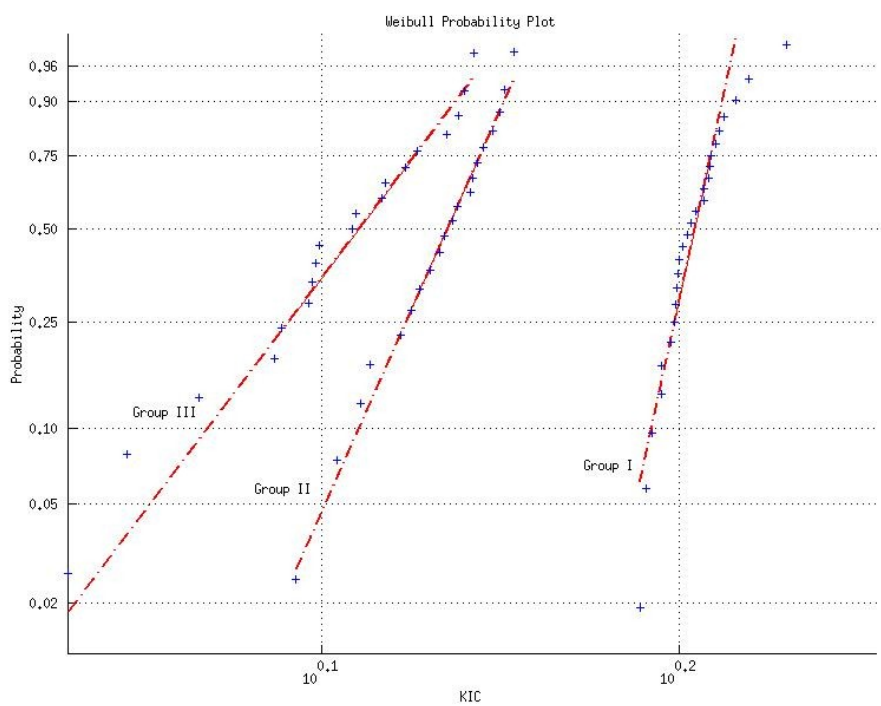

Figure 2.8: Weibull plot of K_{IC} for Groups I, II and III

2.5 FLEXURAL STRENGTH RESULTS

Figure 2.9 shows the fracture profiles of all the 24 specimens and Figure 2.10 shows the load-displacement curves. The maximum failure load and the flexural strength obtained are listed in Table 2.5. The mean and standard deviation of the flexural strength are 28.7MPa and 2.1MPa, respectively. The Weibull's modulus m is 15.6. Figures 2.11 and 2.12 show the Weibull plots of the failure load and flexural strength, respectively.

These results are similar with the values reported in Ref [2, 3], where the mean value of flexural strength of NBG-18 (~30MPa) and its Weibull's modulus *m* (10.0) were obtained through 4-point bending tests.

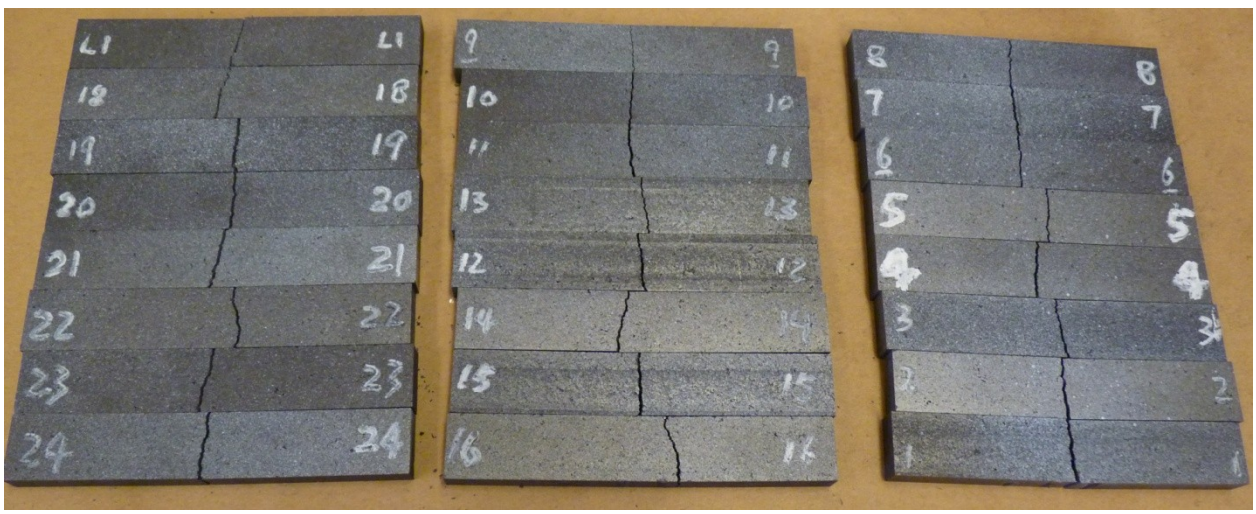

Figure 2.9: Fracture profiles of all specimens

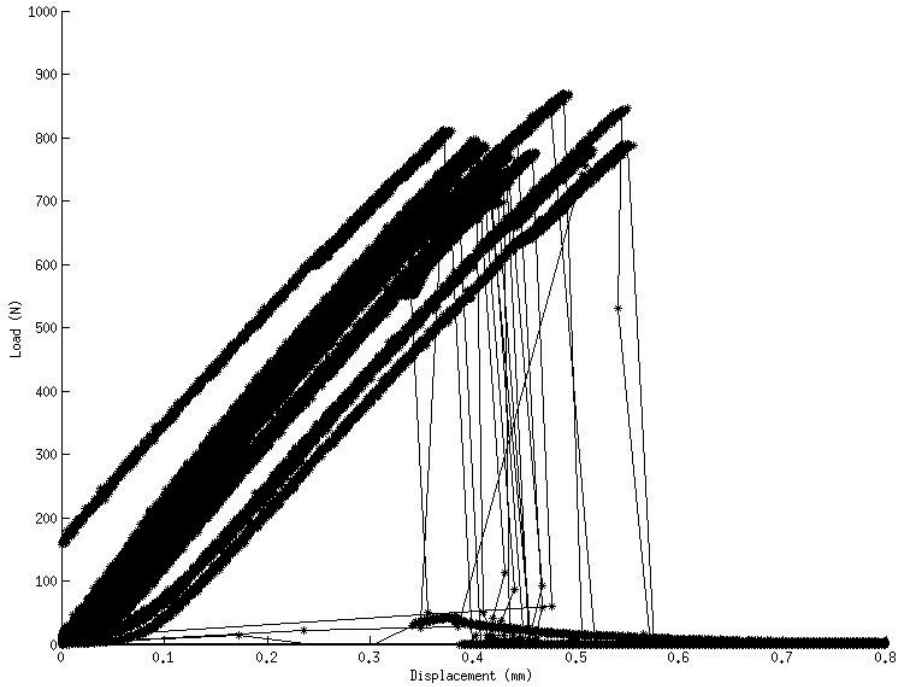

Figure 2.10: Load-displacement curves of all specimens

Table 2.5 Test results-failure load and flexural strength

	Failure load (N)	Flexural strength (MPa)
Mean	765.3	28.7
Std	56.7	2.1
Weibull Modulus m	15.6	15.6

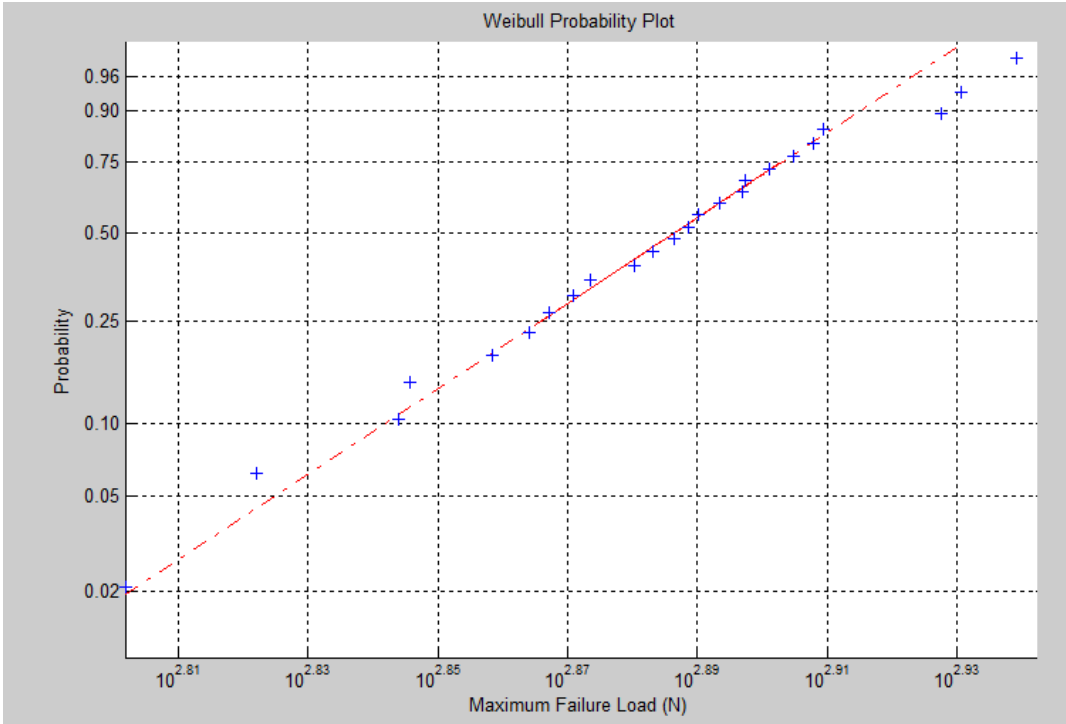

Figure 2.11: Weibull plot of the maximum failure load

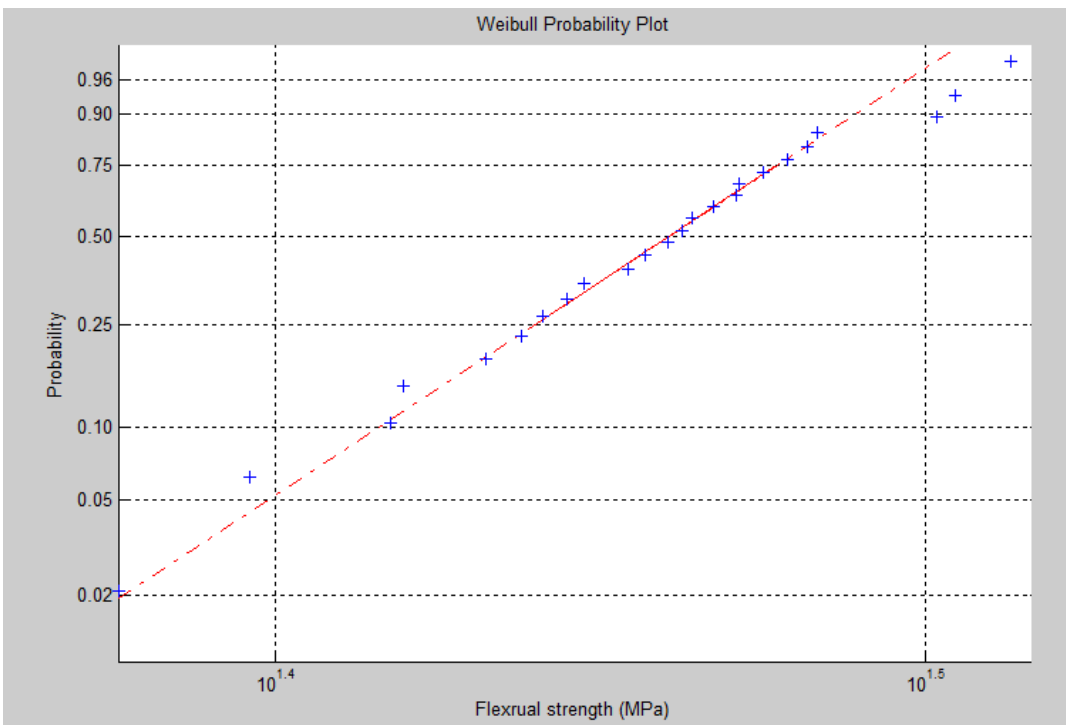

Figure 2.12: Weibull plot of flexural strength

2.6 REFERENCES

[1] Haiyan Li and Alex Fok, Fracture Toughness Measurement of NBG-18 by Three Point Bending Test, First quarterly report of NEUP project: 'Failure Prediction for VHTR Core Components using a Probabilistic Continuum Damage Mechanics Model', NEUP-00101845, April 2010.

[2] M Fechter, S Fazluddin, Characterisation of NBG-18 Graphite for the PBMR Demonstration Power Plant, 9th INGSM, September 2008, Netherlands.

[3] Haiyan Li and Alex Fok, Material properties of NBG-18, First quarterly report of NEUP project: 'Failure Prediction for VHTR Core Components using a Probabilistic Continuum Damage Mechanics Model', NEUP-00101845, April 2010.

3. VALIDATION OF CDM MODEL AND EXTENSION OF UEL FOR GRAPHITE

This study aimed to validate the CDM model and extend the user-defined element (UEL) subroutine for the Continuum Damage Mechanics (CDM) model for graphite [1,2] to include irradiation effects on the failure parameters [4-6], such as the fracture strength, critical strain energy release rate, the strain-softening parameter and their statistical variations.

A Monte Carlo analysis was performed on the fracture simulation of the L-shape specimens using the CDM model, to see whether it can reproduce the reduced variation in the failure load (or increased Weibull modulus) with increasing strain concentration.

The failure of a single-edge-notched-beam (SENB) with different irradiation histories was simulated. The material was assumed to be IG-11 and the fracture parameters were based on the data from references [4-6].

3.1 CDM FAILURE MODEL AND THE UEL

In order to simulate the fracture initiation and propagation, an interface is introduced into the continuum solid where potential crack surfaces may form. The interface has no thickness and there is no gap within it before damage is incurred. Figure 3.1 schematically shows the transition of an interface, via a damage process zone, to fully formed crack surfaces. To derive the constitutive law for the interface in 2D, a dimensionless damage parameter ω is employed, namely

$$\tau_i = k_i^0 (1-\omega)\delta_i, \quad \text{i=1,2} \tag{3.1}$$

where τ_i are the tractions on the interface, δ_i the relative displacements across the interface, and k_i^0 the constraint stiffness values of the interface. Subscript 1 indicates the direction normal to the interface and 2 the direction along the interface. ω=0 indicates no damage, and ω=1 indicates the fully cracked state. Incrementally,

$$\mathrm{d}\tau_i = k_i^0 (1-\omega)\mathrm{d}\delta_i - k_i^0 \delta_i \mathrm{d}\omega, \quad \text{i=1,2} \tag{3.2}$$

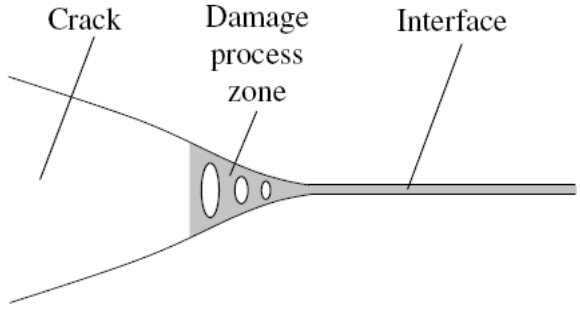

Figure 3.1: Transition of an interface, via a damage process zone, to a fully formed crack

A damage surface, which is based on both a stress-based (τ_i) and a fracture-mechanics-based (G_i) failure criterion, is constructed for establishing the damage evolution law as below:

$$F(\tau_i, G_i) = \left(\frac{\tau_1^2}{\tau_{1C}^2} + \frac{\tau_2^2}{\tau_{2C}^2} \right) + \left(\frac{G_I}{G_{IC}} + \frac{G_{II}}{G_{IIC}} \right)^n - 1 = 0 \tag{3.3}$$

where G_i are the strain energy release rates of the material, defined as $G_i = \int_0^{\delta_i} \tau_i \mathrm{d}\delta_i$; G_{iC} are the critical values of G_i ; and n is a parameter which controls the rate of strain softening in the material.

When the combination of the interfacial stresses exceeds the damage surface, i.e. $F(\tau_i, G_i) > 0$, damage will develop at the interface. Thereafter, infinitesimal changes of the traction forces will result in an infinitesimal change of the damage state as follows:

$$\mathrm{d}F = \sum_{i=1}^{2} \left(\frac{\partial F}{\partial \tau_i} \mathrm{d}\tau_i + \frac{\partial F}{\partial G_i} \mathrm{d}G_i \right) = 0 \tag{3.4}$$

Substituting for $\mathrm{d}\tau_i$ and $\mathrm{d}G_i$ in terms of $\mathrm{d}\delta_i$, this gives

$$\mathrm{d}\omega = \sum_{i=1}^{2} \left[\frac{\partial F}{\partial \tau_i} (1-\omega) k_i^0 + \frac{\partial F}{\partial G_i} \tau_i \right] \mathrm{d}\delta_i \Bigg/ \sum_{j=1}^{2} \frac{\partial F}{\partial \tau_j} k_j^0 \delta_j \tag{3.5}$$

The incremental interfacial constitutive law can then be obtained by making use of Equations (3.2) and (3.5) as:

$$\mathrm{d}\tau_\mathrm{i} = k_i^0 (1-\omega) \mathrm{d}\delta_i - k_i^0 \delta_i \mathrm{d}\omega = k_i^0 (1-\omega) \mathrm{d}\delta_i - k_i^0 \delta_i \sum_{j=1}^{2} C_j \mathrm{d}\delta_j \tag{3.6}$$

where $C_i = \left[\frac{\partial F}{\partial \tau_i} (1-\omega) k_i^0 + \frac{\partial F}{\partial G_i} \tau_i \right] \Bigg/ \sum_{j=1}^{2} \frac{\partial F}{\partial \tau_j} k_j^0 \delta_j$.

When the interfacial stresses are within the damage surface, i.e. $F(\tau_i, G_i) < 0$, no damage is sustained, thus $d\omega = 0$ and the incremental constitutive law simplifies to:

$$\mathrm{d}\tau_{\mathrm{i}} = k_i^0 (1-\omega)\mathrm{d}\delta_i \tag{3.7}$$

Possible traction–relative displacement curves obtained from the above model are shown in Figure 3.2. By changing the softening parameter *n* in Eq. (3.3), different types of material degradation can be obtained.

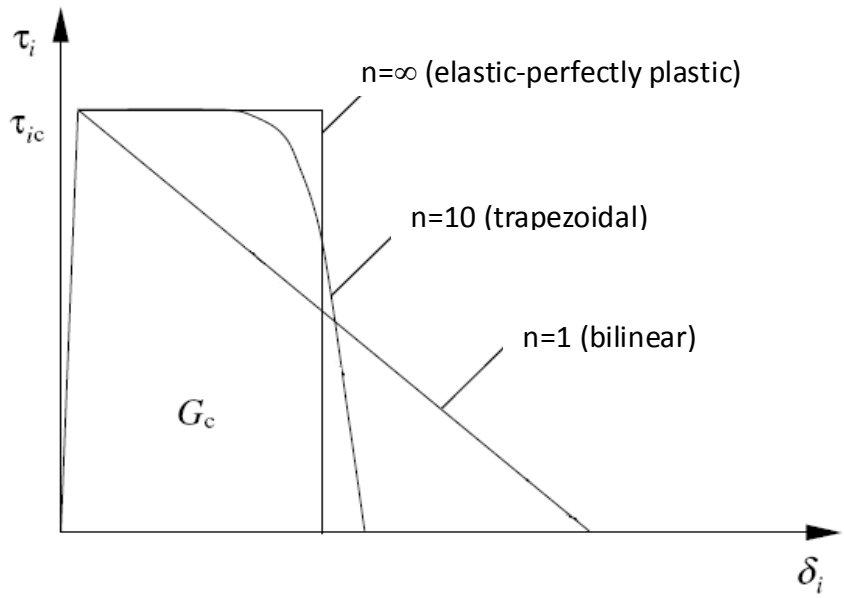

Figure 3.2 Traction–relative displacement curves with different softening parameters (n)

Further details of this CDM model can be found in References [1] and [2]. To implement it into FEA, interface elements with the above interfacial constitutive law were inserted into the boundaries between solid elements. The interface elements were defined through a user element (UEL) subroutine of ABAQUS [3]. Figure 3.5 shows the connections of an interface element with two solid elements. The interface element, which has a zero thickness before damage, shares the nodes at the interface with the two solid elements. The relative displacements across the interface at the position of the dual coincident nodes are simply the relative nodal displacements.

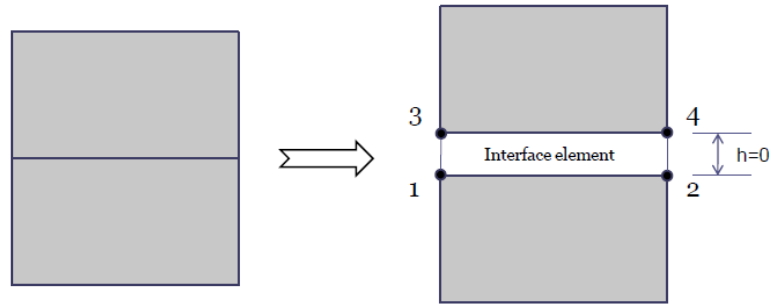

Figure 3.5: Interface element

3.2 Study of Dependence of Statistical Parameters on Strain Gradient

Brittle materials show scatter in their fracture properties. Probabilistic approach is used to for making failure predictions for components made up of brittle material. Weibull model is a probabilistic model based on Weakest link theory and has been extensively used for failure prediction of brittle materials. Equation 3.8 gives the expression for evaluating failure probability based on stress distribution.

$$P_f = 1 - \exp\left[-\int_V \left(\frac{\sigma}{\sigma_0}\right)^m \frac{dV}{V}\right] \qquad (3.8)$$

Fracture simulation of the graphite specimens was performed using the CDM model to check whether it can reproduce the reduced variation in the failure load (or increased Weibull modulus) with increasing strain concentration. Three different cases of graphite specimens were considered: 1) notched beams under three-point bending 2) un-notched beams under three-point bending and 3) L-shaped specimens under tension. The finite element models are shown in Figure 3.6.

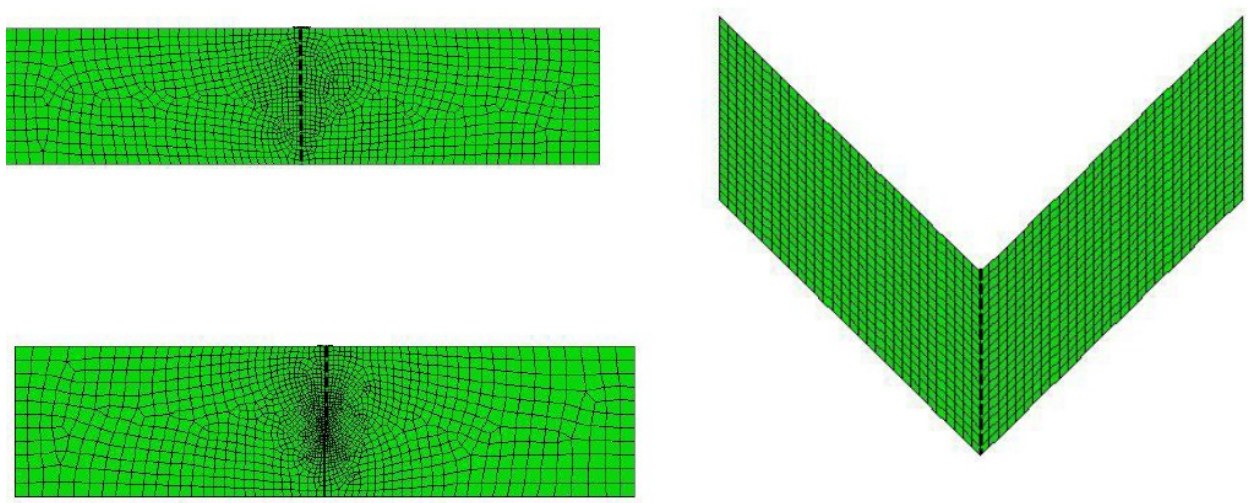

Figure 3.6: Un-notched graphite specimen under three-point bending (top left), notched graphite specimen under three-point bending (bottom left) and L-shaped specimen under tension (right).

3.2.1 Monte Carlo Analysis

A Monte Carlo analysis was performed for the failure simulations. Figure 3.7 delineates the process used for carrying out the analysis. The random sample of 30 sets of fracture properties (strength and fracture toughness) based on Weibull distribution was generated. Table 3.1 shows the Weibull parameters used for generating the random fracture properties.

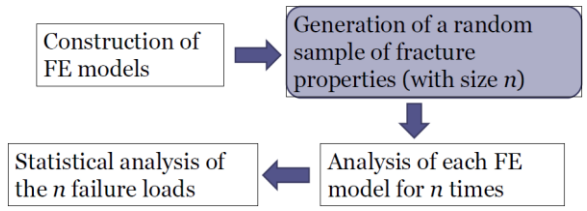

Figure 3.7: Steps in Monte Carlo analysis.

Table 3.1 Weibull mean and Weibull modulus used to generate random sample of fracture properties.

	Weibull mean	**Weibull modulus**
Fracture toughess (MPa √m)	1.11	33
Strength (MPa)	25	9

3.2.2 Results and Conclusion

The mean peak load, the corresponding Weibull modulus and standard deviation for the three tests were evaluated and are shown in Table 3.2. The Weibull plot is shown in Figure 3.8 and the evolution of damage with the progress of loading is shown in Figure 3.9.

Table 3.2 Mean peak load, Weibull modulus and the standard deviation for the three cases of loading.

	P_o(N)	m	std (N)
Notched beam	1006.0	16	69.2
L-shaped beam	1018.1	9.8	110.8
Unnotched beam	8561.8	9.3	973.2

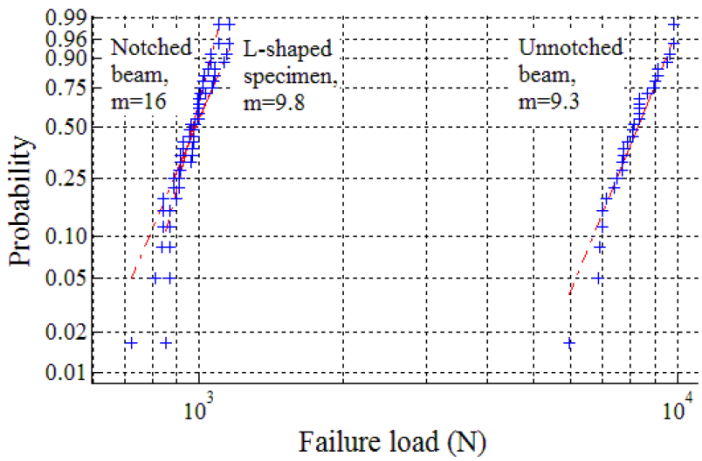

Figure 3.8: Weibull plot for the three cases of loading.

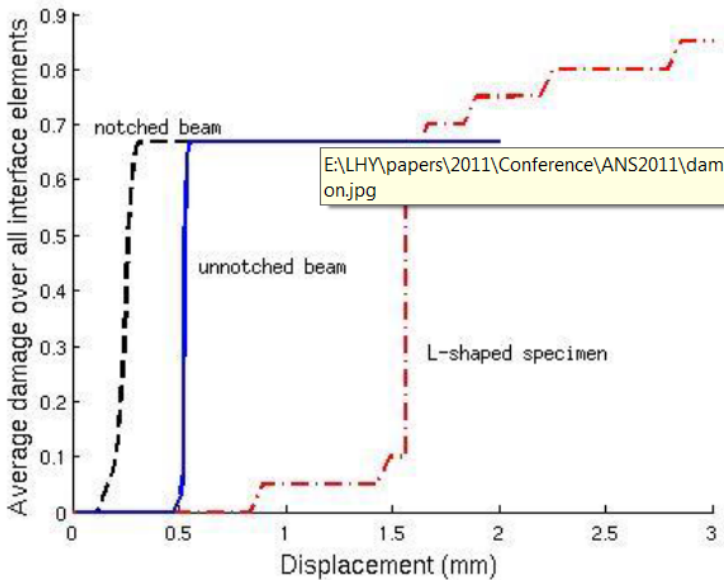

Figure 3.9: Damage evolution for the three cases of loading.

The Weibull modulus was found to be maximum (minimum spread) for notched beams under three-point bending which had the greatest strain gradient. For un-notched beams under three-point bending, which had smallest strain gradient, the Weibull modulus was found to be maximum (maximum spread). The results clearly showed that the strain gradient could affect the spread in the failure loads of nuclear graphite significantly.

3.3 FAILURE PREDICTION OF A SENB SPECIMEN

Figure 3.10 shows the FE model of the SENB specimen, which consists of 36 CPE3 and 1891 CPE4 plane-strain elements, as well as 39 user-defined interface elements [3]. The dimensions of the specimen were: Length=220 mm, Width=50 mm, Thickness=25 mm, Support span=200 mm, and Pre-crack length =21 mm. Constraints were applied at Points A, B and C (Y_A=Y_B=X_C=0, where Y is for vertical direction and X is for horizontal direction). At the same time, a vertical load was applied at Point C via prescribed displacement (Y_C = -0.8 mm).

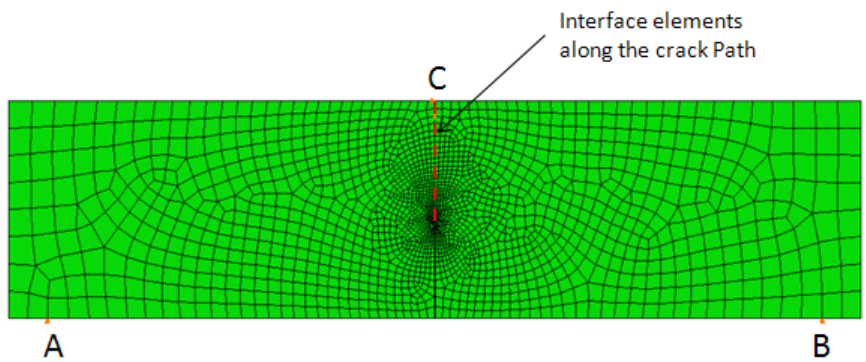

Figure 3.10 FE model of SENB specimen

3.3.1 Fracture parameters

The fracture parameters used in the UEL included: the strength τ_i, critical strain energy release rate G_i, and the softening parameter *n*, which is a reciprocal measure of the degree of strain-softening. Figure 3.11 shows the influence of neutron irradiation on the strength of IG-11 [6], which has a virgin value of 21.4 MPa. There were very limited experimental data on the fracture toughness of irradiated IG-11. According to the experimental results from Ref. [4, 5], where the IG-11 graphite has been exposed to low dose neutron irradiation of about (1~2)x10^{21} n/cm^2, the ratio of irradiated to virgin values for strength and fracture toughness were 1.23 and 1.29, respectively. Therefore, the critical strain energy release rate, which has a virgin value of 0.11x10^3 J/m^2, was assumed to have the same curve as strength, as shown in Figure 3.11. The softening parameter *n* was assumed to be a constant of 50. Young's modulus and Poisson's ratio were assumed to be constants of 9 GPa and 0.2, respectively.

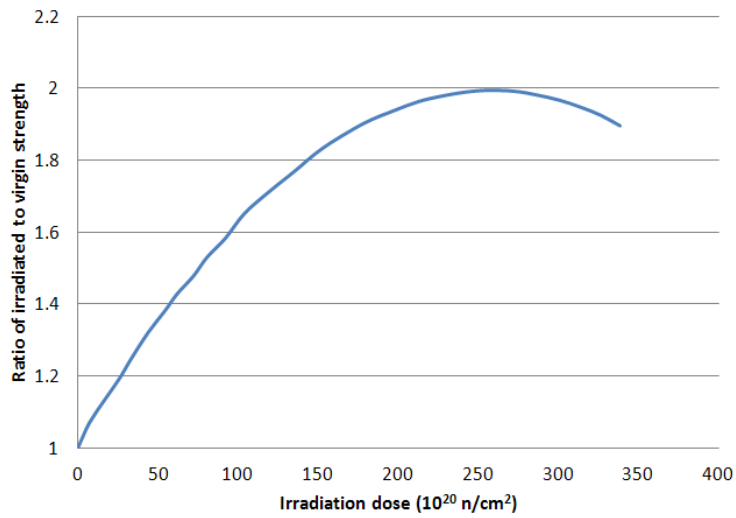

Figure 3.11 Ratio of irradiated to virgin strength of IG-11 against neutron irradiation dose

3.3.2 FE results

The failure of the SENB specimens with different irradiation histories was simulated. Figure 3.12 shows the failure process of the SENB specimen with an irradiation dose of 104×10^{20} n/cm^2. Figure 3.13 shows the load-displacement curves of the SENB specimens with different neutron irradiation doses.

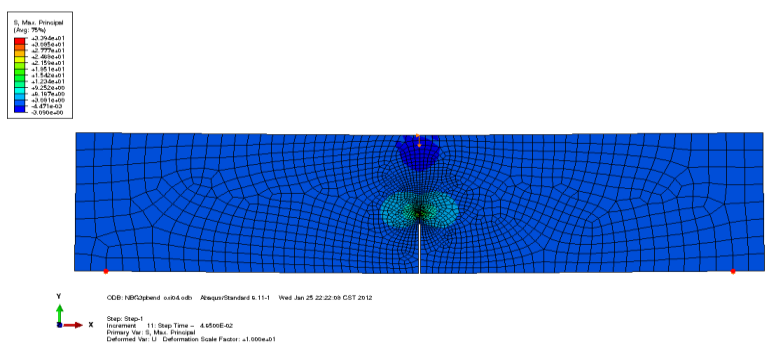

3.12 (a)

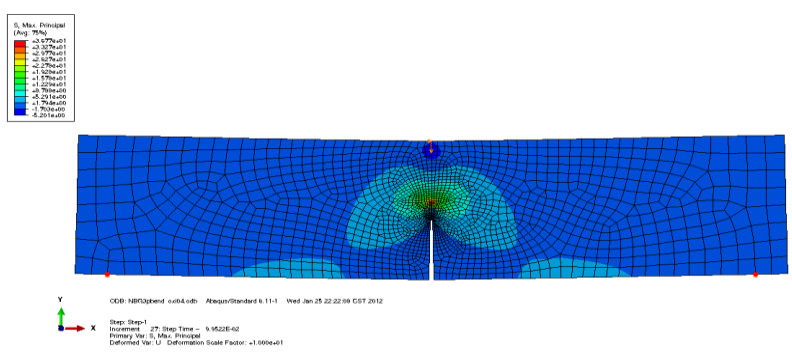

3.12 (b)

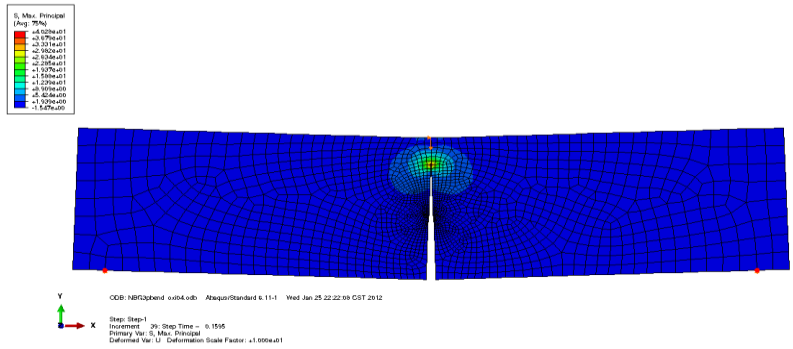

3.12 (c)

Figure 3.12 Failure process of the SENB specimen with an irradiation dose of 104×10^{20} n/cm^2: (a) Damage initiation, (b) Crack propagation and (c) Failure of the specimen. *[Note: deformations were magnified by a factor of 10.]*

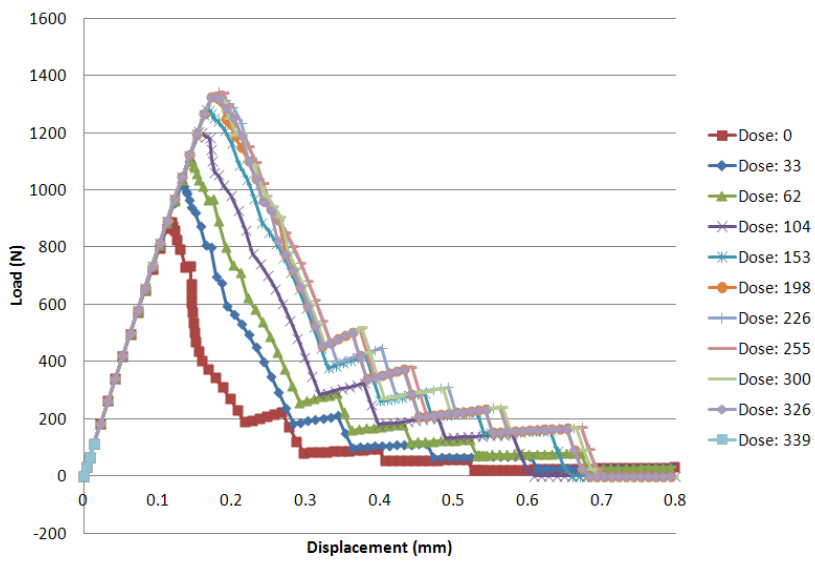

Figure 3.13 Predicted load-displacement curves of SENB specimens with different irradiation doses (10^{20} n/cm^2)

The predicted failure (maximum) loads of SENB specimens with different irradiation doses are plotted in Figure 3.14. Figure 3.15 shows the ratio of the irradiated to virgin failure load against the irradiation dose, together with that for the strength/fracture toughness as comparison. It can be seen that the increase in the failure load of the SENB specimen is lower than that in the un-notched specimens. Since the SENB specimen is used to measure the fracture toughness of graphite, this means that the predicted increase in the fracture toughness of graphite by irradiation is not consistent with that assumed.

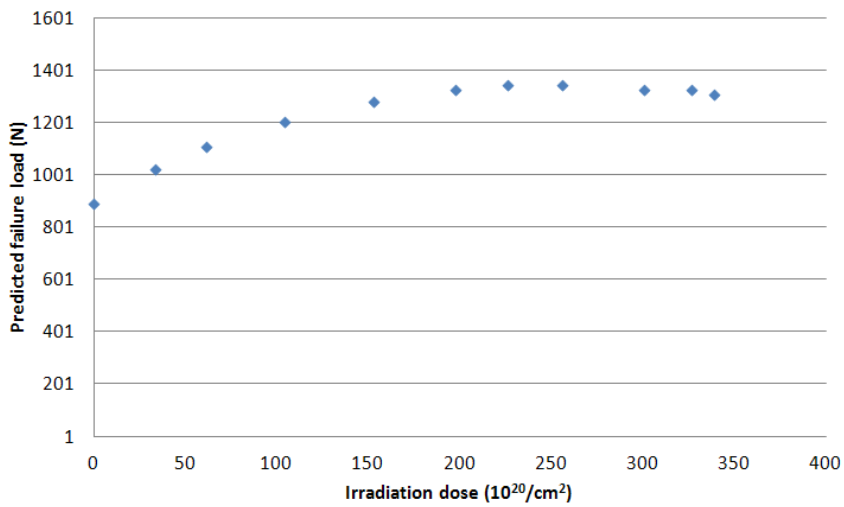

Figure 3.14 Maximum failure load against irradiation dose

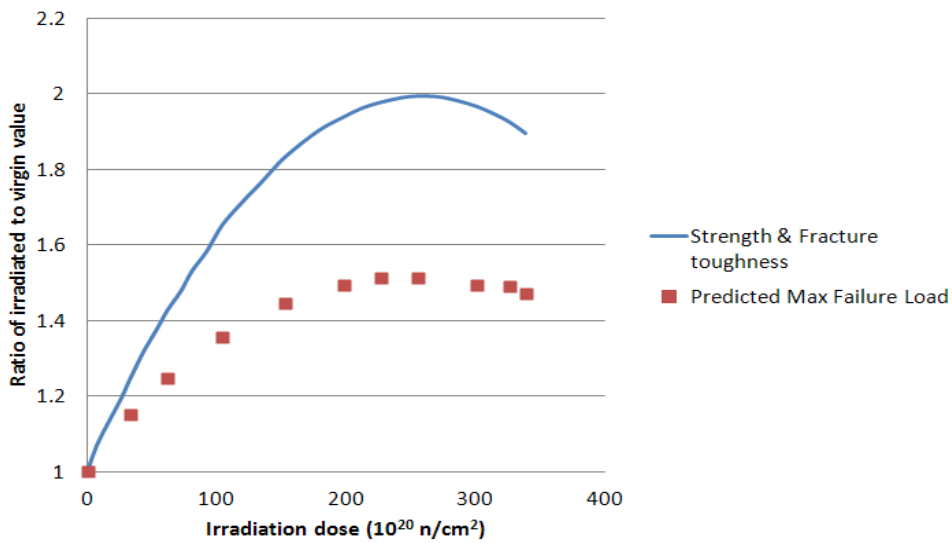

Figure 3.15 Influence of irradiation dose on the maximum failure load of the SENB specimen

3.4 REFERENCES

1) Z. Zou, A.S.L. Fok, S.O. Oyadiji, B.J. Marsden. Failure predictions for nuclear graphite using a continuum damage mechanics model. Journal of Nuclear Materials 324 (2004) 116–124.
2) Z. Zou, S.L. Fok , B.J. Marsden, S.O. Oyadiji, Numerical simulation of strength test on graphite moderator bricks using a continuum damage mechanics model, Engineering Fracture Mechanics 73 (2006) 318–330.

3) ABAQUS version 6.5 user's manuals, Pawtucket, RI, USA. Hibbett, Karlsson and Sorensen Inc. 2004
4) S. Sata, A. Kurumada and K. Kawamata, Neutron irradiation effects on thermal shock resistance and fracture toughness of graphites as plasma-facing first wall components for fusion reactor devices, Carbon, 27 (4) 507-516, (1989).

5) S. Sata, K. Kawamata, A. Kurumada, H. Ugachi and H. Awaji, Degradations of thermal shock resistance and the fracture toughness of reactor graphite subjected to neutron irradiation. JAERI-M 96-192.

6) S. Ishiyama, T.D. Burchell, J.P. Striazak and M. Eto, The effect of high fluence neutron irradiation on the properties of a fine – grained isotropic nuclear graphite, Journal of Nuclear Materials, 230, 1 -7, (1996).

4. CONSTITUTIVE MODEL FOR GRAPHITE AND ITS IMPLEMENTATION IN FEM

Constitutive model for the irradiation behavior of nuclear graphite under high temperature and irradiation was constructed and implemented as User Material (UMAT) subroutines in commercial finite element software ABAQUS. The strain components of the model included the irradiation-induced dimensional change strain, thermal strain, creep strain and elastic strain. Changes of the dimensions and material properties (Young's modulus, creep coefficient and coefficient of thermal expansion, etc.) with irradiation dose and temperature were based on existing data for VHTR candidate materials available in the literature. The UMAT was verified by making the numerical predictions for the stresses in a cylindrical AGR (Advanced Gas-Cooled Reactor) graphite brick using UMAT and comparing it with the analytically evaluated stresses.

4.1 CONSTITUTIVE MODEL

The constitutive model for the irradiation behavior of nuclear graphite was constructed. The main equations of the model include:

$$\Delta\boldsymbol{\varepsilon}^{total} = \Delta\boldsymbol{\varepsilon}^{e} + \Delta\boldsymbol{\varepsilon}^{pc} + \Delta\boldsymbol{\varepsilon}^{sc} + \Delta\boldsymbol{\varepsilon}^{dc} + \Delta\boldsymbol{\varepsilon}^{th} \quad (4.1)$$

$$\boldsymbol{\sigma} = \mathbf{D}\boldsymbol{\varepsilon}^{e} \quad (4.2)$$

$$\Delta\boldsymbol{\sigma} = \check{\mathbf{D}}\Delta\boldsymbol{\varepsilon}^{e} + \Delta\mathbf{D}\boldsymbol{\varepsilon}^{e} \quad (4.3)$$

$$\boldsymbol{\varepsilon}^{pc} = 4.0\exp(-4\gamma)\int_0^{\gamma}\frac{\sigma}{E_c}\exp(4\gamma')d\gamma' \quad (4.4)$$

$$\boldsymbol{\varepsilon}^{sc} = 0.23\int_0^{\gamma}\frac{\sigma}{E_c}d\gamma' \quad (4.5)$$

$$\boldsymbol{\varepsilon}^{dc} = F(\gamma,T) \quad (4.6)$$

$$\boldsymbol{\varepsilon}^{th} = \alpha(\gamma)(T - T_o) \quad (4.7)$$

$$E = H(\gamma,T) \quad (4.8)$$

$$E_c = I(\gamma,T) \quad (4.9)$$

where Equation 4.1 shows that the total strain consists of elastic strain ($\boldsymbol{\varepsilon}^{e}$), primary creep strain ($\boldsymbol{\varepsilon}^{pc}$), secondary creep strain ($\boldsymbol{\varepsilon}^{sc}$), dimensional change strain ($\boldsymbol{\varepsilon}^{dc}$) and thermal strain ($\boldsymbol{\varepsilon}^{th}$). In Equations 4.2 and 4.3 **D** is the stiffness matrix of the material defined by the Young's modulus **E** and Poisson's ratio, and $\check{\mathbf{D}}$ is the mean value of **D** in the current increment. These relations are used to define the Jacobian matrix ($\mathbf{C} = \partial\Delta\boldsymbol{\sigma}/\partial\Delta\boldsymbol{\varepsilon}$). The jacobian is used in the UMAT to calculate the increment in stresses $\Delta\sigma$ and update the

stresses in each increment of time. Equations 4.4 and 4.5 define the primary and secondary creep strain, respectively [2,4]. As shown in Equations 4.6 to 4.9, the dimensional change strain, thermal strain, dynamic Young's Modulus and creep Young's Modulus are functions of irradiation dose and temperature. By modifying these functions the UMAT can be applied to different materials.

4.2 VERIFICATION OF UMAT

To verify the UMAT, it was applied to the analysis of a cylindrical structure for which analytical results are available in the published literature [1]. To reduce the computation cost, only a section of the cylinder has been considered according to the symmetric condition, as shown in Figure 4.1.

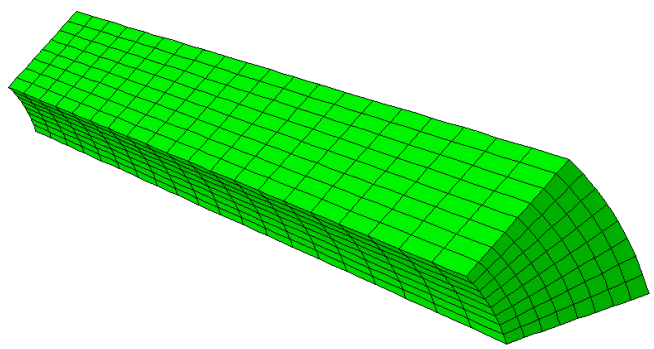

Figure 4.1: Meshed section of the cylinder

The cylinder section model contained 6345 nodes and 1280 C3D20 elements, which are 3D quadratic isoparametric elements with 20 nodes. Boundary conditions to enforce symmetry about the long axis were applied. The temperature was kept constant while the irradiation dose increased linearly with time. The inner surface of the cylinder was exposed to the highest level of irradiation and the irradiation decreased linearly with the increase in radial distance. Primary creep strain was neglected as it was very small relative to secondary creep strain. The irradiation period was 30 years. The irradiation dose distribution in the section after 30 years is shown in Figure 4.2.

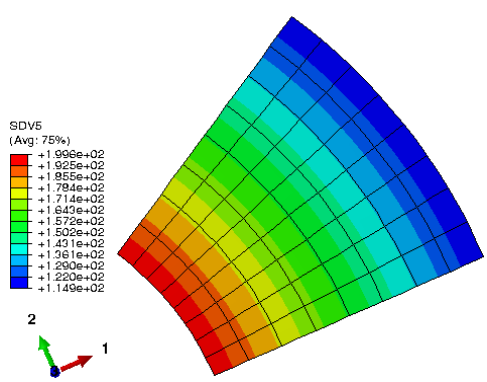

Figure 4.2: Variation of irradiation dose (10^{20} n/cm^2) in the cylindrical section with the radial distance

The model was analyzed using ABAQUS/standard and the results are shown in Figures 4.3 to 4.7. Figures 4.3 and 4.4 show the hoop and axial stress distributions, respectively, within the cylinder after 15 years.

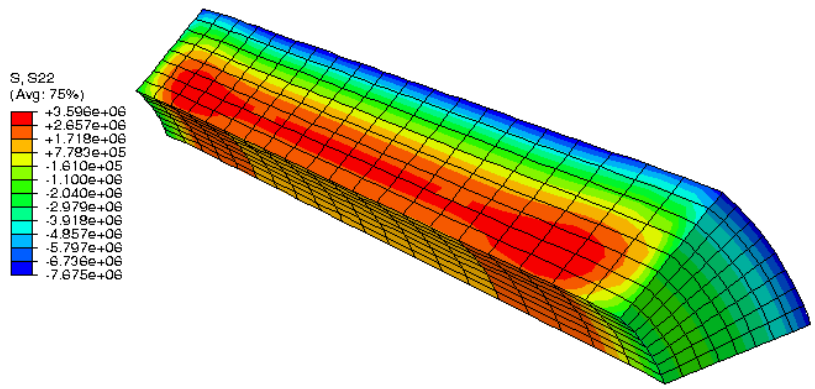

Figure 4.3: Hoop stress distribution after 15 years

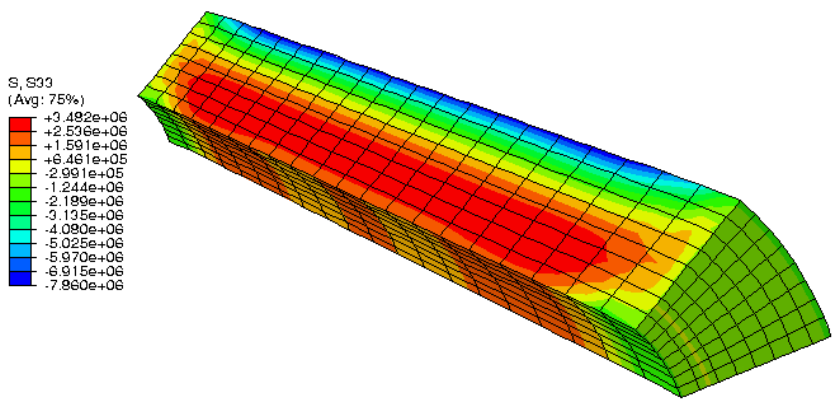

Figure 4.4: Axial stress distribution after 15 years

Figures 4.5 and 4.6 show the curves of hoop and axial stress against time, respectively, at the inner and outer surfaces of the cylinder.

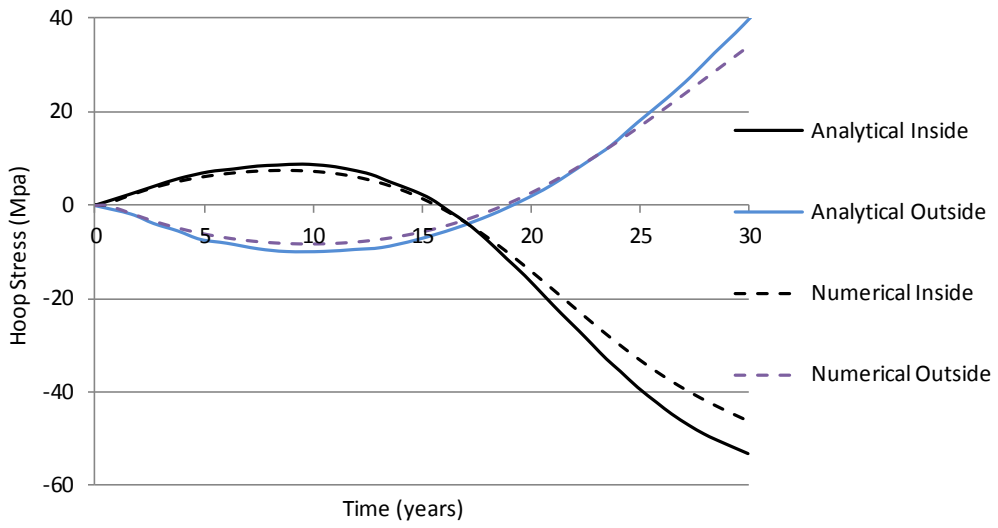

Figure 4.5: Hoop stresses against time at the inner and outer surfaces

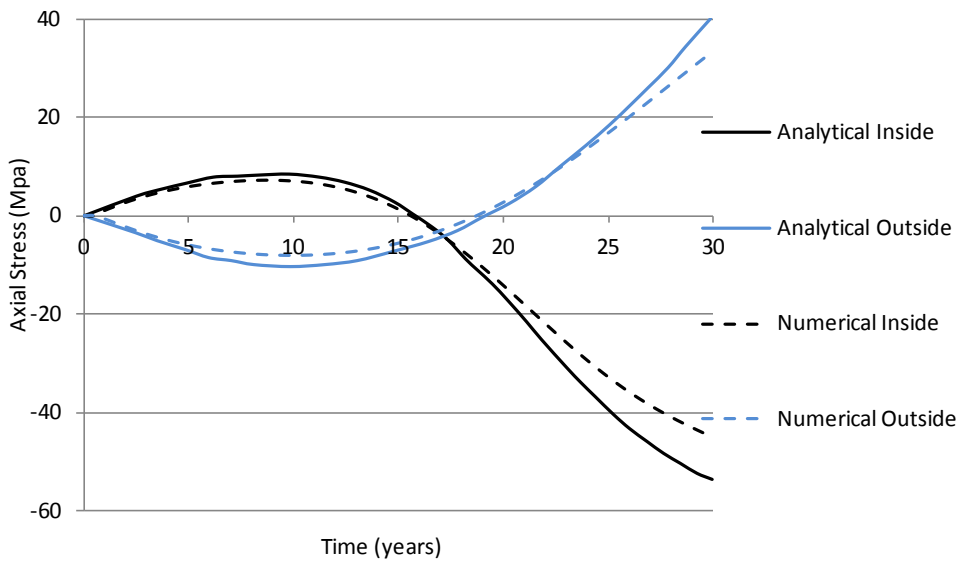

Figure 4.6: Axial stresses against time at the inner and outer surfaces

The results were compared with those published in the literature and were found to be in good agreement.

4.3 REFERENCES

1) H. Li, A. Fok and B. J. Marsden, An Analytical Study on the Irradiation – Induced Stresses in Nuclear Graphite Moderator Bricks, , Journal of Nuclear Materials, 372, 164 – 170, (2008)
2) Suyuan Yu, H. Li, C. Wang and Z. Zhang, Probability assessment of graphite brick in the HTR – 10, Nuclear Engineering and Design, 227, 133 – 142, (2004)
3) D.K.L. Tsang and B.J. Marsden, The Development of a Stress Analysis Code for Nuclear Graphite Components in Gas – Cooled Reactors, Journal of Nuclear Materials, 350(3), 208 – 220, (2006)

5. Modeling Residual Stresses in VHTR Graphite Components

The developed UMAT was employed to carry out the stress analysis in a HTR brick. Considering the symmetry of the HTR graphite brick, only a quarter of the brick was analyzed to minimize the computational cost (see Figure 5.1). The HTR brick model was meshed with the C3D20R element, which is a 3D quadratic isoparametric element with 20 nodes that employs reduced integration. The model contained 17398 nodes and 3640 elements. Boundary conditions to enforce symmetry about the horizontal and vertical mid-planes were applied. Also, one of the corner nodes near the center of the core was constrained in all directions to avoid rigid body motion.

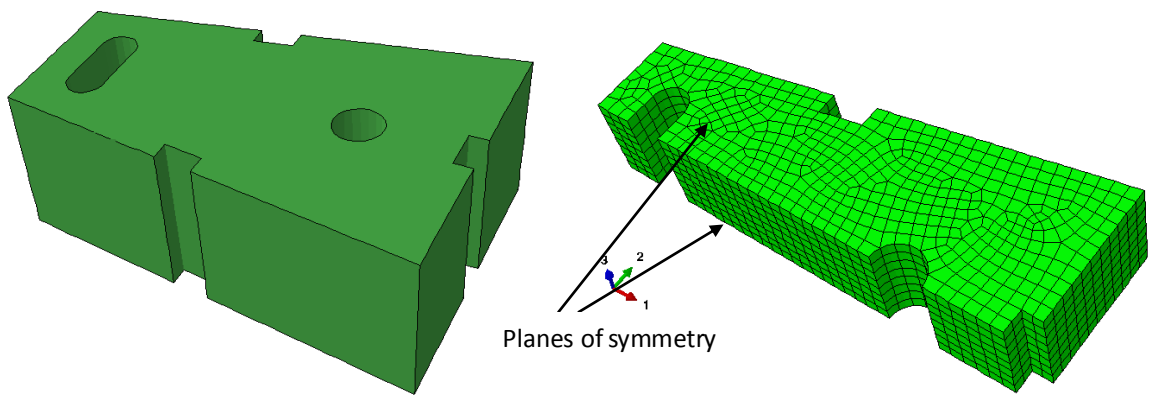

Figure 5.1: A full model (left) and a meshed quarter model (right) of HTR graphite brick

5.1 Load and boundary conditions

The brick was subjected to load and boundary conditions which represented those in the HTR. Due to the unavailability of data in the literature, some assumptions were made, as explained later. The equations for the model are given below:

$$\gamma = (p_1 + p_2 x)t \tag{5.1}$$

$$T = (q_1 + q_2 x) \tag{5.2}$$

$$\alpha = a_1\gamma^2 + a_2\gamma + a_3 \tag{5.3}$$

$$\boldsymbol{\varepsilon}^{dc} = (b_1\gamma^5 + b_2\gamma^4 + b_3\gamma^3 + b_4\gamma^2 + b_5\gamma + b_6)\, f_\varepsilon \tag{5.4}$$

$$\text{where } f_\varepsilon = c_4T^2 + c_5T + c_6 \tag{5.5}$$

$$Y = (d_1\gamma^5 + d_2\gamma^4 + d_3\gamma^3 + d_4\gamma^2 + d_5\gamma + d_6)\, f_Y \tag{5.6}$$

where $f_Y = (e_1T^5 + e_2T^4 + e_3T^3 + e_4T^2 + e_5T + e_6)$ (5.7)

$$\boldsymbol{\varepsilon}^c = 0.23\int_0^{\gamma} \frac{\sigma}{E_c} d\gamma' \quad (5.8)$$

$$E_c = (f_1\gamma^5 + f_2\gamma^4 + f_3\gamma^3 + f_4\gamma^2 + f_5\gamma + f_6) \quad (5.9)$$

$$\boldsymbol{\varepsilon}^{th} = \alpha\Delta T \quad (5.10)$$

The neutron dose (γ) at any point in the brick was assumed to be a function of time (t) and the distance from the center of the core, as shown in Equation 3.1, where x represents the radial distance from the core center, and t represents time and p and q are constants. Dose was assumed to decrease linearly with distance and increase linearly with time. It was assumed that the reactor would operate for 30 years.

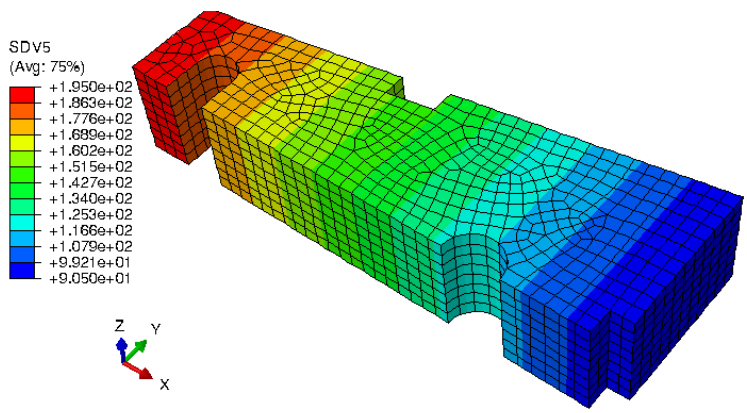

Figure 5.2: Assumed distribution of irradiation dose (10^{20} n/cm^2) in the HTR graphite brick at 17th year

A temperature (T) gradient was also assumed to be present in the HTR graphite brick, as given by Equation 3.2. The temperature was highest at the face closest to the core center and decreased linearly with distance from it. The dependence of the coefficient of thermal expansion (α) on the dose and temperature was considered. The relation was obtained by fitting a quadratic curve to experimental data available in [4]. Similarly, the dependence of the dimensional change strain ($\boldsymbol{\varepsilon}^{dc}$) on dose at 600°C was obtained by fitting a polynomial curve of 5th degree through the data presented in [5]. The dimensional change strains at temperatures 380°C and 1200°C were obtained from [6] and [7]. However, since the data at other temperatures was available for low dose only, the temperature dependence of the dimensional change strain had to be extrapolated for the time being.

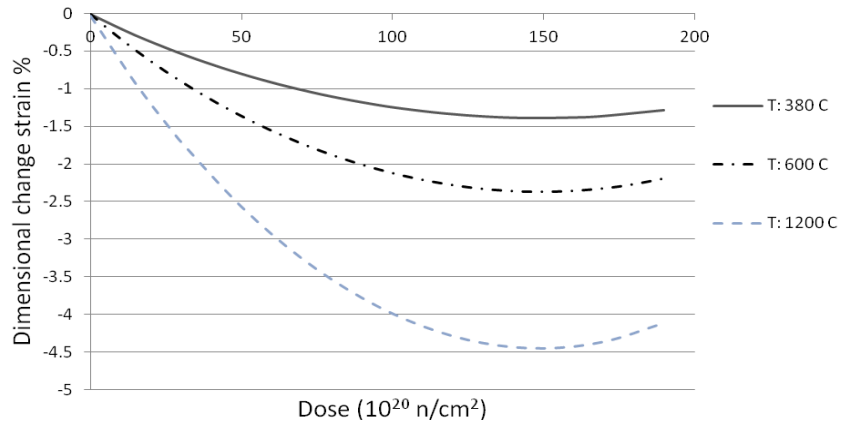

Figure 5.3: Assumed variation of dimensional change strain with neutron dose at different temperatures

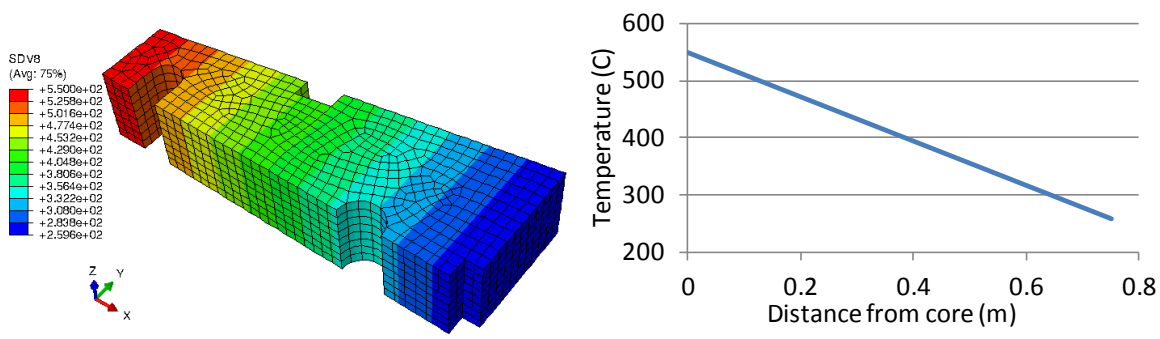

Figure 5.4: Assumed variation of temperature (°C) in the HTR graphite brick with distance from the core

Young's modulus's (Y) variation with dose was based on the data presented in [5], while the temperature dependence of Young's modulus (f_Y) was taken from [8]. 5th order polynomial curves were used to fit both sets of data. The combined dependence is shown in Equations 5.6 and 5.7. Creep strain's ($\boldsymbol{\varepsilon}^c$) variation with dose was also considered in the analysis. However, due to insufficient data for either IG 110 or IG 11, the creep strain data of graphite used in the Advanced Gas-cooled Reactor (AGR) were used. The dependence of creep strain and creep Young's modulus (E_c) on dose is shown in Equations 5.8 and 5.9, respectively. The relation of thermal strain to temperature is shown in Equation 5.10. The value of the constants involved in equations 5.1-5.10 are given in Appendix.

5.2 Simulation results

The brick model was analyzed using ABAQUS/standard and the results are shown in Figures 5.5 to 3.13. Figures 5.5, 5.6, 5.7 and 5.8 show the radial, hoop, axial and maximum principal stress distributions, respectively, within the HTR brick after 30 years of irradiation.

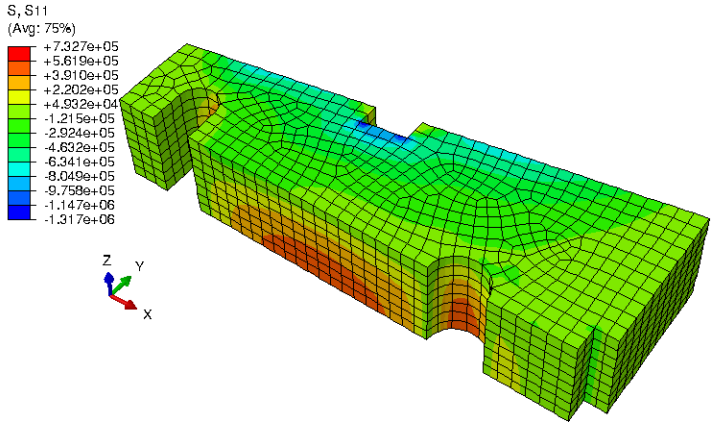

Figure 5.5: Radial stress distribution after 30 years

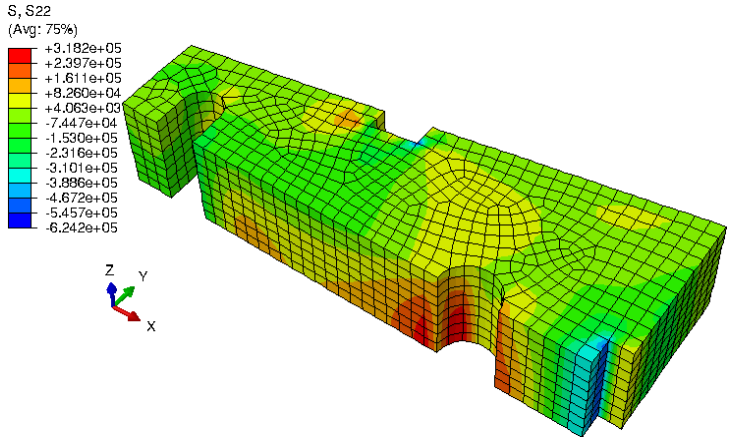

Figure 5.6: Hoop stress distribution after 30 years

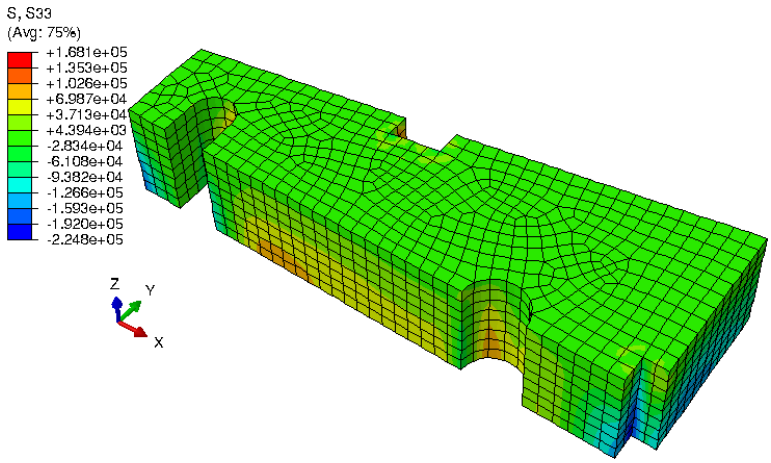

Figure 5.7: Axial stress distribution after 30 years

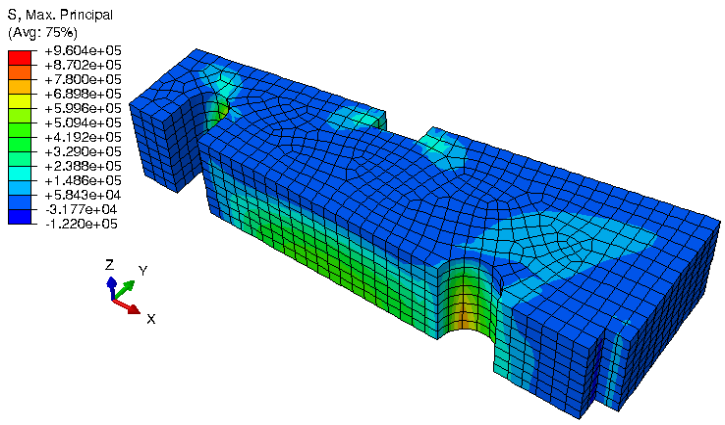

Figure 5.8: Maximum Principal stress distribution after 30 years

It was found that the radial stresses ranged from 0.73 MPa in tension to 0.13 MPa in compression. The hoop stresses ranged from 0.32 MPa in tension to 0.62 MPa in compression and the axial stresses ranged from 0.17 MPa in tension to 0.22 MPa in compression. The maximum principal stress ranged from 0.96 MPa in tension to 0.12 MPa in compression. The stresses were found to be high in the regions of sharp edges and corners, which indicated stress concentration. The variations of the radial, hoop and axial stresses with time at two different locations (node A and node B in Figure 5.9) on the brick are shown in Figures 5.10 to 5.13. For node A, the radial and hoop stresses were found to be compressive throughout the operation of the reactor, while the axial stresses turned from compressive to tensile at about 15 years. For node B, on the other hand, the radial, hoop and axial stresses were tensile throughout the operation of the reactor.

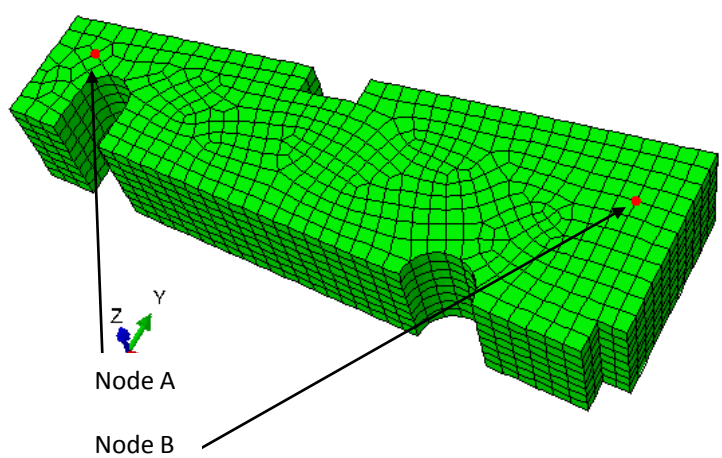

Figure 5.9: Location of two points of interest (node A and node B)

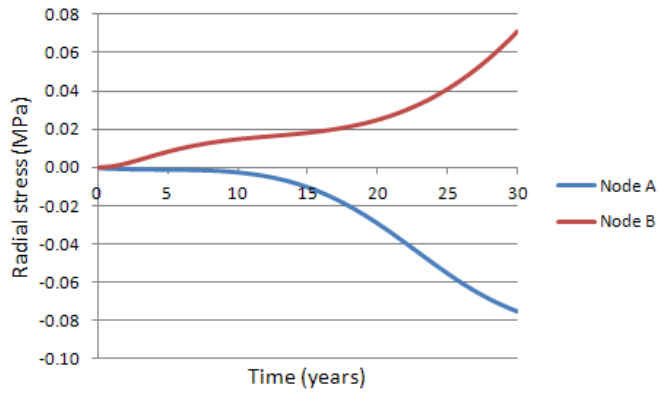

Figure 5.10: Variation of radial stress (S11) with time at two locations

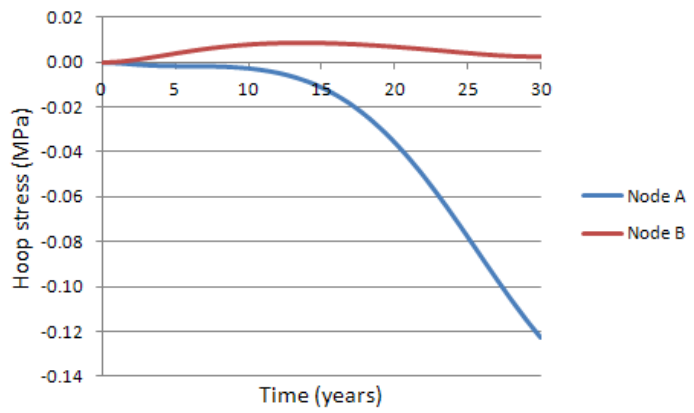

Figure 5.11: Variation of hoop stress (S22) with time at two locations

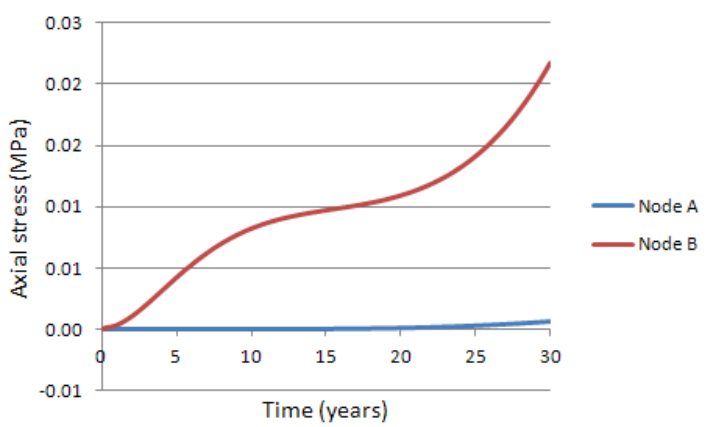

Figure 5.12: Variation of axial stress (S33) with time at two locations

5.3 REFERENCES

1) H. Li, A. Fok and B. J. Marsden, An Analytical Study on the Irradiation – Induced Stresses in Nuclear Graphite Moderator Bricks, , Journal of Nuclear Materials, 372, 164 – 170, (2008)
2) Suyuan Yu, H. Li, C. Wang and Z. Zhang, Probability assessment of graphite brick in the HTR – 10, Nuclear Engineering and Design, 227, 133 – 142, (2004)
3) D.K.L. Tsang and B.J. Marsden, The Development of a Stress Analysis Code for Nuclear Graphite Components in Gas – Cooled Reactors, Journal of Nuclear Materials, 350(3), 208 – 220, (2006)
4) H. Wang, X. Zhou, L. Sun, J. Dong and S. Yu, The effect of stress levels on the coefficient of thermal expansion of a fine – grained isotropic nuclear graphite, Nuclear Engineering and Design, 239, 484 – 489, (2009)
5) S. Ishiyama, T.D. Burchell, J.P. Striazak and M. Eto, The effect of high fluence neutron irradiation on the properties of a fine – grained isotropic nuclear graphite, Journal of Nuclear Materials, 230, 1 -7, (1996)
6) H. Matsuo, Effect of high temperature neutron irradiation on dimensional change and physical properties of nuclear graphite for HTGR. JAERI-M87-207.
7) I.G. Lebedev, O.G. Kochkarev and Y.S.Virgil'ev, Radiation – Induced change in the properties of isotropic structural graphite, Atomic energy, 93(1), 589 – 594, (2002)
8) T. Konishi, M. Eto and T. Oku, High temperature Young's Modulus of IG – 110 Graphite, JAERI-M86-192.
9) Gyanender Singh, Haiyan Li and Alex Fok, Modeling the residual stresses in VHTR graphite component using user defined subroutine UMAT, NEUP Quarterly report

5.4 APPENDIX

p1	270
p2	385
q1	550
q2	387
a1	-4.00E-5
a2	0.0106
a3	3.35

b1	-2.374E-12
b2	1.88E-9
b3	-5.314E-7
b4	1.704E-4
b5	-3.444E-2
b6	-1.771E-2
c4	-5.081E-7
c5	2.378E-3

c6	-0.2439
d1	1.122E-12
d2	-7.999E-10
d3	-5.522E-7
d4	2.487E-4
d5	2.562E-2
d6	7.498
e1	2.99E-16

e2	-9.169E-13
e3	9.228E-10
e4	-1.938E-7
e5	2.265E-6
e6	0.9998
f1	6.114E-7
f2	-2.999E-4
f3	4.504E-2
f4	-1.7506
f5	1.817E1
f6	9.1029E3

6. EXTENDED FINITE ELEMENT METHOD (XFEM) FOR MODELING FAILURE IN GRAPHITE

The user element subroutine (UEL) was replaced by Extended Finite Element Method (XFEM) for modeling failure in graphite and ceramics. XFEM is a relatively new technique which can be used to solve differential equations with discontinuous functions. It has been implemented in Abaqus and other commercial finite element software to model discontinuities including cracks. It was developed by Belytschko et al. [1] in 1999 and is based on the unity partition function [2]. It has significant advantages over the conventional finite element method for modeling cracks in terms of obviating the needs of a very fine mesh to capture singular asymptotic fields and remeshing during crack propagation, thus making the process of crack modeling less cumbersome and cheaper.

6.1 MODELING CRACK PROPAGATION USING XFEM

The XFEM is an extension of the conventional finite element method and can be employed to model cracking in structures. It allows the presence of discontinuities in an element by enriching it with special degrees of freedom which obviate the need to match the mesh with the geometry of the discontinuity [3]. Thus, XFEM can be used to simulate crack initiation and propagation along an arbitrary, solution-dependent path. The XFEM technique has been explored in the current task for its possible use in the prediction of fracture in graphite bricks under in-reactor conditions.

In Abaqus' implementation of XFEM [3], the approximation for a displacement vector function u is given as:

$$\mathbf{u} = \sum_{i=1}^{N} N_I(x)\,[\mathbf{u}_I + H(x)\mathbf{a}_I + \sum_{\alpha=1}^{4} F_\alpha(x)\,\mathbf{b}_I^\alpha] \tag{6.1}$$

where

$N_I(x)$: nodal shape function
a_I: nodal enriched degree of freedom vector
$H(x)$: discontinuous jump function across the crack surfaces
$F_\alpha(x)$: Elastic asymptotic crack tip functions
b_I: nodal enriched degree of freedom vector

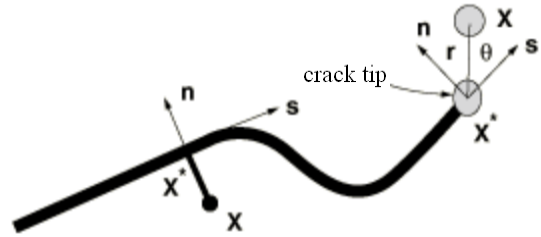

Figure 6.1: Normal and tangential coordinates for a smooth crack

$$H(x) = \begin{cases} 1 & \text{if } (x - x^*).n \geq 0 \\ -1 & \text{otherwise} \end{cases} \tag{6.2}$$

where x is the sample (Gauss) point, x^* is the point on the crack closest to x and n is the unit outward normal to the crack at x^*. Figure 6.1 shows the normal and tangential coordinate systems used in Abaqus for a crack.

$$F_\alpha(x) = [\sqrt{r}\sin\frac{\theta}{2}, \sqrt{r}\cos\frac{\theta}{2}, \sqrt{r}\sin\theta\sin\frac{\theta}{2}, \sqrt{r}\sin\theta\cos\frac{\theta}{2}] \tag{6.3}$$

where (r,θ) is the polar coordinate system having its origin at the crack tip.

In Abaqus, XFEM can be used to model cracking in two ways: 1) using the cohesive segment method and phantom nodes and 2) using the principles of linear elastic fracture mechanics and phantom nodes. The cohesive segment method was used for the current task. This method can be used to model cracking in both ductile and brittle materials.

The available traction-separation model in Abaqus assumes initially linear elastic behavior followed by damage initiation and evolution. The normal, shear and tangential separations are linearly related to the corresponding traction stresses as:

$$\begin{Bmatrix} t_n \\ t_s \\ t_t \end{Bmatrix} = \begin{bmatrix} K_{nn} & 0 & 0 \\ 0 & K_{ss} & 0 \\ 0 & 0 & K_{tt} \end{bmatrix} \begin{Bmatrix} \delta_n \\ \delta_s \\ \delta_t \end{Bmatrix} \tag{6.4}$$

where t_n, t_s and t_t are normal, shear and tangential tractions, δ_n, δ_s and δ_t are the corresponding displacements and K_{nn}, K_{ss} and K_{tt} are the stiffness matrix components based on elastic properties. However, once the damage initiation criterion is met the traction separation response of the element can be either linear or non-linear. A non-linear traction-separation response curve is shown in Figure 6.2.

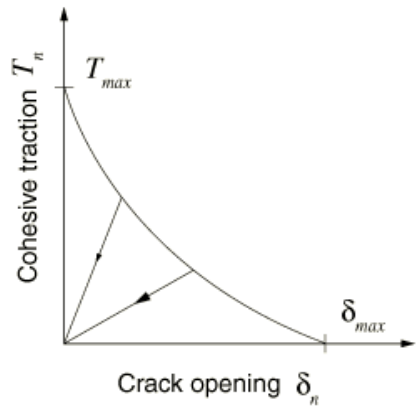

Figure 6.2: A non-linear traction-separation response [3]

Crack is said to be initiated when the cohesive response of the enriched element degrades. There are several criteria for crack initiation defined in Abaqus:

a) the maximum principal stress criterion
b) the maximum principal strain criterion
c) the maximum nominal stress criterion
d) the maximum nominal strain criterion
e) the quadratic traction interaction criterion
f) the quadratic separation interaction criterion

For the current task, the maximum principal stress criterion was used. It is given as:

$$f = \frac{\langle \sigma_{max} \rangle}{\sigma^{o}_{max}} \tag{6.5}$$

where

$$\langle \sigma_{max} \rangle = \sigma_{max} \text{ if } \sigma_{max} > 0 \qquad \langle \sigma_{max} \rangle = 0 \quad \text{ if } \sigma_{max} \leq 0 \tag{6.6}$$

The crack initiates or extends when f reaches the value 1.0 within the given tolerance: $1 \leq f \leq f_{tol}$. Similarly, other criteria can be specified.

Damage evolution specifies the rate of degradation of the cohesive stiffness after damage initiation. In Abaqus, it is implemented through a scalar variable D which represents the averaged overall damage at the intersection between the crack surfaces and the edges of the cracked elements. With no damage, its value is 0 and as damage occurs, its value increases up to 1. The normal and shear stresses are dependent on D as:

$$t_n = \begin{cases} (1 - D)T_n, \ T_n \geq 0 \\ T_n \text{ (no damage to compressive stifness)} \end{cases} \tag{6.7}$$
$$t_s = (1 - D)T_s$$
$$t_t = (1 - D)T_t$$

where T_n, T_s and T_t are the traction stresses for the current separations without damage. Figure 6.3 shows the crack passing through the elements in XFEM simulation. The ability of the crack to pass through elements makes crack propagation solution dependent and the crack path is not required to be known beforehand.

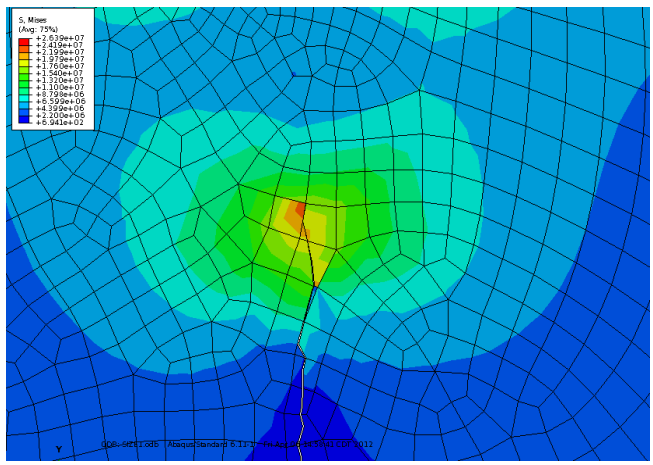

Figure 6.3: Crack propagation through the enriched elements during the three-point bend test

6.2 ASSESSING THE VIABILITY OF XFEM

The possibility of using the Extended Finite Element Method (XFEM) for modeling fracture in graphite components was explored by:

1) Studying the effect of mesh type and mesh size on crack propagation behavior;
2) Simulating 3D crack propagation in graphite structures.

Using the commercial finite element software Abaqus, the XFEM technique was employed to simulate crack propagation in graphite specimens under three-point bending for two dimensional and three dimensional cases. The effect of the mesh (type and size) on the crack propagation behavior was studied using two dimensional models.

To understand the sensitivity of the simulation to mesh type, the middle region of the beam through which the crack is expected to propagate was meshed in two ways using: a) a structured mesh and b) an unstructured mesh, as shown in Figure 6.4.

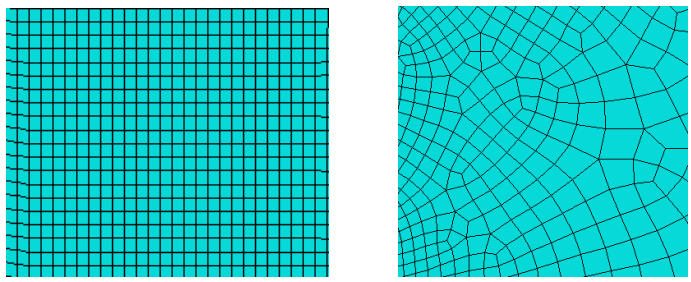

(a) (b)

Figure 6.4: FE meshes: (a) structured and (b) unstructured

To understand the effect of mesh size, the graphite beam model was meshed with three different sized elements. The simulation results for the three cases of mesh size were compared.

Since structured meshing was found to give more consistent results, it was used in the crack region for simulating 3D crack propagation in graphite specimens under three-point bending.

All the computational results were compared with the experimental results and the percentage errors evaluated.

6.2.1 Mesh Sensitivity of XFEM Crack

Figure 6.5 shows a graphite beam model under three-point bending. An initial crack was built in the beam model using the assembly feature. The initial crack length to beam width ratio was $a_o/W \approx 0.4$. The dimensions of the graphite beams and initial crack lengths are given in Table 6.1.

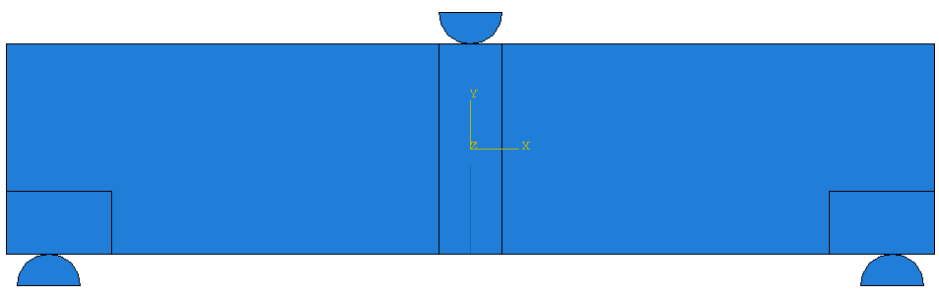

Figure 6.5: A three-point-bend beam model showing the initial crack, supports and loading bar

Table 6.1: Dimensions for the three different sizes of graphite beams and their initial crack lengths

Size	Total length (L/mm)	Span (S/mm)	Width (W/mm)	Thickness (B/mm)	Initial crack length (a_o/mm)
Size 1	220	200	50	25	21
Size 2	110	100	20	10	8
Size 3	45	40	10	5	4

Young's modulus (E) and Poisson's ratio (υ) of the graphite were assumed to be 12 GPa and 0.2, respectively. The maximum principal stress criterion was selected as the damage initiation criterion with the critical maximum principal stress taken to be 21 MPa. The incorporated damage evolution law was based on fracture energy and the softening was assumed to be linear. The critical fracture energy was set as 188 J/m^2. The critical fracture energy was calculated using the critical stress intensity factor (K_{IC}), which was experimentally found to be around 1.4 MPa$\sqrt{m}$ [5], and the Irwin relationship for plane strain case: $G = (1-\upsilon^2)\frac{K^2}{E}$.

6.2.2 Effect of Mesh Type on XFEM Crack

To understand the effect of mesh type on the crack propagation behavior modeled by XFEM, two kinds of mesh were considered: a) Unstructured mesh and b) Structured mesh (Figure 6.4). Figures 6.6 and 6.7 show the two graphite specimens under three-point bending with unstructured and structured mesh, respectively. The element type was CPS4R quad-shaped, plane-strain, reduced-integration element. The edges of the beam in contact with the supporting and loading bars were more densely meshed so as to provide proper interaction of the surfaces. Beams with three different sizes, as shown in Table 6.1, were all modeled using structured and unstructured mesh, respectively. Table 6.2 shows the total number of elements in each model. The number of elements for the structured and unstructured meshes was kept roughly the same for each size.

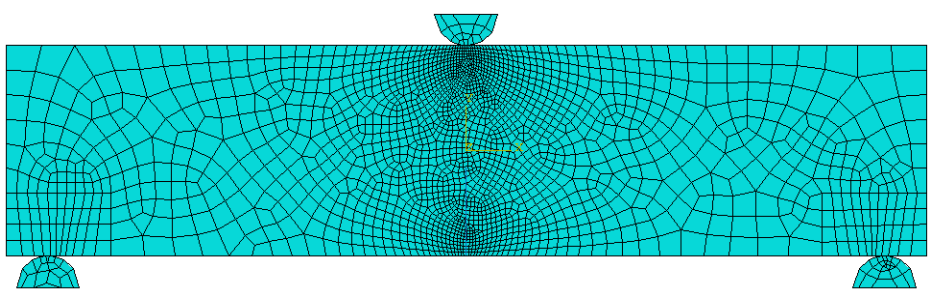

Figure 6.6: A three-point-bending graphite model with unstructured mesh in the middle region

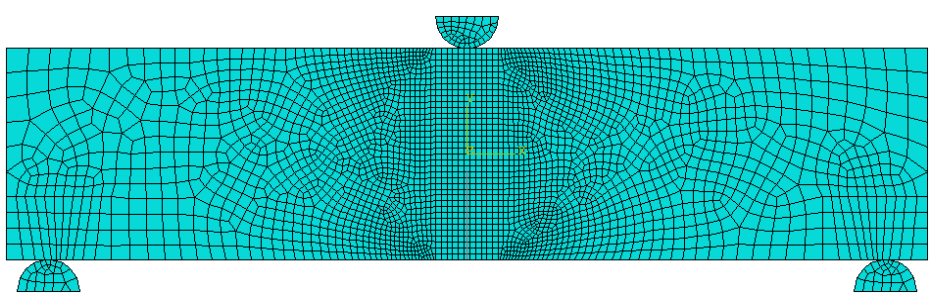

Figure 6.7: A three-point-bending graphite model with structured mesh in the middle region

Table 6.2: Total number of elements in the graphite beams

	Unstructured mesh	Structured mesh
Size 1	2932	2910
Size 2	2401	2514
Size 3	2925	2719

The two support half-rollers were fixed and a vertical displacement was applied from the top loading roller. The three-point bending model was solved using Abaqus Standard.exe. The numerical simulation was stabilized using damping effect. Figures 6.8, 6.9 and 6.10 show the crack path for unstructured and structured meshes for beam sizes 1, 2 and 3 respectively.

6.2.3 Results

6.2.3.1 Effect of mesh type

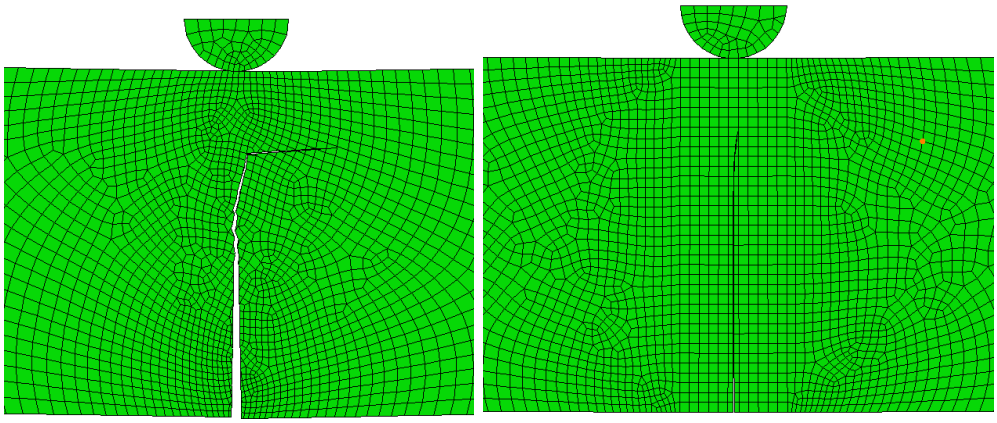

Figure 6.8: Simulated crack paths for size 1 graphite beam with unstructured (left) and structured (right) meshes

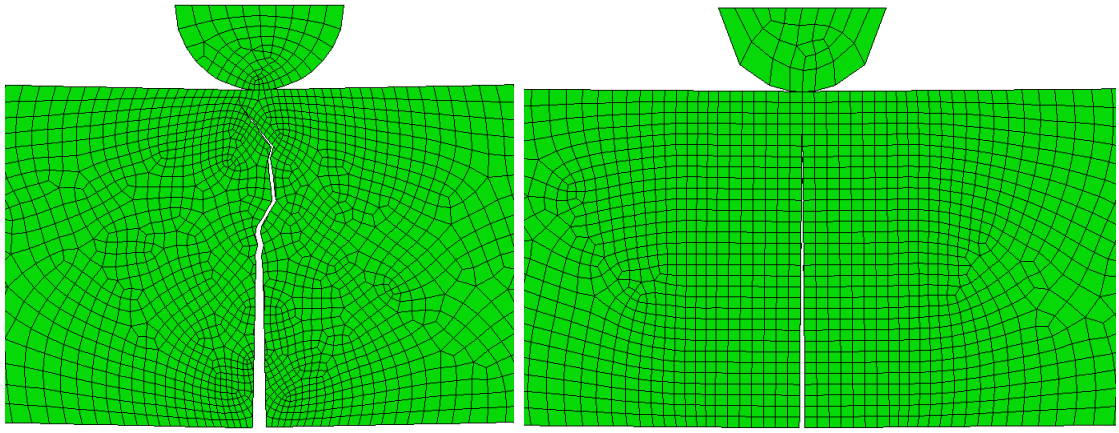

Figure 6.9: Simulated crack paths for size 2 graphite beam with unstructured (left) and structured (right) meshes

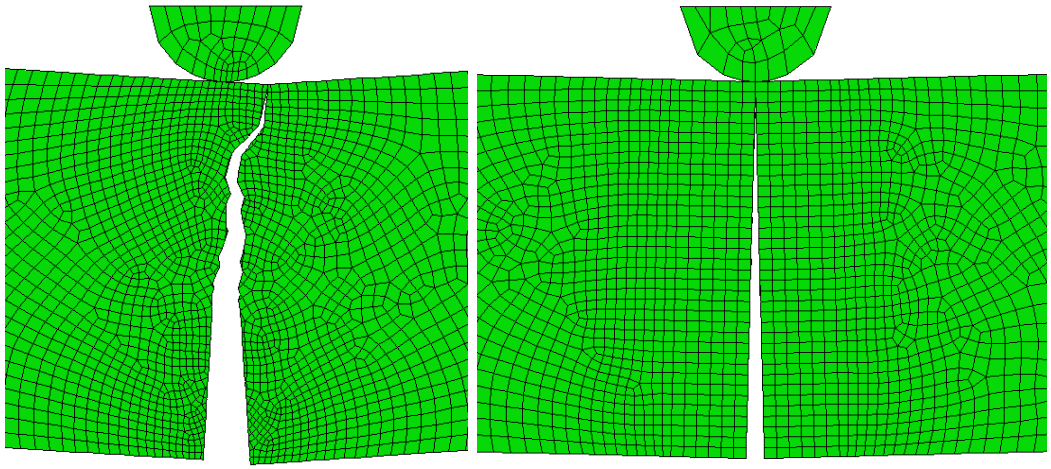

Figure 6.10: Simulated crack paths for size 3 graphite beam with unstructured (left) and structured (right) meshes

Figures 6.8, 6.9 and 6.10 show that the crack propagates in a straight line in size-2 and 3 beams with a structured mesh. While with an unstructured mesh the crack did not propagate in a straight path, especially when it approached the loading roller. For the size-1 beam, the crack turned its direction by about 70° with an unstructured mesh, while with a unstructured mesh there was slight change in the direction of crack.

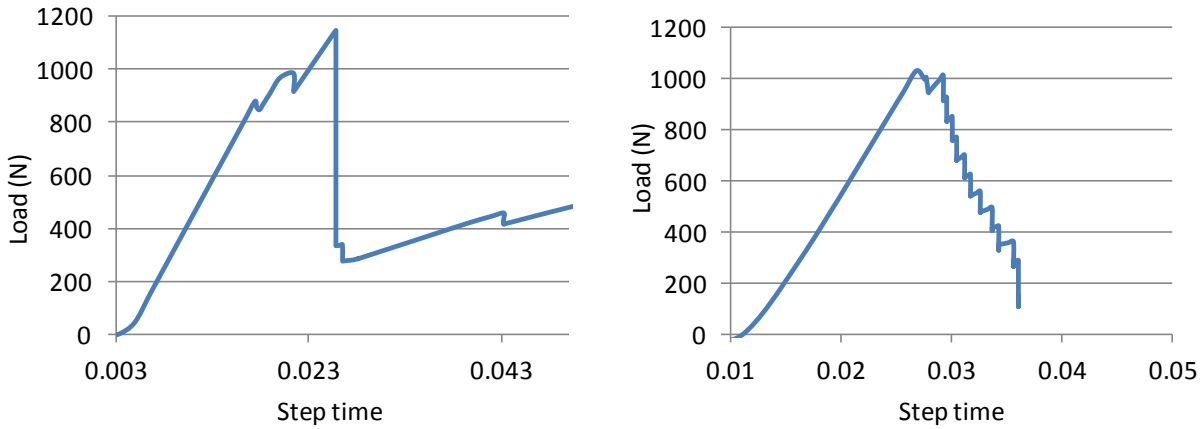

Figure 6.11: Simulated load vs. step time curves for size 1 graphite beam with unstructured (left) and structured (right) meshes

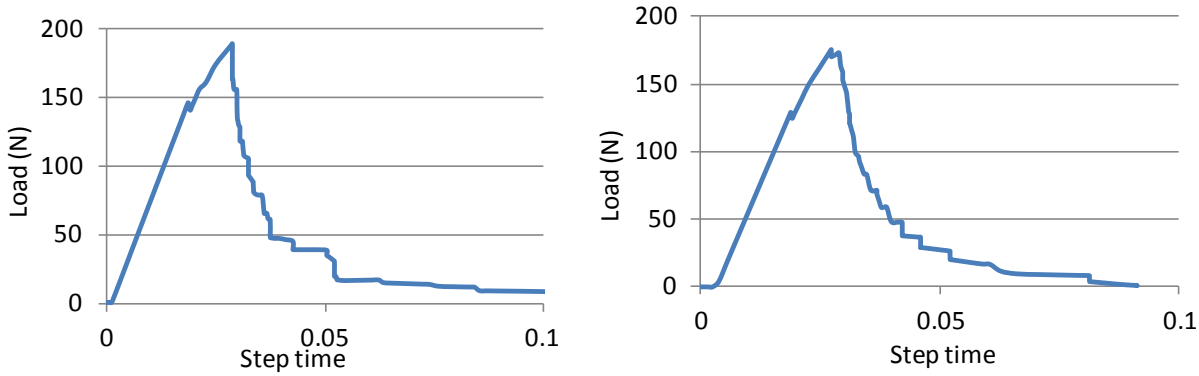

Figure 6.12: Simulated load vs. step time curves for size 2 graphite beam with unstructured (left) and structured (right) meshes

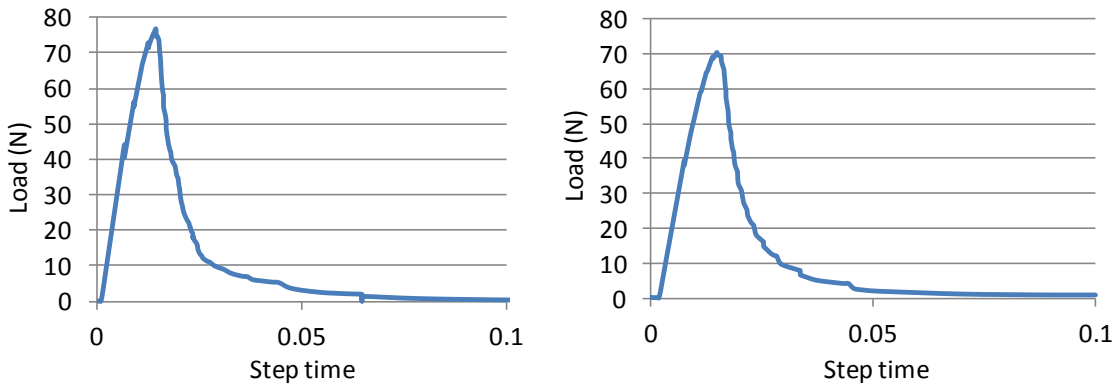

Figure 6.13: Simulated load vs. step time curves for size 3 graphite beam with unstructured (left) and structured (right) meshes

Figures 6.11, 6.12 and 6.13 show the load vs. step time curves for the structured and unstructured meshes for all the three different sized graphite beams. It can be seen that the pre and post-peak behavior of crack propagation is smoother for structured meshes. For the size-1 graphite beam with an unstructured mesh, there is an increase in the load within the post-peak region. This is attributed to the sharp change in crack path towards the horizontal direction (Figure 6.8). For all other cases the post-peak behavior appears quite reasonable. The predicted peak loads and the corresponding errors, when compared with the experimental peak loads, for both types of mesh are shown in Table 6.3.

Table 6.3: Experimental and computational peak loads and the corresponding errors

	Experimental peak load (N)	Computational peak load (N)		peak load error (%)	
		Unstructured mesh	Structured mesh	Unstructured mesh	Structured mesh
Size 1	1093	1148	1029	-5.0 %	5.9 %
Size 2	187	189	175	-1.1 %	6.4 %
Size 3	81	77	70	4.9%	13.6%

Table 6.3 shows that for graphite beams with sizes 1 and 2, the peak load was over-predicted for unstructured mesh and under-predicted for structured mesh. For graphite beam with size 3, peak load was under predicted for both types of meshes. The absolute % error was found to be smaller for the unstructured mesh.

6.2.3.2 Effect of mesh size

To understand the effect of mesh size on the behavior of crack propagation simulated with XFEM, three mesh sizes were considered. Table 6.4 shows the number of elements and element size in the middle region of the graphite beam for each size of graphite beam. In mesh2, the element size was about twice of the size in mesh1, and in mesh3 the element size was about four times the size in mesh1. Thus, mesh1 was finer than mesh2 and mesh2 was finer than mesh3. Figures 6.14, 6.15 and 6.16 show the simulated crack paths for the three different meshes for beam sizes 1, 2 and 3 respectively.

Table 6.4: Number of elements for structured and unstructured meshes for 3 different sizes

	Number of elements in the graphite beam			**Approximate element size in the mid-region of the beam(mm)**		
	Mesh1	**Mesh2**	**Mesh3**	**Mesh1**	**Mesh2**	**Mesh3**
Size 1	6405	2910	970	0.71	1.42	2.78
Size 2	5843	2514	784	0.33	0.67	1.33
Size 3	6736	2719	991	0.14	0.29	0.56

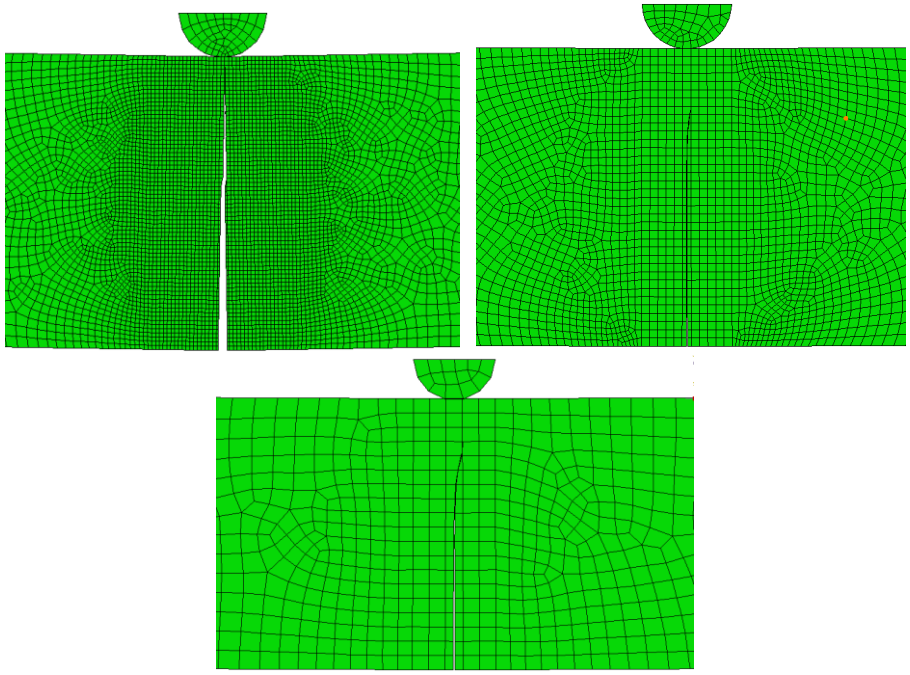

Figure 6.14: Simulated crack paths for size 1 graphite beam with mesh1 (upper left), mesh2 (upper right) and mesh3 (lower)

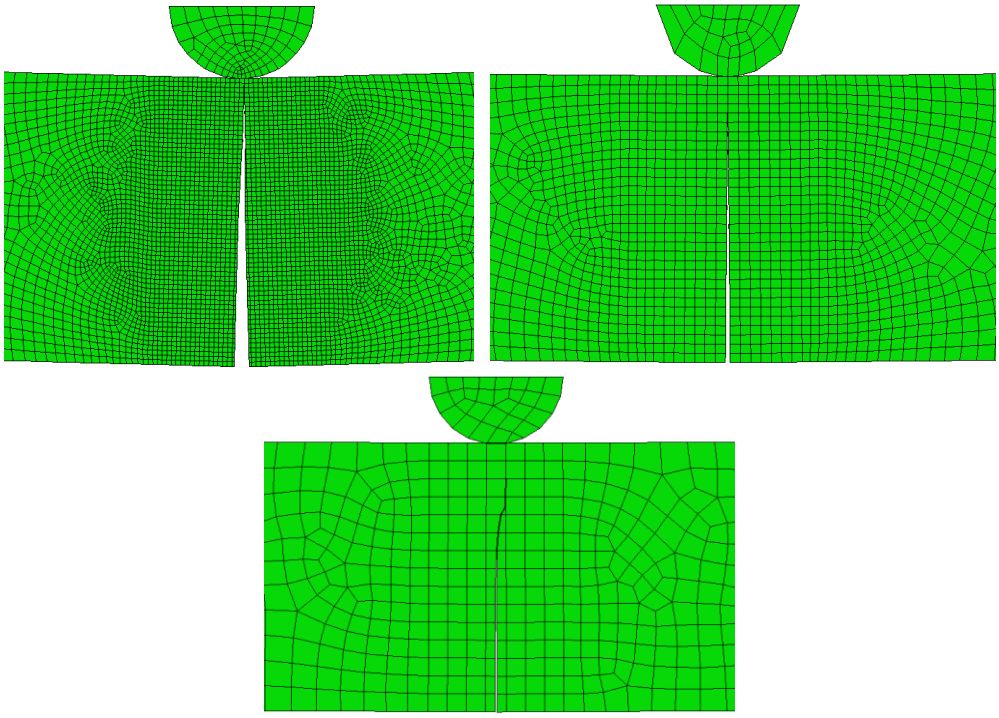

Figure 6.15: Simulated crack paths for size 2 graphite beam with mesh1 (upper left), mesh2 (upper right) and mesh3 (lower)

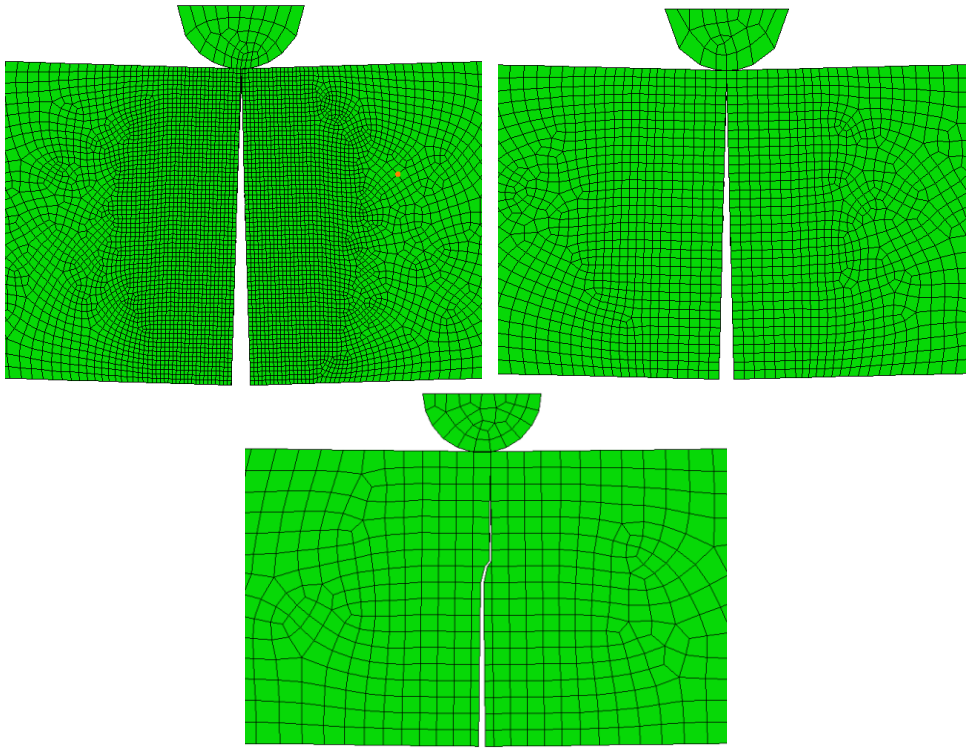

Figure 6.16: Simulated crack paths for size 3 graphite beam with mesh1 (upper left), mesh2 (upper right) and mesh3 (lower)

It can be seen from Figures 6.14, 6.15 and 6.16 that the crack propagation directions were slightly changed in models with coarse meshes (mesh3). While with finer meshes (mesh1 and mesh2) the cracks propagated in an almost straight line.

Figures 6.17, 6.18 and 6.19 show the load vs. step time for the three types of mesh for beam sizes 1, 2 and 3, respectively. It can be seen from the figures that the load vs. step time curves were smoothest for the finest mesh (mesh1) and the curves became rough as the mesh size increased. For mesh3, which was the coarsest mesh, the load-step time was found to be least smooth.

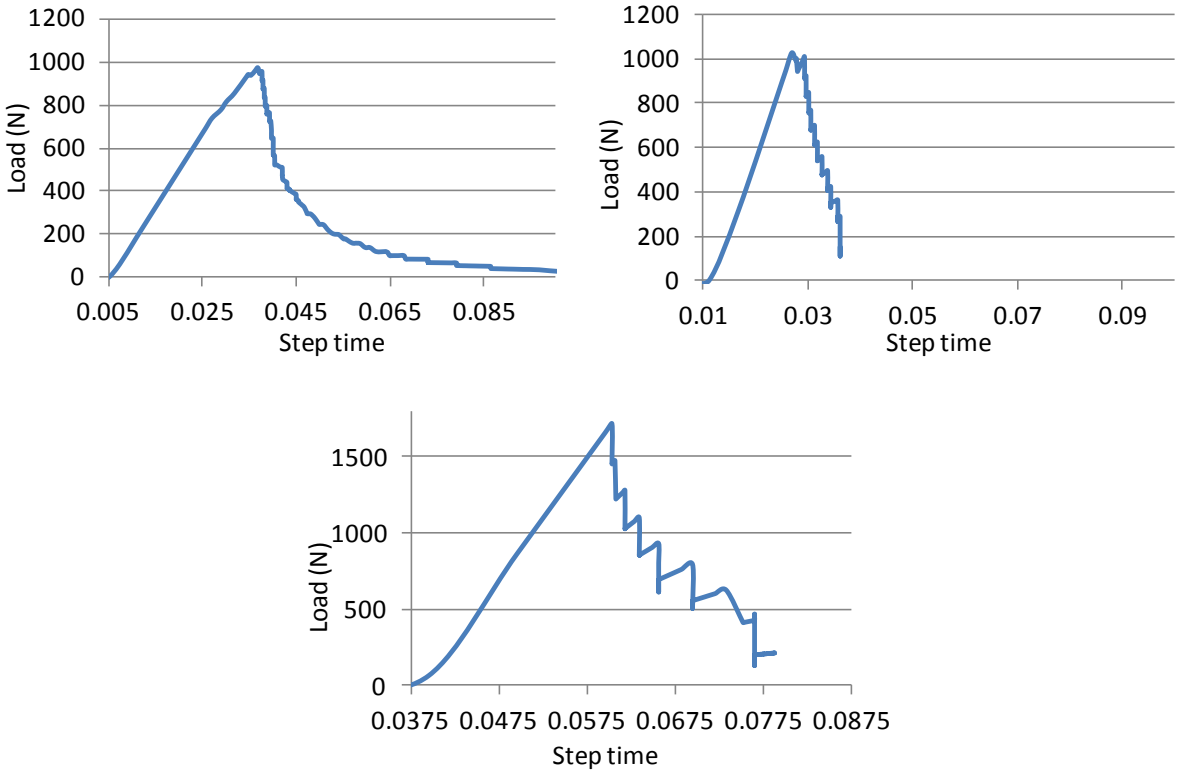

Figure 6.17: Simulated load vs. step time curves for size 1 graphite beam with mesh 1 (upper left), mesh 2 (upper right) and mesh 3 (lower).

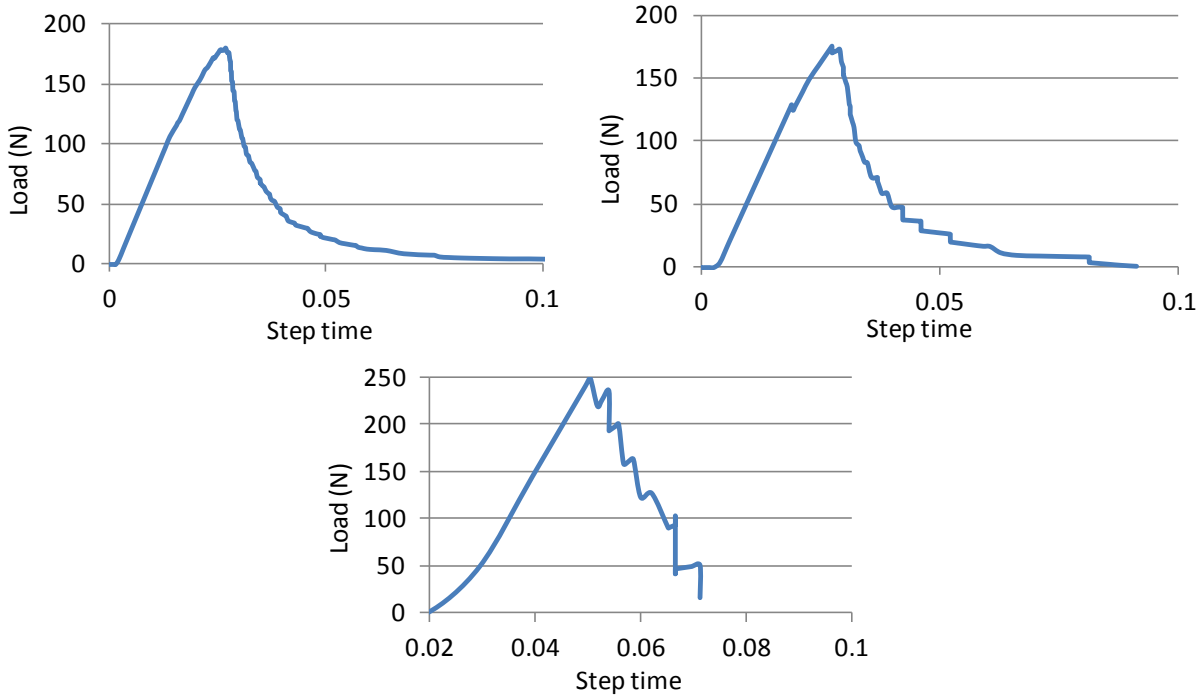

Figure 6.18: Simulated load vs. step time curves for size 2 graphite beam with mesh 1(upper left), mesh 2 (upper right) and mesh 3 (lower)

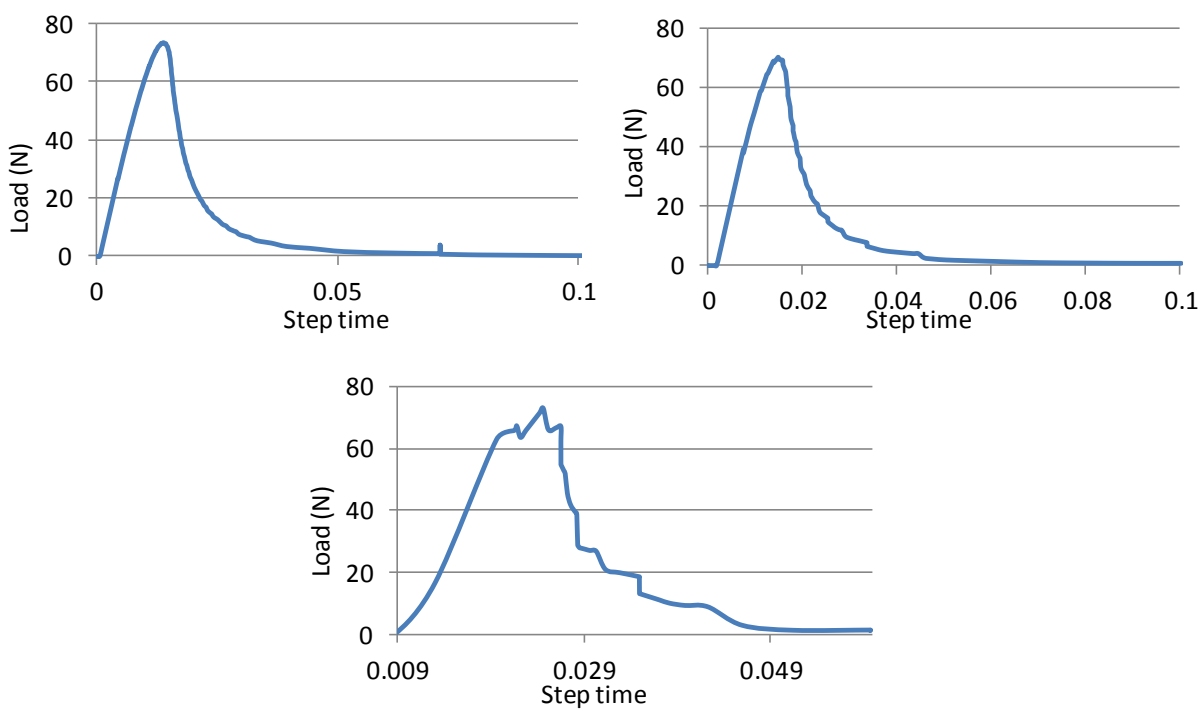

Figure 6.19: Simulated load vs. step time curves for size 3 graphite beam with mesh 1(upper left), mesh 2 (upper right) and mesh 3 (lower)

Table 6.5 gives the experimental and predicted values of the peak load for beam sizes 1, 2 and 3 with the different meshes. For size-1 and 2 beams, the finer meshes (mesh1 and mesh2) gave much smaller % errors compared to the coarse mesh (mesh3). While for the size-3 graphite beam, the % error was similar among the 3 meshes. It can be concluded that a finer mesh can significantly improve the accuracy of XFEM crack simulation.

Table 6.5: Experimental and computational peak loads for both types of meshes and the corresponding errors

	Experimental peak load (N)	Computational peak load (N)			peak load error (%)		
		Mesh1	Mesh2	Mesh3	Mesh1	Mesh2	Mesh3
Size 1	1093	972	1029	1716	11.1	5.9	-57.0
Size 2	187	180	175	249	3.7	6.4	-33.2
Size 3	81	74	70	73	8.6	13.6	9.9

6.3 VERIFICATION OF XFEM FOR SIMULATING 3D FRACTURE

The viability of XFEM in ABAQUS for simulating three-dimensional fractures was evaluated by modeling crack propagation in 3-D graphite beams under three-point bend. The results were compared with the 2-D XFEM results for the same test.

6.3.1 Three Point-Bend Test

The three-point bend test as shown in Figure 6.20 was modeled in ABAQUS. The model was meshed with C3D8 (3D, 8-node, linear, isoparametric) elements. In order to compare the effect of mesh density, two different element sizes, 0.5 mm and 2.0 mm (Figures 6.20 and 6.21), were selected for meshing the central region of the beam. Downward displacement at a constant rate was provided for the top loading bar.

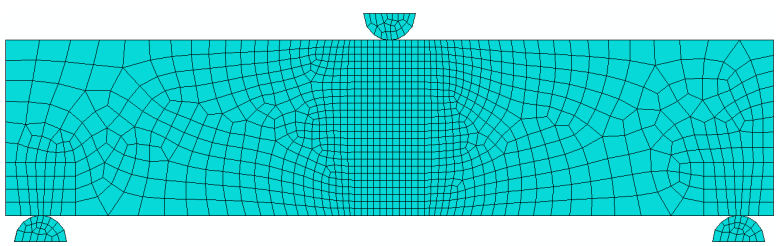

Figure 6.20: Crack simulation model of a beam under three-point bend test with coarse meshing (element size = 2mm in the central region of the beam).

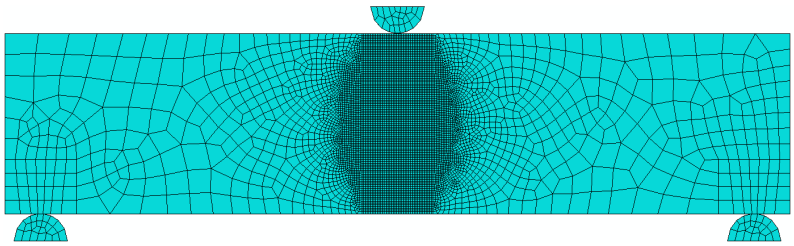

Figure 6.21: Crack simulation model of a beam under three-point bending with fine meshing (element size = 0.5 mm in the central region of the beam)

6.3.2 Results

Figure 6.22 shows the simulated crack propagation for the fine-mesh case. Figure 6.23 shows the load-displacement curves for the 3D models, together with the 2D simulation results. It shows that the fine-mesh model produced a very close prediction of the load curve with the 2D model, indicating that the XFEM in ABAQUS has the capability to simulate 3D fracture in nuclear graphite.

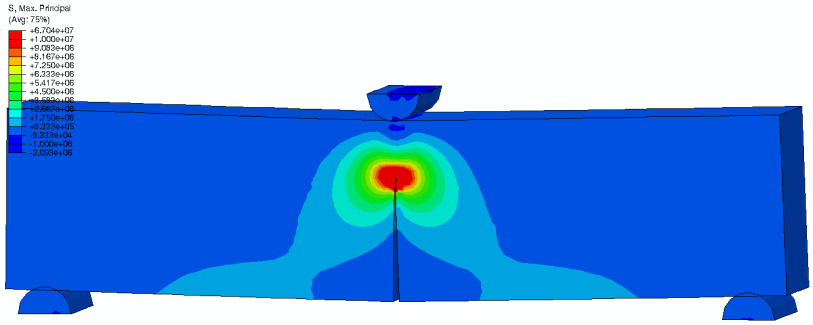

(a) The whole model

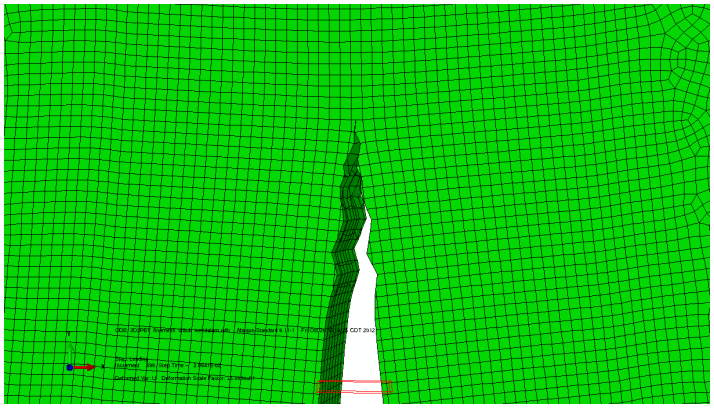

(b) A closer view of the crack tip

Figure 6.22: Crack propagation through a 3-D beam under 3-point bending

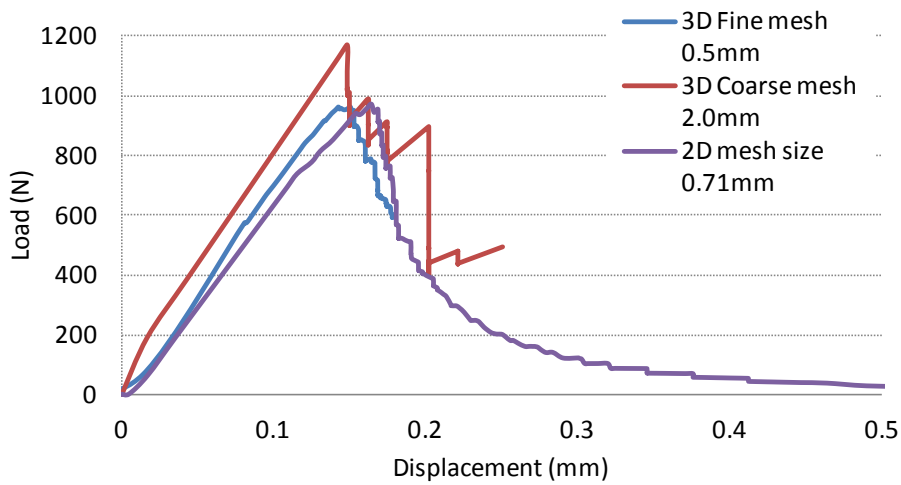

Figure 6.23: Predicted load vs. displacement curves for the three-point bend test with 2D and 3D FE models

6.4 CONCLUSION

It was found that the type of mesh affects the XFEM-predicted direction of crack propagation in a beam under 3-point bending. For a structured mesh the crack propagation was found to be more or less in a straight line, while for an unstructured mesh the crack changed direction as the crack propagated. The direction of the crack affects the load-step time curve. For example, appreciable change in the direction of crack propagation in the size-1 graphite beam with an unstructured mesh (Figure 6.8) lead to an increase in the load in the post-peak region (Figure 6.11). Also, it was found that the load-step time curves were smoother for structured meshes. Thus, the XFEM simulation is sensitive to the type of mesh.

The effect of mesh size on crack propagation modeled by XFEM was studied, and it was found that there was a slight change in the direction of crack propagation for coarser meshes (mesh3) while for finer meshes (mesh1 and mesh2) the crack propagated in an almost straight line without any change in direction. Thus, the size of the mesh could also affect the crack path. It was also noted that the load-step time curves were smooth for finer meshes (mesh1 and mesh2) compared to those for the coarse mesh (mesh3). The peak load errors were smaller for finer meshes (mesh1 and mesh2) than for the coarse mesh (mesh3). Thus, finer mesh leads to more accurate simulation of crack propagation by XFEM. However, the differences between mesh1 and mesh2 were found to be small, indicating that the accuracy of the results was not improved significantly by refining the mesh from mesh2 to mesh 1. It can be concluded that mesh size is also an important factor which can affect the accuracy of the XFEM results quite significantly.

The XFEM technique was explored in simulating crack propagation in 3-dimensional graphite beam models. The peak load was found to be close to the experimental peak load. The load-step time curve was found to be reasonable. Thus, the XFEM technique was found to be promising for simulating 3-dimensional crack propagation.

6.5 REFERENCES

1) Belytschko, T., and T. Black, "Elastic Crack Growth in Finite Elements with Minimal Remeshing," International Journal for Numerical Methods in Engineering, 45, 601-620, (1999).

2) Melenk, J., and I. Babuska, "The Partition of Unity Finite Element Method: Basic Theory and Applications," Computer Methods in Applied Mechanics and Engineering, 39, 289-314, 1996.

3) AbaqusDocumentation 6.11

4) Suyuan Yu, H. Li, C. Wang and Z. Zhang, Probability assessment of graphite brick in the HTR – 10, Nuclear Engineering and Design, 227, 133 – 142, (2004)

5) Haiyan Li, Gyanender Singh, Alex Fok, Effect of Specimen Size on the Fracture Toughness of NBG-18, 4th quarterly report for NEUP-875: Failure Predictions for VHTR Core Components using a Probabilistic Continuum Damage Mechanics Model..

7. MONTE CARLO 2D FAILURE ANALYSIS OF VHTR CORE COMPONENTS

The developed material subroutine UMAT was combined with Extended Finite Element technique (XFEM) to predict the crack initiation and growth in a cylindrical and a prismatic reactor reflector brick under irradiation and high temperature. Monte Carlo 2D failure analysis was performed to evaluate the failure probability of the components. For the analysis of cylindrical brick material was assumed to be ATR-2E graphite. However, for Prismatic reactor two analyses were performed with material as: 1) ATR-2E graphite and 2) IG-11 graphite.

7.1 MONTE CARLO 2D FAILURE ANALYSIS OF A CYLINDRICAL GRAPHITE BRICK

7.1.1 Methods

A cylindrical graphite brick was modeled using the commercial finite element software ABAQUS (see Figure 7.1). The brick was considered to be composed of ATR-2E graphite and subjected to high temperature and irradiation conditions. The internal stresses caused by temperature and irradiation were predicted using the user-defined subroutine UMAT [1]. The XFEM technique was employed simultaneously with UMAT to simulate crack initiation and propagation which would happen when the stresses reached the critical limit.

Monte Carlo failure analysis of the brick was performed by using 30 sets of strength and fracture toughness values (see Appendix) which were calculated according to experimental data. The predicted failure time of the 30 samples were used to evaluate the failure probability of the brick as a function of time.

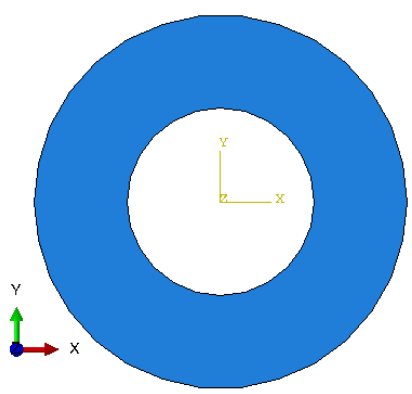

Figure 7.1: Cross-sectional view of a graphite component (hollow cylinder)

7.1.2 Stresses and Fracture Prediction

Since the length of the brick is much longer than its cross-sectional dimensions, plane-strain conditions were assumed for evaluating the stress distribution in the cross section of the brick. The model was divided into XFEM and non-XFEM domains as shown in Figure 7.2. The XFEM domain is the region in which the nodes' degrees of freedom are enriched with special displacement functions to allow for the presence of discontinuities in the elements. The presence of the XFEM domain limits the occurrence of cracking within this region of the brick. Therefore, it prevents multiple cracking in the brick model so as to be in accord with practical observations.

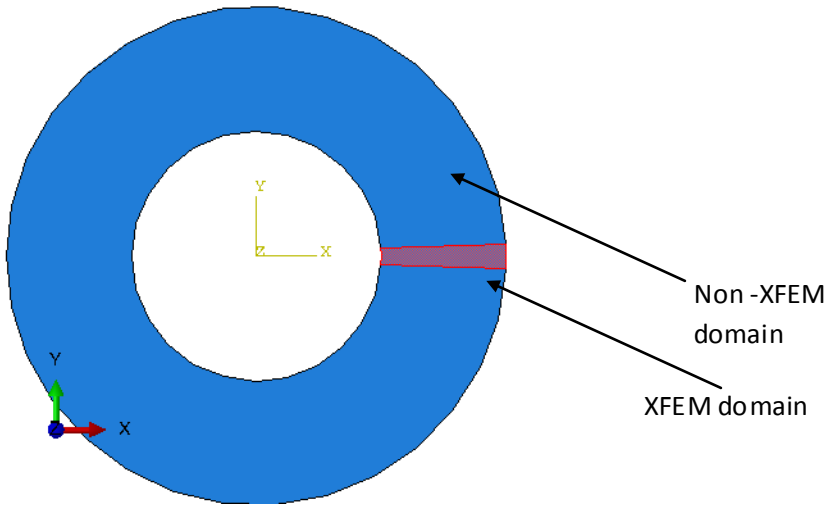

Figure 7.2: Brick model divided into enriched and non-enriched regions.

The model was meshed with 1248 CPE4 (continuum, plane–strain, bilinear, 4-node) elements as shown in Figure 7.3. Figure 7.3 also shows the nodes constrained in x- or y- directions. The temperature was assumed to decrease linearly from 550°C at the inner surface to 300°C at the outer surface (see Figure 7.4). The irradiation dose was assumed to decrease linearly from the inner surface to the outer surface of the brick and increase linearly with time as shown through Equation (1), where 'a' and 'b' are constants (9.6 and 58.7 respectively) and 'r' and 't' are radial distance (m) and time (years) respectively.

$$\text{dose} = (a - br)t \qquad (7.1)$$

The dose distribution in the graphite brick at the end of 30 years is shown in Figure 7.4.

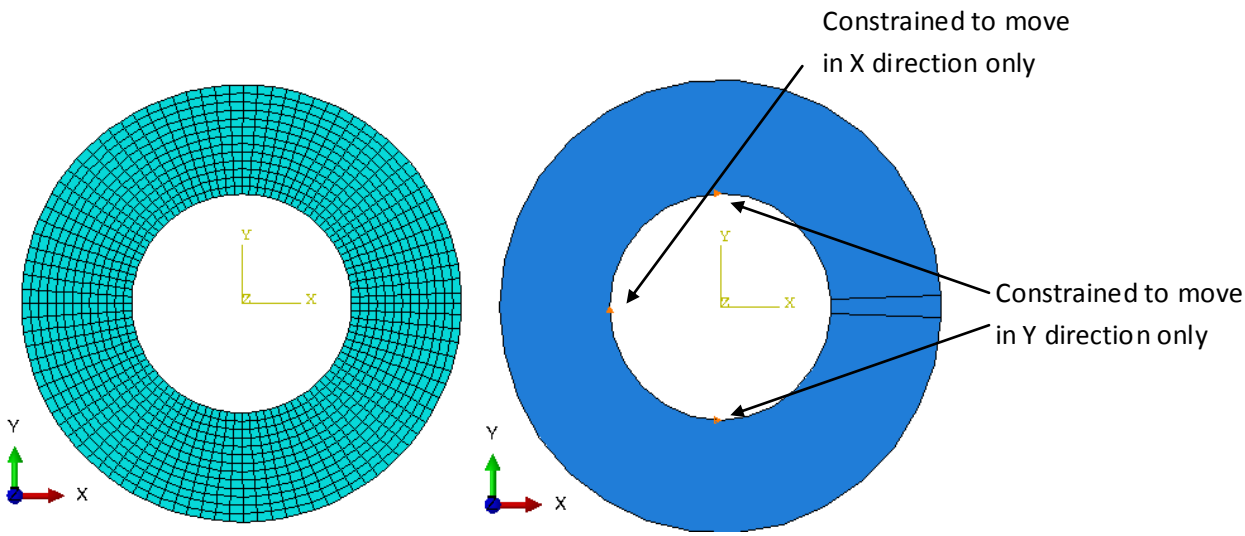

Figure 7.3: Brick meshed with CPE4 elements (left); boundary conditions on the brick (right).

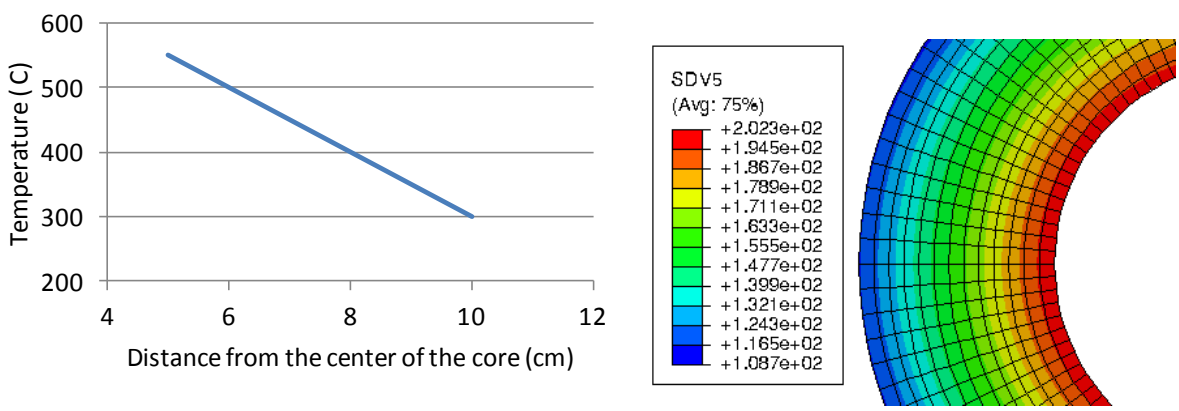

Figure 7.4: Variation of temperature with distance from brick center (left); variation of irradiation dose ($x10^{20}n/cm^2$) with radial distance at the end of 30 years (right)

The brick was considered to be made of ATR-2E graphite. The constitutive model for the brick included the irradiation creep strain, thermal strain, dimensional change strain, and the elastic strain. Further details about the constitutive model are provided in [1]. The material data for ATR-2E were obtained from the work conducted by Gerd Haag [3]. These included the variations of dimensional change strain, coefficient of thermal expansion and Young's Modulus with dose and temperature. The creep modulus was assumed to be a constant.

To simulate fracture of the brick, the maximum principal stress criterion was selected as the damage initiation criterion. The incorporated damage evolution law was based on fracture energy and the softening law was assumed to be linear. Thirty different random values of strength (σ_f) and critical stress intensity factor (K_{IC}) were generated based on the Weibull distribution (See Appendix). The mean values and the corresponding Weibull modulus of σ_f and K_{IC} used for generating the random values are given in Table 7.1. The critical fracture energy (G_{IC}) was calculated from the stress intensity factor K_{IC} using the Irwin relationship for the plane-strain case:

$$G = (1-\upsilon^2)\frac{K^2}{E} \qquad (7.2)$$

where υ and E are Poisson's ratio and Young's Modulus (for virgin graphite), respectively. The variation of fracture energy and strength with irradiation was not considered in the work presented herein. It will be included in the future work.

Table 7.1: The mean value and Weibull Modulus for strength and critical stress intensity factor

	Mean value	**Weibull modulus**
Strength (σ_f)	12. 5 MPa	9
Critical stress intensity factor (K_{IC})	1.0 MPa√m	35

Failure of the brick for the thirty cases was simulated and the failure probability of the graphite brick was evaluated as a function of time using Equation 3 below.

$$\text{Failure probability (time t)} = \frac{\text{Number of specimens failed uptil time t}}{\text{Total number of specimens}} \qquad (7.3)$$

7.1.3 Results and Discussion

The finite element model was run in ABAQUS for each of the thirty sets of fracture energy and strength. Figure 7.5 shows the maximum principal stress distribution in the graphite brick at the end of 5, 10, 15, 20, 25 and 30 years for specimen 1 (σ_f = 14.3 MPa, G_{IC} = 92.6 J/m^2).

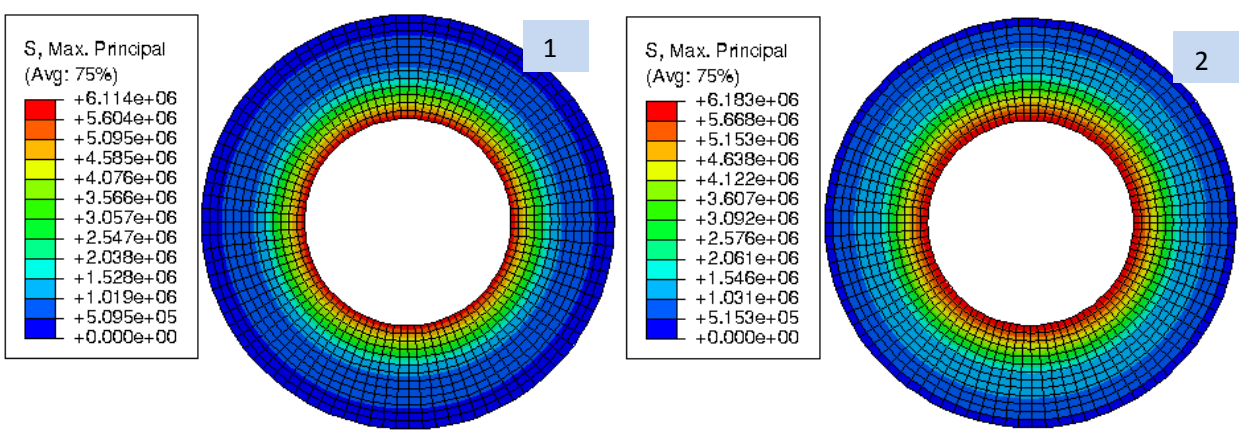

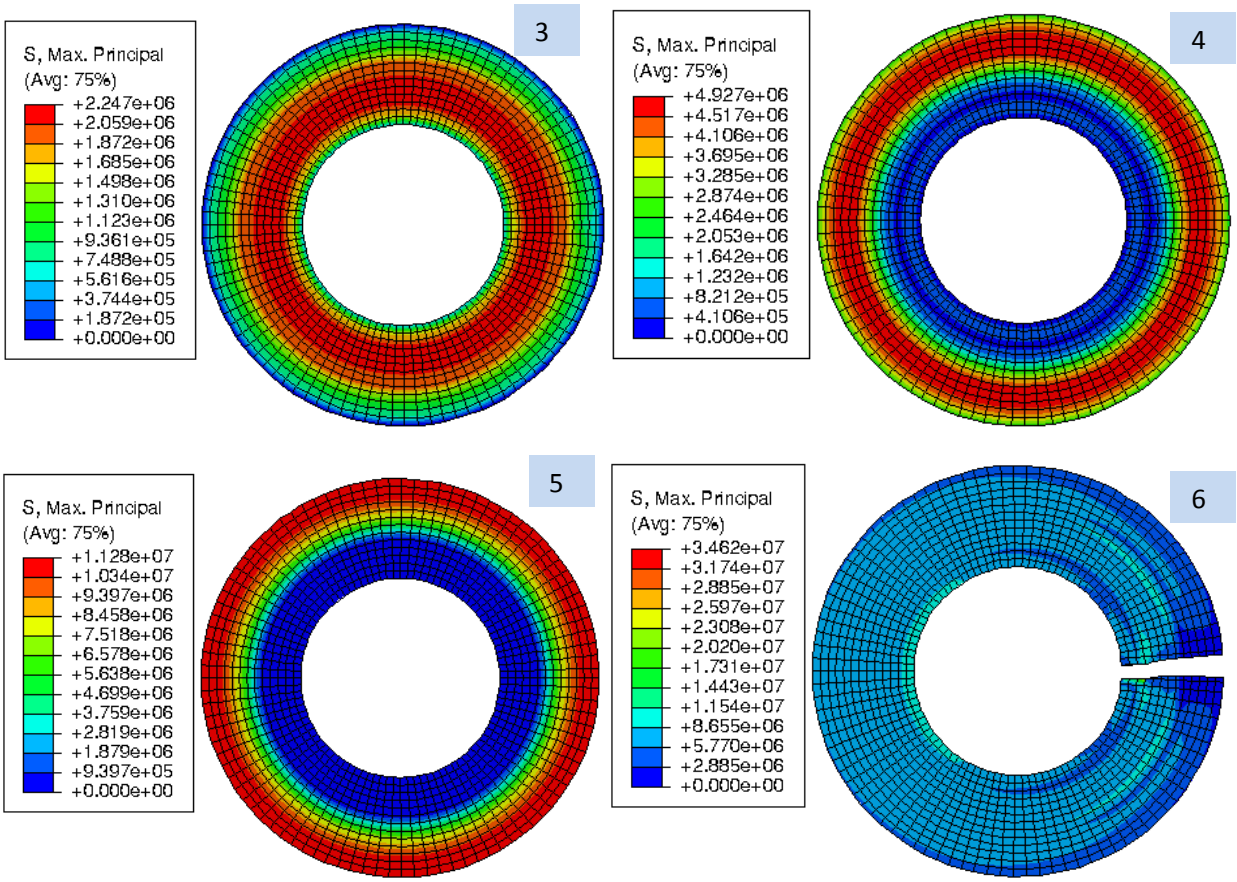

Figure 7.5: Distribution of maximum principal stress at the end of 5, 10, 15, 20, 25 and 30 years shown in pictures numbered 1, 2, 3, 4, 5 and 6 respectively for case 1 (σ_f = 14.3 MPa, G_{IC} = 92.6 J/m^2).

Figure 7.6 shows the variation of hoop stress at the inner and outer surfaces of the brick with time for the same specimen. It can be seen that the sudden temperature rise at the start of the reactor operation caused development of thermal stresses in the graphite brick. The thermal stresses are compressive at the inner surface and tensile at the outer surface. Due to irradiation creep and irradiation effect the thermal stresses are released and at around 2 years the brick is under negligible stress. Then continued irradiation resulted in tensile stresses in the inner region and compressive stresses in the outer region of the brick. The turn-around of stresses at the inner and outer surfaces takes place at the 8th and 10th years, respectively, and at these time points the magnitude of the stresses starts decreasing. At the 14th year, the stresses at the inner surface change from tensile to compressive; and at the 19th year the stresses at the outer surface change from compressive to tensile and continue to increase.

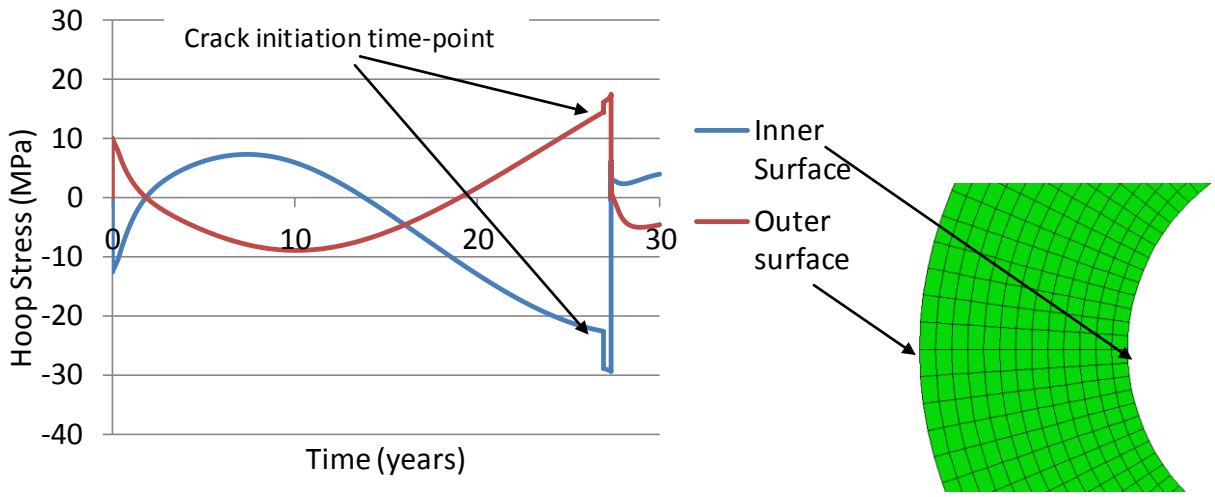

Figure 7.6: Variation of hoop stress with time at the inner and outer surfaces of the brick for specimen 1 (σ_f = 14.3 MPa, G_{IC} = 92.6 J/m^2).

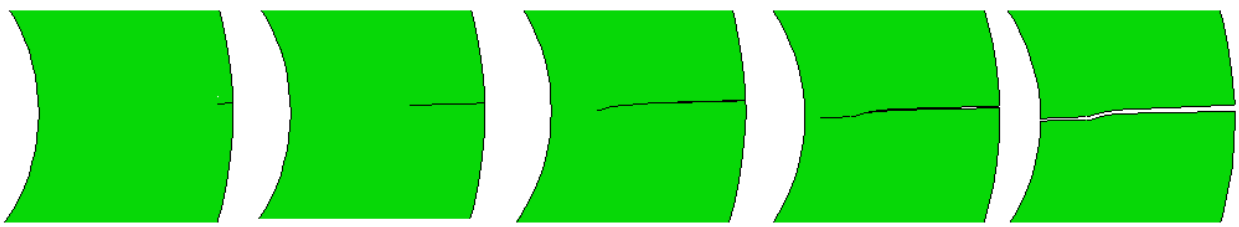

Figure 7.7: Crack propagation with time through the thickness of a graphite brick model.

Figure 7.7 shows the crack propagation through the thickness of the graphite brick. For each specimen, the times at which crack initiates in the brick, penetrates through half of the thickness and penetrates through all the thickness of the brick were obtained and listed in Table 7.2. the crack initiation time was found to be very close to the time at which the crack penetrated through half of the thickness of the brick, the failure time is defined as equal to the crack initiation time. It was found that cracking developed in 2 specimens (specimens 8 and 26) within the first year. Such unusually early failure of these specimens can be attributed to their very low strengths (8.98 and 8.77 MPa), which were the lowest within the group. The thermal stresses developed in the graphite bricks during the start of the reactor were about 10 MPa and were greater than the strength of these two specimens. Therefore, it was the thermal stresses that caused the failure of these two graphite bricks.

Table 7.2: The predicted times at which crack initiates, penetrates through half of the thickness and penetrates through all the thickness in the brick

Specimen number	G (J/m^2)	Strength (Pa)	Crack initiation time (years)	Half radial distance penetration time (years)	Full radial distance penetration time (years)
1	92.585	14342646.79	26.92	26.92	27.34
2	110.1351	12852079.07	26.12	26.13	26.39
3	92.1204	14161890.22	26.82	26.83	27.32
4	101.0609	13732899.95	26.62	26.63	26.98
5	110.8948	10419269.28	24.72	24.72	
6	107.1619	11172630.51	25.12	25.13	25.36
7	102.6631	12693836.63	26.02	26.03	26.45
8	88.3286	8981793.07	1		
9	87.3517	14305797.38	26.92	26.92	26.92
10	109.4413	12233736.59	25.72	25.82	26.04
11	86.4567	12448451.15	25.82	25.83	26.16
12	88.3697	10795081.39	24.92	24.93	25.18
13	103.7269	10612426.46	24.82	24.83	25.03
14	96.9803	13239377.72	26.32	26.33	26.6
15	109.7879	12040452.93	25.62	25.63	25.88
16	104.7849	12207989.68	25.72	25.73	26.04
17	91.9684	11400006.43	25.32	25.33	25.55
18	97.2272	11100184.66	25.12	25.13	25.34
19	88.0822	10857574.58	25.02	25.03	25.26
20	100.5854	12855686.94	26.12	26.13	26.37
21	113.1924	11245732.42	25.22	25.23	25.4
22	95.2821	11360276.52	25.22	25.23	25.53
23	90.6435	13357064.47	26.42	26.43	26.76
24	100.0969	13594588.63	26.52	26.53	26.86
25	98.2031	12007471.63	25.62	25.63	25.84
26	98.5844	8767569.468	1		
27	105.2695	12604331.18	25.92	26.02	26.25
28	100.5909	11662426.52	25.43	25.42	25.63
29	109.1556	13073066.26	26.22	26.32	26.59
30	99.4847	10876902.64	25.02	25.03	25.19

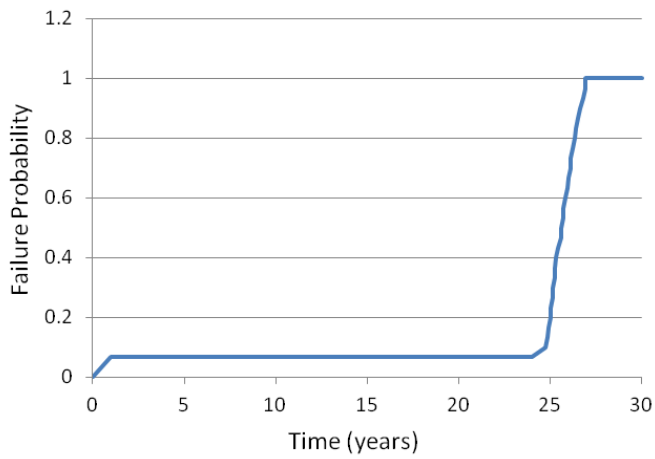

Figure 7.8: Failure probability of ATR-2E graphite brick vs. time

Finally, the variation of failure probability of the ATR-2E graphite brick as a function of time was obtained according to Equation (3), as shown in Figure 7.8. It can be seen that most brick specimens failed during the time range of 24-27 years. Except specimens 8 and 26, whose failure were caused by thermal stresses, in all the other specimens cracking occurred at the outer surface of the brick and propagated towards the inner surface. Crack initiation at the outer surface can be explained from Figure 7.6, which shows that the maximum principal stress occurs at the outer surface of the brick, making it most susceptible to fracture. When the maximum principal stress reaches the critical limit, a crack develops. It can be noted from Table 7.2 that the brick specimens with higher strengths had longer lives. The failure probability vs. time plot shown in Figure 7.8 shows that the failure probability is low (0.067) up till 24 years and rises steeply thereafter.

7.1.4 Conclusion

Thirty different random values of strength and fracture energy based on the Weibull distribution were generated for ATR-2E graphite. Due to the unavailability of dose and temperature distribution data, assumptions were made regarding their spatial distributions. For each of the thirty cases, stresses and cracking were simulated for the cylindrical graphite brick. For 28 cases, cracking initiated at the outer surface of the brick and propagated rapidly through the thickness towards the inner surface. Most of the bricks failed in the time range of 24-27 years. However, in two cases, the brick failed within the first year due to thermal stresses. The failure probability of ATR-2E graphite bricks was found to be low up till 24 years and rise steeply thereafter.

7.2 MONTE CARLO 2D FAILURE ANALYSIS OF A PRISMATIC REFLECTOR GRAPHITE BRICK

7.2.1 Methods

A prismatic reflector graphite brick was modeled using the commercial finite element software ABAQUS. Figure 7.9 shows the location of the brick in the prismatic reactor core and its dimensional details. Two types of graphite were considered for the numerical analysis of the brick: ATR-2E and IG-11. Figure 7.10 shows the computer model of the reflector brick used for numerical analysis. For the first case the brick was considered to be composed of ATR-2E graphite and subjected to high temperature and irradiation conditions. The irradiation data were obtained from reference [4]. The internal stresses caused by temperature and irradiation were predicted using the user-defined material subroutine UMAT [1]. The XFEM technique was employed simultaneously with UMAT to simulate crack initiation and propagation when the stresses reached the critical limit [2].

Monte Carlo failure analysis of the brick was performed by using 30 sets of strength and fracture toughness values (see Appendix) which were calculated according to experimental data [3]. The predicted time to failure the 30 samples were used to evaluate the failure probability of the reflector brick as a function of time.

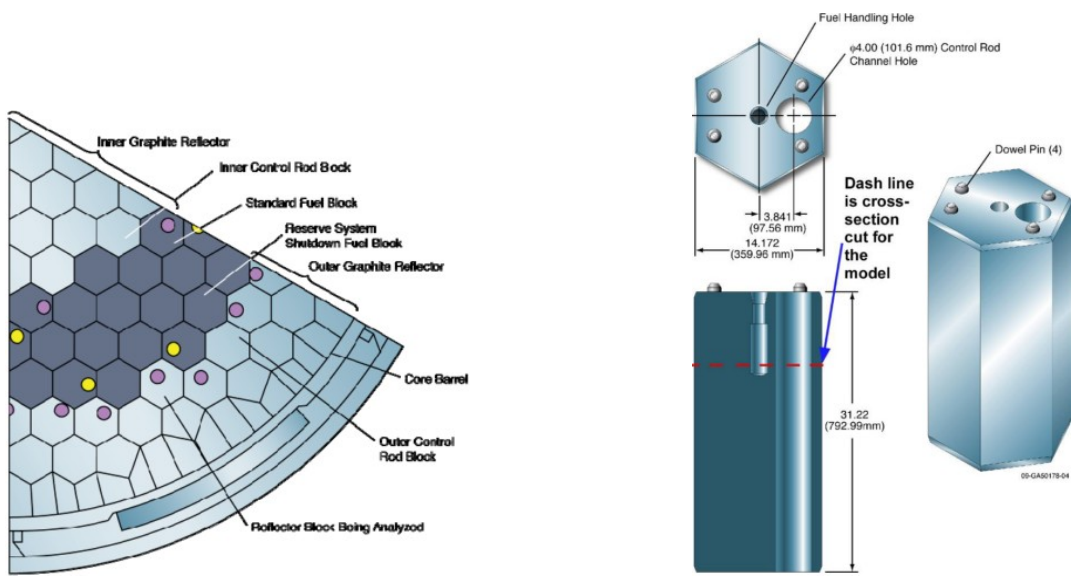

Figure 7.9: Location and dimensional details of prismatic reflector block considered for failure analysis (source: [4])

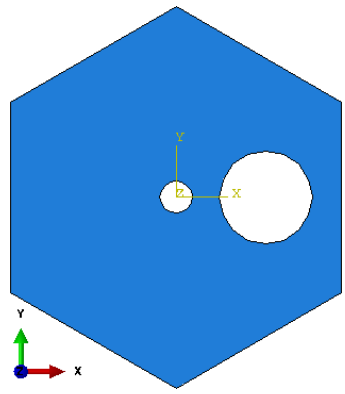

Figure 7.10: Prismatic reactor core brick model.

7.2.2 Stresses and Fracture Prediction

Since the length of the reflector brick is much larger than its cross-sectional dimensions, plane-strain conditions were assumed for evaluating the stress distribution in the cross section of the brick. The model was divided into XFEM and non-XFEM domains as shown in Figure 7.11. In the XFEM domain the nodes' degrees of freedom were enriched with special displacement functions to allow for the presence of discontinuities in the elements. The occurrence of cracking was limited to this region of the brick, thus preventing multiple cracking in the brick model.

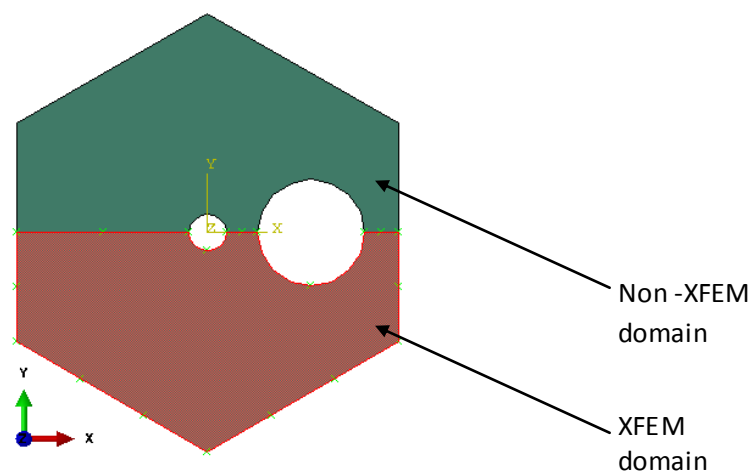

Figure 7.11: Brick model divided into enriched and non-enriched regions.

The model was meshed with 3625 CPS4 (continuum, plane–strain, bilinear, 4-node) elements with 3756 nodes as shown in Figure 7.12. Figure 7.12 also shows the nodes constrained in the x or y directions.

The irradiation dose distribution was based on the operating conditions for a reflector block in the Ft. St. Vrain reactor as presented in [4]. Due to unavailability of temperature distribution data for the prismatic reflector brick, a temperature distribution based on simple assumptions was used for the numerical analysis (see Figure 7.13).

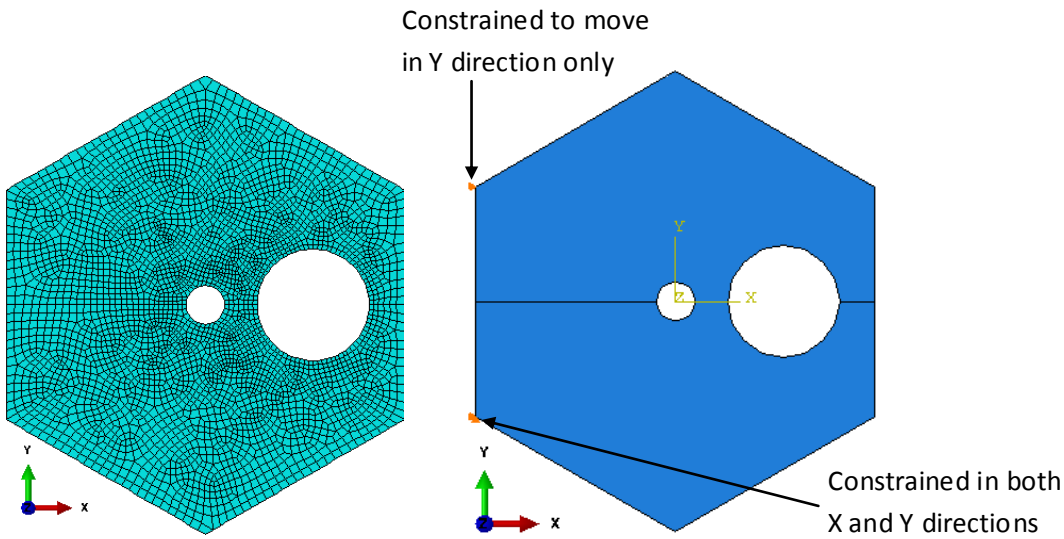

Figure 7.12: Brick meshed with CPS4 elements (left); boundary conditions on the brick (right).

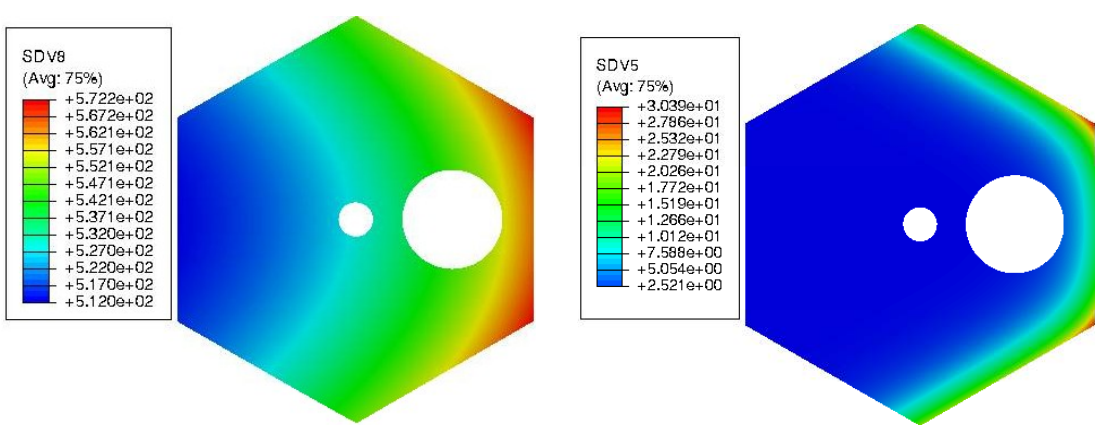

Figure 7.13: Temperature distribution (left) and irradiation dose distribution ($x10^{20}n/cm^2$) (right) in the prismatic reactor core brick at the end of 6 years

The constitutive model for the brick included the irradiation creep strain, thermal strain, dimensional change strain, and the elastic strain. Further details about the constitutive model are provided in [1]. The material data for ATR-2E were obtained from the work conducted by Gerd Haag [3]. These included the variations of dimensional change strain, coefficient of thermal expansion and Young's Modulus with dose and temperature. The creep modulus was assumed to be a constant.

The maximum principal stress criterion was selected as the damage initiation criterion. For simulating cracking, the damage evolution law selected was based on the critical fracture energy and the softening law was assumed to be linear. Using the Weibull distribution, thirty different values of strength (σ_f) and critical stress intensity factor (K_{IC}) were generated randomly using MATLAB (See Appendix). The mean values and the corresponding Weibull modulus of σ_f and K_{IC} used for generating the random values are given in Table 7.3. The critical fracture energy (G_{IC}) was calculated from the stress intensity factor K_{IC} using the Irwin relationship for the plane-strain case (Equation 7.2). The variation of fracture energy and strength with irradiation was not considered in the work presented herein and will be included in future work.

Table 7.3: The mean value and Weibull Modulus for strength and critical stress intensity factor

	Mean value	**Weibull modulus**
Strength (σ_f)	12. 5 MPa	9
Critical stress intensity factor (K_{IC})	1.0 MPa√m	35

Failure of the prismatic brick for the thirty cases was simulated and the failure probability of the graphite brick was evaluated as a function of time using Equation 7.3.

7.2.3 Results and Discussion

The finite element model was run in ABAQUS for each of the thirty sets of fracture energy and strength. Figure 7.14 shows the maximum principal stress distribution in the graphite brick at the end of 2, 5, 8, 11, 11.6 and 17 years for specimen 1 (σ_f = 15.1 MPa, G_{IC} = 110.3 J/m^2).

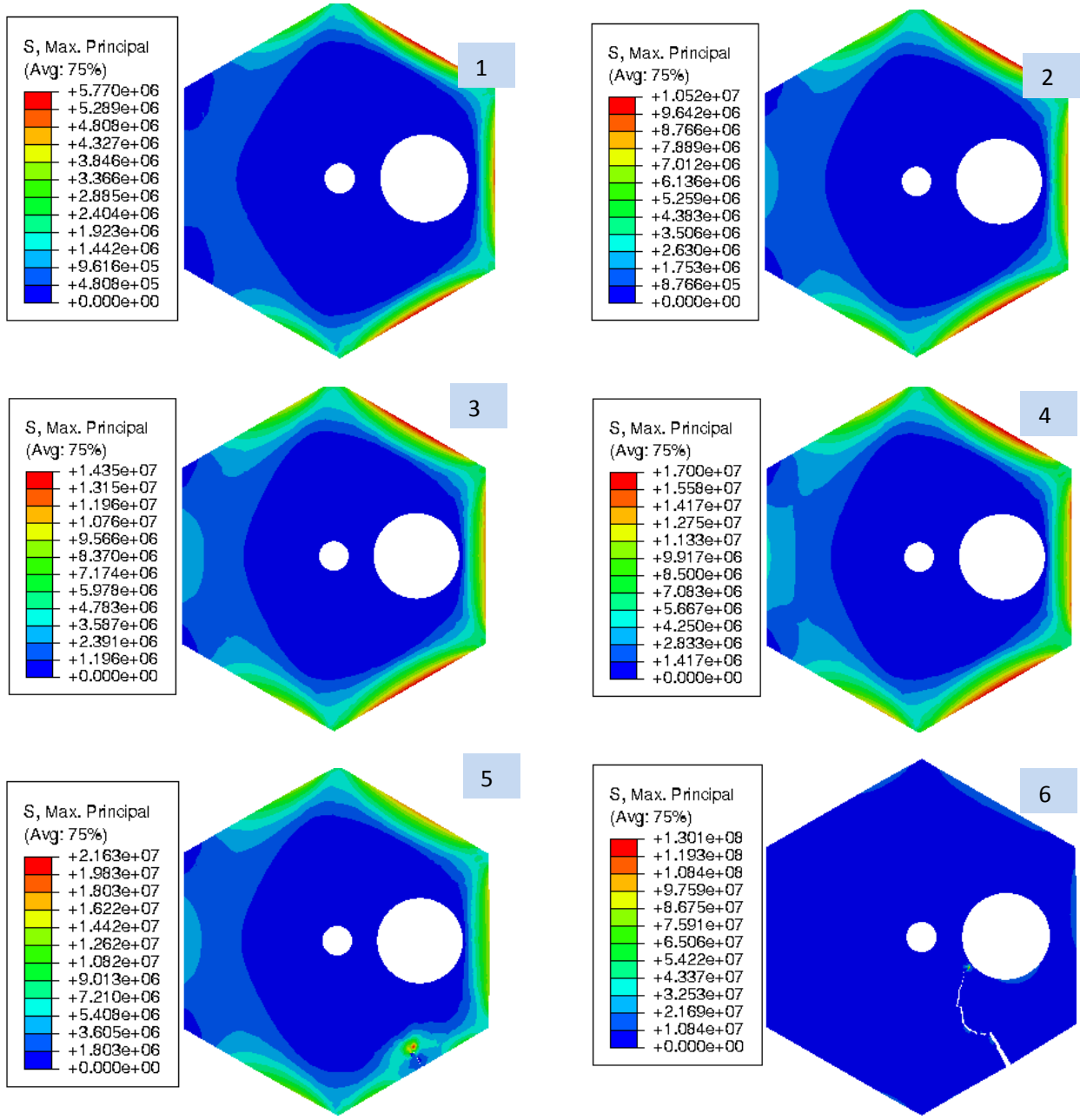

Figure 7.14: Distribution of maximum principal stress with ATR-2E graphite at the end of 2, 5, 8, 11, 11.6 and 17 years shown in pictures numbered 1, 2, 3, 4, 5 and 6 respectively for case 1 (σ_f = 15.1 MPa, G_{IC} = 110.3 J/m^2).

Figure 7.15 shows the variation of the maximum principal stress with time at two different locations in the reflector brick for a specimen. With an increase in irradiation, the maximum principal stress increased until crack initiated. Due to cracking in the brick, stresses were relieved which resulted in decrease in the stresses at the two locations. Node B was nearer to the crack location and experienced greater stress relaxation. So, the decrease in stress was greater at node B. The crack was arrested and the stresses again increased in magnitude. But as the crack began to propagate again, stresses again decreased in magnitude. The life-time of this particular specimen was found to be 11.6 years.

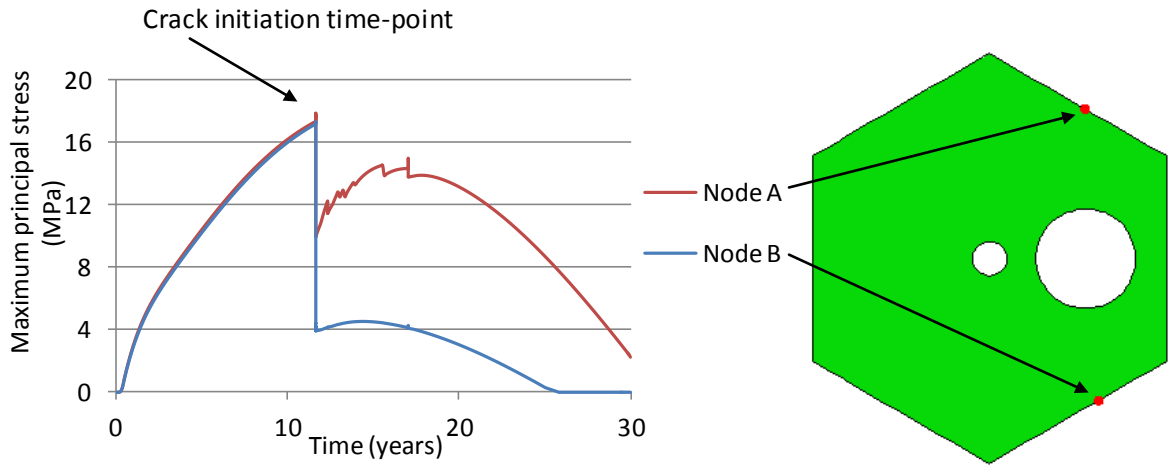

Figure 7.15: Variation of maximum principal stress with time at the inner and outer surfaces of the brick for specimen 1 (σ_f = 15.1 MPa, G_{IC} = 110.3 J/m^2).

Figure 7.16 shows the crack propagation through a reflector brick model. For each specimen the time at which crack initiated was obtained and listed in Table 7.4. It was found that cracks initiated at the right lower edge (see Figure 7.16) of the specimen and propagated towards the control rod channel. Initiation of cracks from this particular location could be attributed to the high dose gradient between the control rod channel and the brick edge which led to the development of high stresses in that location. It indicates that the outer surface of the reflector brick, which is in contact with a fuel block, is more susceptible to failure than the inner free surfaces of the control rod channel and fuel handling hole. It was also observed that the crack propagation was quite fast initially and most of the path was traversed by the crack shortly after initiation. It indicates that the prismatic reactor core reflector brick made of ATR-2E graphite will fail as soon as a crack appears in it.

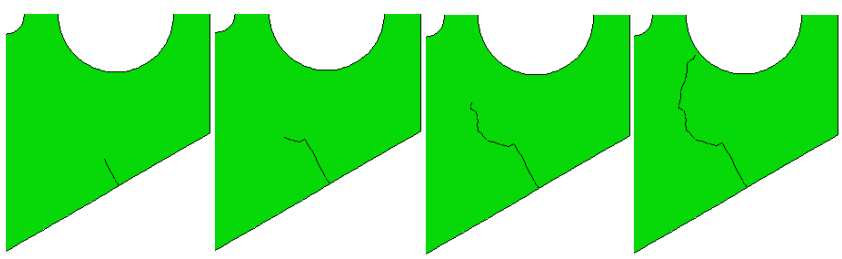

Figure 7.17: Crack propagation with time through the thickness of a graphite brick model.

Table 7.4: The predicted times at which crack initiates, penetrates through half of the thickness and penetrates through all the thickness in the brick

Specimen number	G (J/m^2)	Strength (MPa)	Crack initiation time (years)
1	96.52	13.67	9.82
2	92.59	8.71	5.02
3	110.14	15.07	11.6
4	92.12	10.74	6.82
5	101.06	10.46	6.52
6	110.89	10.05	6.22
7	107.16	13.82	10.0
8	102.66	12.38	8.42
9	88.33	12.92	8.92
10	87.35	10.58	6.62
11	109.44	12.26	8.22
12	86.46	9.61	5.82
13	88.37	13.26	9.32
14	103.73	12.91	8.92
15	96.98	13.45	9.52
16	109.79	13.50	9.62
17	104.78	10.05	6.52
18	91.97	11.69	7.72
19	97.23	11.81	7.82
20	88.08	13.45	9.52
21	100.59	10.19	6.32
22	113.19	11.51	7.52
23	95.28	12.56	8.62
24	90.64	11.95	7.92
25	100.10	12.37	8.42
26	98.20	13.89	10.0
27	98.58	13.00	9.02
28	105.27	13.57	9.72
29	100.59	13.25	9.32
30	109.16	13.00	9.02

Failure of the reflector brick specimens was governed mainly by their strength: bricks with higher strength had longer lifetime while bricks with lower strength failed in shorter time. The brick specimen with the lowest strength of 8.7 MPa had the shortest lifetime of 5 years while the brick with the greatest strength of 15.1 MPa had the longest lifetime of 11.6 years. Finally, the variation of failure probability of the ATR-2E graphite brick as a function of time was obtained according to Equation (2), as shown in Figure 7.17. There was no failure observed before 5 years, so the failure probability is zero during this initial period. Most reflector brick specimens failed during the time range of 6-10 years, therefore the failure probability rose steeply within this time range. After about 10 years the failure probability was almost equal to 1.

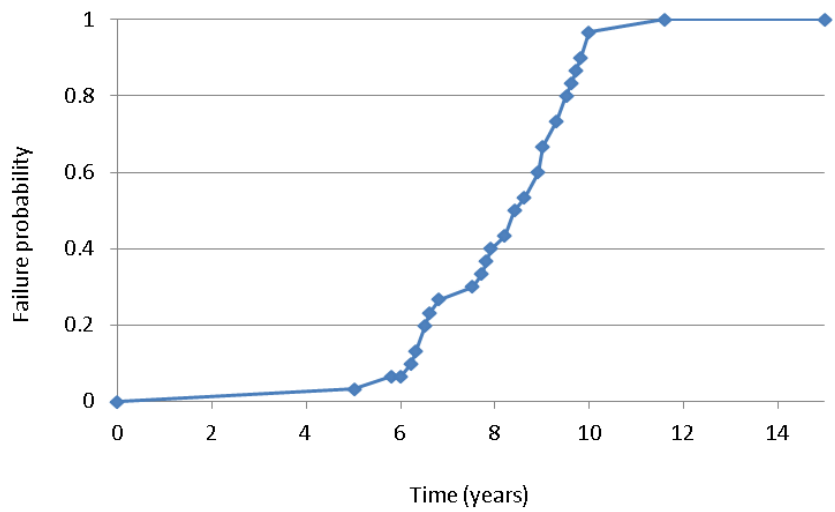

Figure 7.17: Failure probability of ATR-2E graphite brick vs. time.

7.2.3 2D Failure Analysis of Prismatic Reflector Brick (IG-11 Graphite)

7.2.3.1 Methods

The prismatic reflector brick model, as described earlier, was then assigned IG-11 graphite material properties. Since not all the properties for IG-11 graphite could be found in the literature, a combination of IG-11 and IG-110 graphite properties were used along with some assumptions for the cases for which no data were available. The details about the properties for IG-11/110 graphite are provided in [5]. The same temperature and irradiation conditions, as given for ATR-2E graphite brick, were assigned to the model. The internal stresses caused by the temperature and irradiation were predicted using the user-defined material subroutine UMAT [1]. The XFEM technique was employed simultaneously with UMAT to simulate crack initiation and propagation which would happen when the stresses reached the critical limit. Besides changing the material properties from ATR-2E to IG-11/110 graphite, no other changes were made in the numerical model.

7.2.3.2 Results and Discussion

The finite element model was again run in ABAQUS. Figure 7.18 shows the maximum principal stress distribution in the graphite brick at the end of 5, 15, 25 and 30 years. The stresses were found to be maximum at the end of 30 years. The peak maximum principal stress was found at the inner surface of the control rod channel (node B shown in Figure 7.19) and was calculated to be 10.4 MPa. As can seen in Figure 7.18, there was no fracture in the reflector brick during the operation time of 30 years. There was no failure because the maximum principal stress did not exceed the strength of the material, which was around 25 MPa, during the course of the reactor operation.

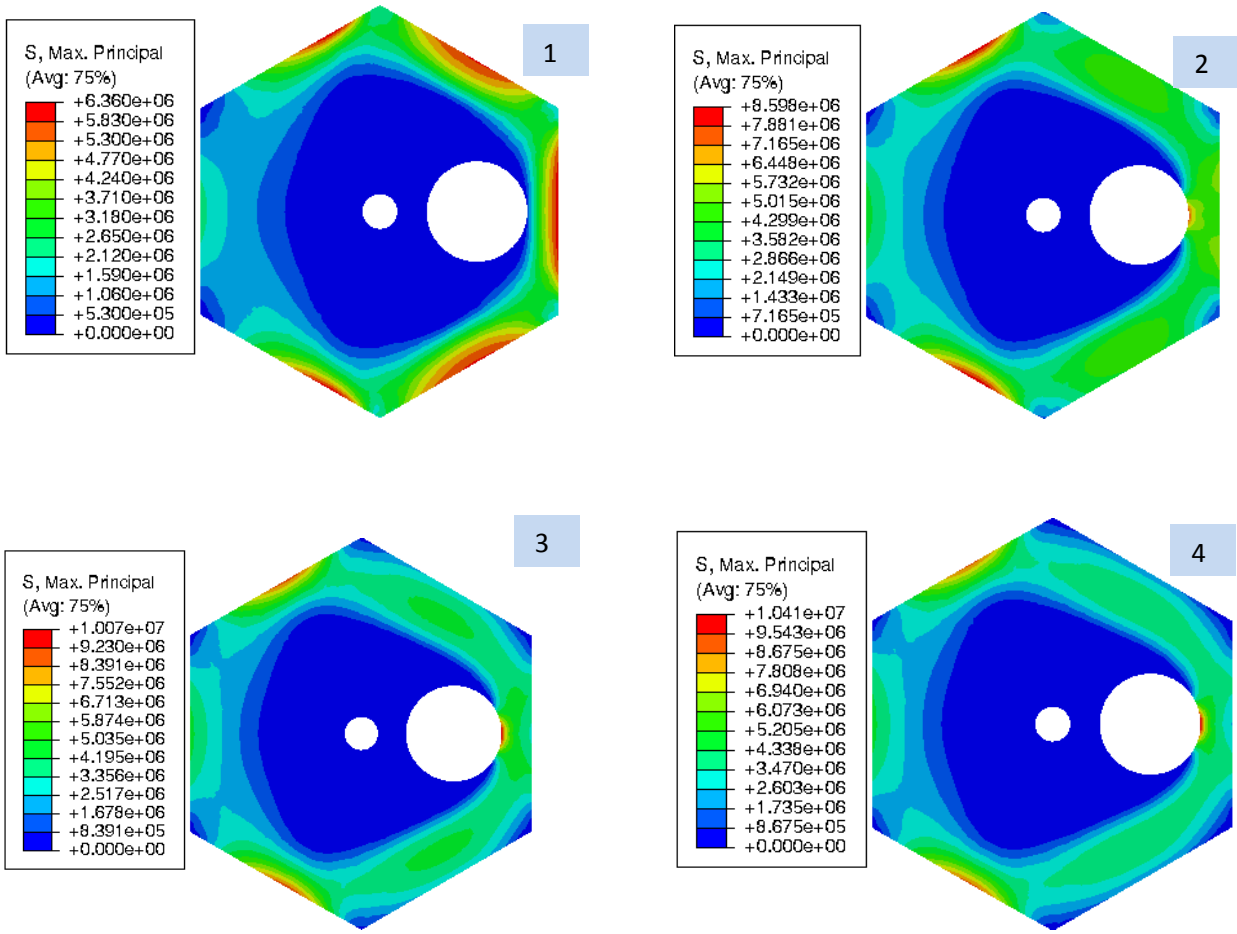

Figure 7.18: Distribution of maximum principal stress with IG-11 graphite at the end of 5, 15, 25 and 30 years shown in pictures numbered 1, 2, 3 and 4 respectively in the prismatic reactor core brick.

Figure 7.19 shows the variation of the stress in the y direction with time at two locations represented by nodes A and B. At the start of the reactor operation, the stress was compressive at both the nodes, which was due to thermal strains caused by a rise in temperature of the core. Thereafter, the stress at node A became tensile in nature and continued to rise until about 4.5 years, at which point the stress begins to decrease in magnitude. The decrease in stress continued for the remaining duration of the reactor operation. However, the stress at node B showed a different trend. Following the development of compressive thermal stresses at the start of reactor operation, the stress at node B continued to remain compressive and increased further in magnitude until about 2 years. After that, the stress began to decrease in magnitude and turned tensile in nature at around 4.3 years. Thereafter, the stress at node B continued to increase with time.

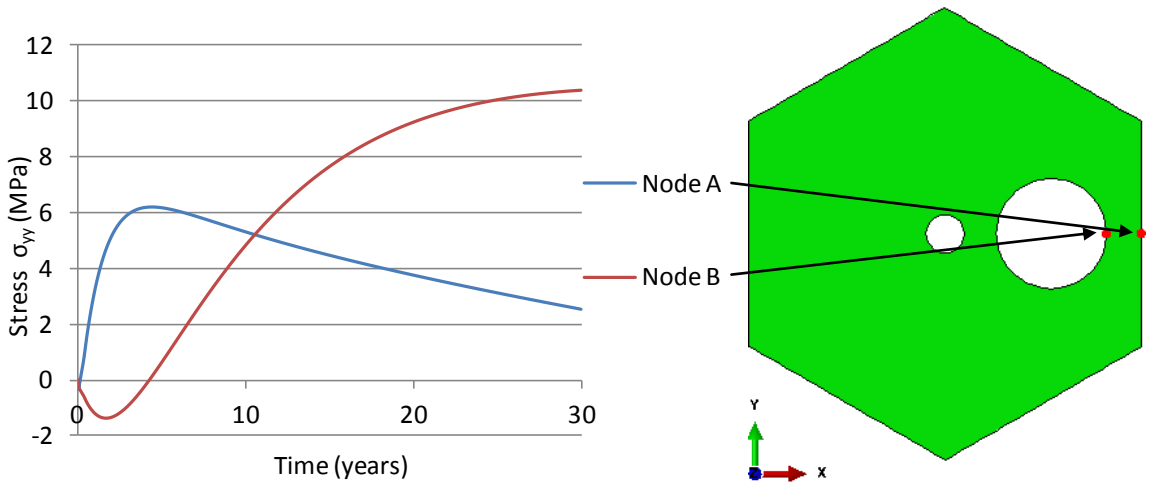

Figure 7.19: Variation of σ_{yy} with time at the two locations of the brick.

7.2.4 Conclusion

Two materials, ATR-2E and IG-11/110, were considered for the failure analysis of the prismatic core reflector brick. For ATR-2E graphite thirty different random values of strength and fracture energy were generated based on the Weibull distribution. The irradiation dose distribution data used in the numerical analysis were based on the operating conditions for the reflector block in the Ft. St. Vrain reactor. The temperature distribution data was unavailable and assumptions were made regarding its spatial distribution. For each of the thirty cases, stresses and cracking were simulated for the reflector brick. For all the cases considered cracking initiated at the outer surface of the brick and propagated rapidly through the thickness towards the control rod channel. Since no failure was observed before 5 years the failure probability was zero during this time range. Most of the bricks failed in the time range of 6-10 years. Therefore, the failure probability rose steeply after 5 years of reactor operation. All the specimens failed by the end of 11.6 years.

Failure analysis was also performed for the prismatic core reflector brick made of IG-11/110 material using the same brick model as used for ATR-2E brick failure analysis. For IG-11/110 brick no fracture was observed during its operation time of 30 years. The reason for this was that the maximum principal stresses did not exceed the strength of the material at any time during the course of reactor operation. However, it was found that the peak maximum principal stress occurred at the inner surface of the control rod channel, indicating this region to be most susceptible to failure.

7.3 References

[1] Gyanender Singh, Haiyan Li, Alex Fok. Modeling the Residual Stresses in VHTR Core Components, 4th quarterly report for NEUP-875: Failure Predictions for VHTR Core Components using a Probabilistic Continuum Damage Mechanics Model.

[2] Gyanender Singh, Haiyan Li, Alex Fok. Assessing the Viability of Extended Finite Element Method (XFEM) for Modeling Fracture in Graphite, 7th quarterly report for NEUP-875: Failure Predictions for VHTR Core Components using a Probabilistic Continuum Damage Mechanics Model.

[3] Gerd Haad, Properties of ATR-2E Graphite and Property Changes Due to Fast Neutron Irradiation, Institute for Safety Research and Reactor Technology, 2005.

[4] Modeling Mechanical Behavior of a Prismatic Replaceable Reflector Block, Robert L. Bratton, Idaho National Laboratory, Next Generation Nuclear Plant Project, INL/EXT-09-15868, 2009.

[5] Gyanender Singh, Haiyan Li, Alex Fok. Calculating the Residual Stresses in VHTR Core Components, 6th quarterly report for NEUP-875: Failure Predictions for VHTR Core Components using a Probabilistic Continuum Damage Mechanics Model.

8. MONTE CARLO 3D FAILURE ANALYSIS OF VHTR CORE COMPONENTS

Monte Carlo 3D failure analyses were performed to evaluate the failure probability of a cylindrical graphite brick and a prismatic reflector graphite brick as a function of time.

8.1 MONTE CARLO 3D FAILURE ANALYSIS OF A CYLINDRICAL BRICK

A cylindrical ATR-2E graphite brick was modeled using the commercial finite element software ABAQUS (see Figure 8.1). The internal stresses caused by temperature and irradiation were predicted using the user-defined subroutine UMAT [1]. The XFEM technique was employed simultaneously with UMAT to simulate crack initiation and propagation which would happen when the internal stresses reached the critical limit.

Monte Carlo failure analysis of the brick was performed by using 30 sets of strength and fracture toughness values (see Appendix) to consider the variations in material properties. These 30 sets of data were generated according to the mean values of strength and fracture toughness and their statistical characteristics of ATR-2E obtained from experiments [3]. The predicted failure time of the 30 samples were then used to evaluate the failure probability of the brick as a function of time.

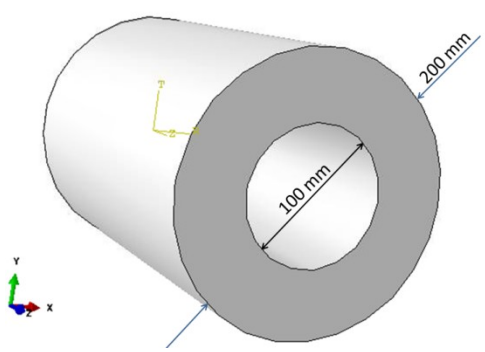

Figure 8.1: Cylindrical graphite component

8.1.1 FE simulation

The brick model was divided into XFEM and non-XFEM domains as shown in Figure 8.2. The XFEM domain was the region in which the nodal degrees of freedom were enriched with special displacement functions to allow for the presence of discontinuities in the elements. Cracking was restricted to the XFEM domain. Therefore, it prevented multiple cracking in the brick model so as to be in accord with practical observations.

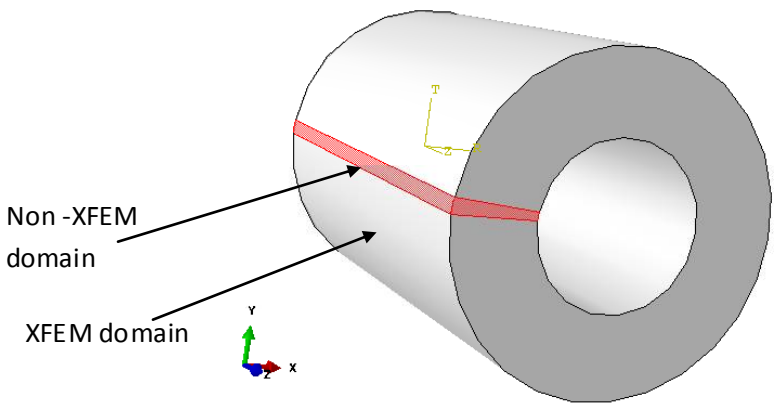

Figure 8.2: XFEM and non-XFEM domains of brick model.

The brick was meshed with 11520 C3D8 (continuum 3D 8-node linear isoparametric) elements as shown in Figure 8.3. Figure 8.3 also shows the boundary conditions on the model.

The temperature was assumed to decrease linearly from 550°C at the inner surface to 300°C at the outer surface (see Figure 8.4). The irradiation dose was assumed to decrease linearly from the inner surface to the outer surface of the brick and increase linearly with time as given by Equation (1):

$$\text{dose} = (a - br)t \qquad (8.1)$$

where 'a' and 'b' are constants (9.6 and 58.7, respectively) and 'r' and 't' are the radial distance (m) and time (years) respectively. The dose distribution in the graphite brick at the end of 20 years of operation is shown in Figure 8.4.

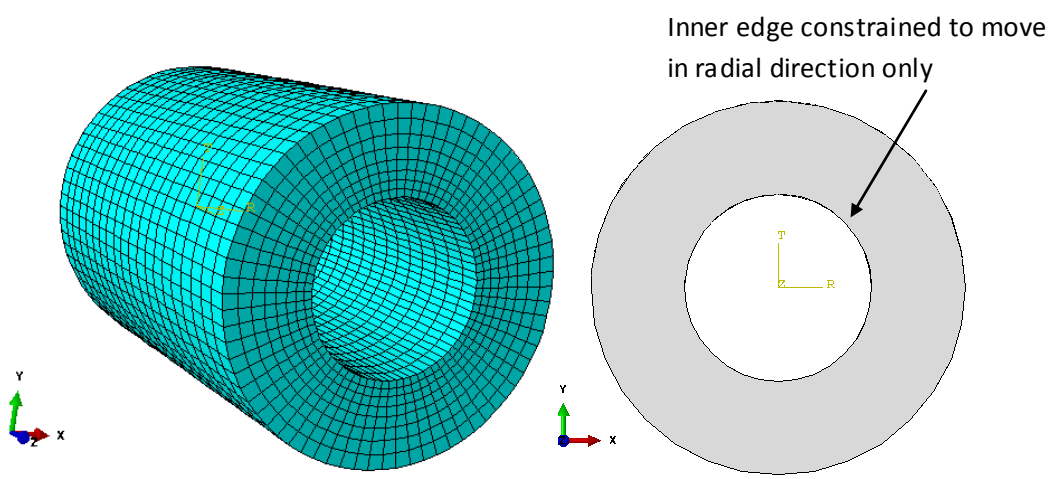

Figure 8.3: Mesh of 3D FE model (left); boundary conditions on the brick (right).

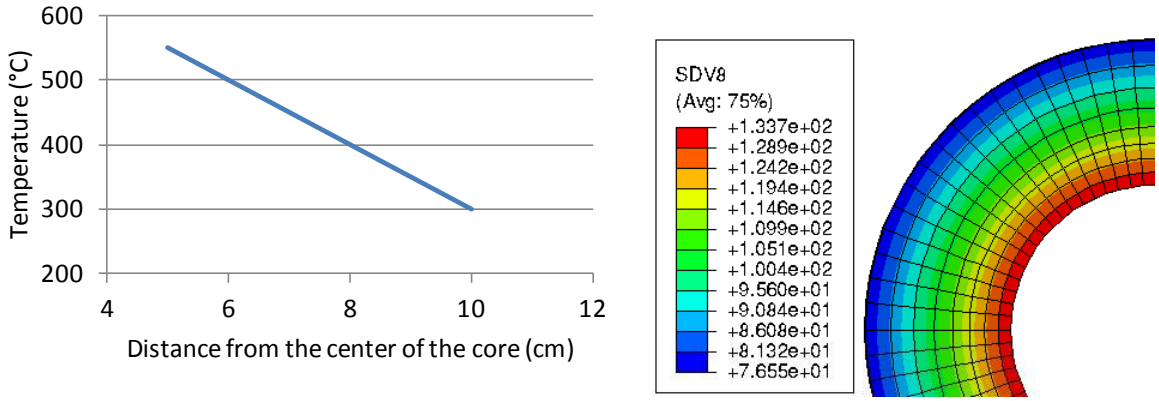

Figure 8.4: Variation of temperature with radial distance from brick center (left); variation of irradiation dose ($x10^{20}n/cm^2$) with radial distance at the end of 20 years (right)

The brick was considered to be made of ATR-2E graphite. The constitutive model for the brick included irradiation creep strain, thermal strain, dimensional change strain and elastic strain. Further details about the constitutive model are provided in [1]. The material data for ATR-2E were obtained from the work conducted by Haag [3]. These included the variations of dimensional change strain, coefficient of thermal expansion and Young's Modulus with dose and temperature. The creep modulus was assumed to be a constant.

To simulate fracture of the brick using XFEM, the maximum principal stress criterion was selected as the damage initiation criterion. The incorporated damage evolution law was based on fracture energy and the linear softening law was used. Thirty different sets of random values of strength (σ_f) and critical stress intensity factor (K_{IC}) were generated based on the Weibull distribution (See Appendix). The mean values and the corresponding Weibull modulus of σ_f and K_{IC} used for generating the random values are given in Table 8.1. The critical fracture energy (G_{IC}) was calculated from the critical stress intensity factor K_{IC} using the Irwin relationship:

$$G = \frac{K^2}{E} \qquad (8.2)$$

where E is the Young's Modulus for virgin graphite.

The variation of strength with irradiation was incorporated in the work presented herein. Data on the dependence of strength on irradiation dose for ATR-2E graphite was not available. Therefore, a trend similar to that found for IG-110 graphite [4] was assumed, as shown in Figure 8.5. An ABAQUS-based user-subroutine, USDFLD, was coded for implementing the irradiation-dependence of strength in the finite element analysis. The variation of fracture toughness with irradiation was not considered.

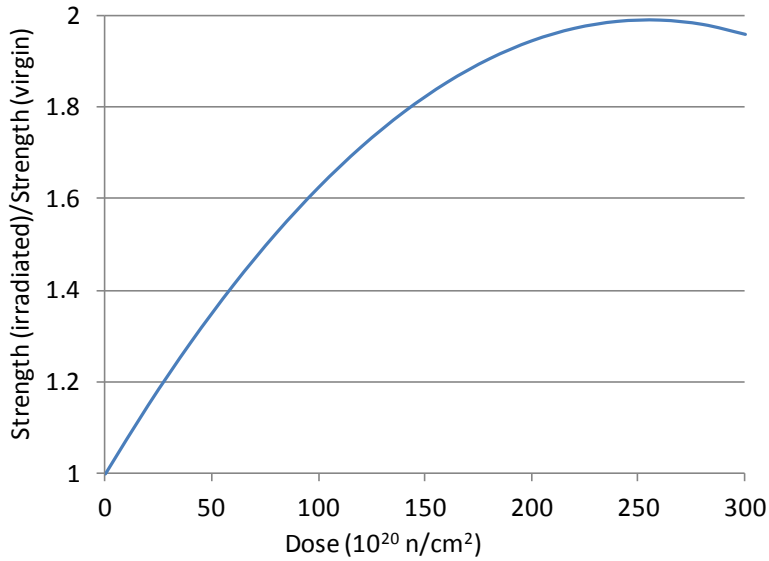

Figure 8.5: Variation of strength with irradiation dose [4]

Table 8.1: The mean value and Weibull Modulus for strength and critical stress intensity factor

	Mean value	**Weibull modulus**
Strength (σ_f)	12.5 MPa	9
Critical stress intensity factor (K_{IC})	1.0 MPa√m	35

Failure of the brick for the thirty cases was simulated and the failure probability of the graphite brick was evaluated as a function of time using Equation 3 below.

$$\text{Failure probability (time t)} = \frac{\text{Number of specimens failed uptil time t}}{\text{Total number of specimens}} \quad (8.3)$$

8.1.2 Results and Discussion

The finite element model was run in ABAQUS for each of the thirty sets of fracture energy and strength. Figure 8.6 shows the maximum principal stress distribution in the graphite brick at the end of 5, 10, 15, 20, 25 and 30 years for Case 1 (σ_f = 13.9 MPa, G_{IC} = 102.5 J/m^2).

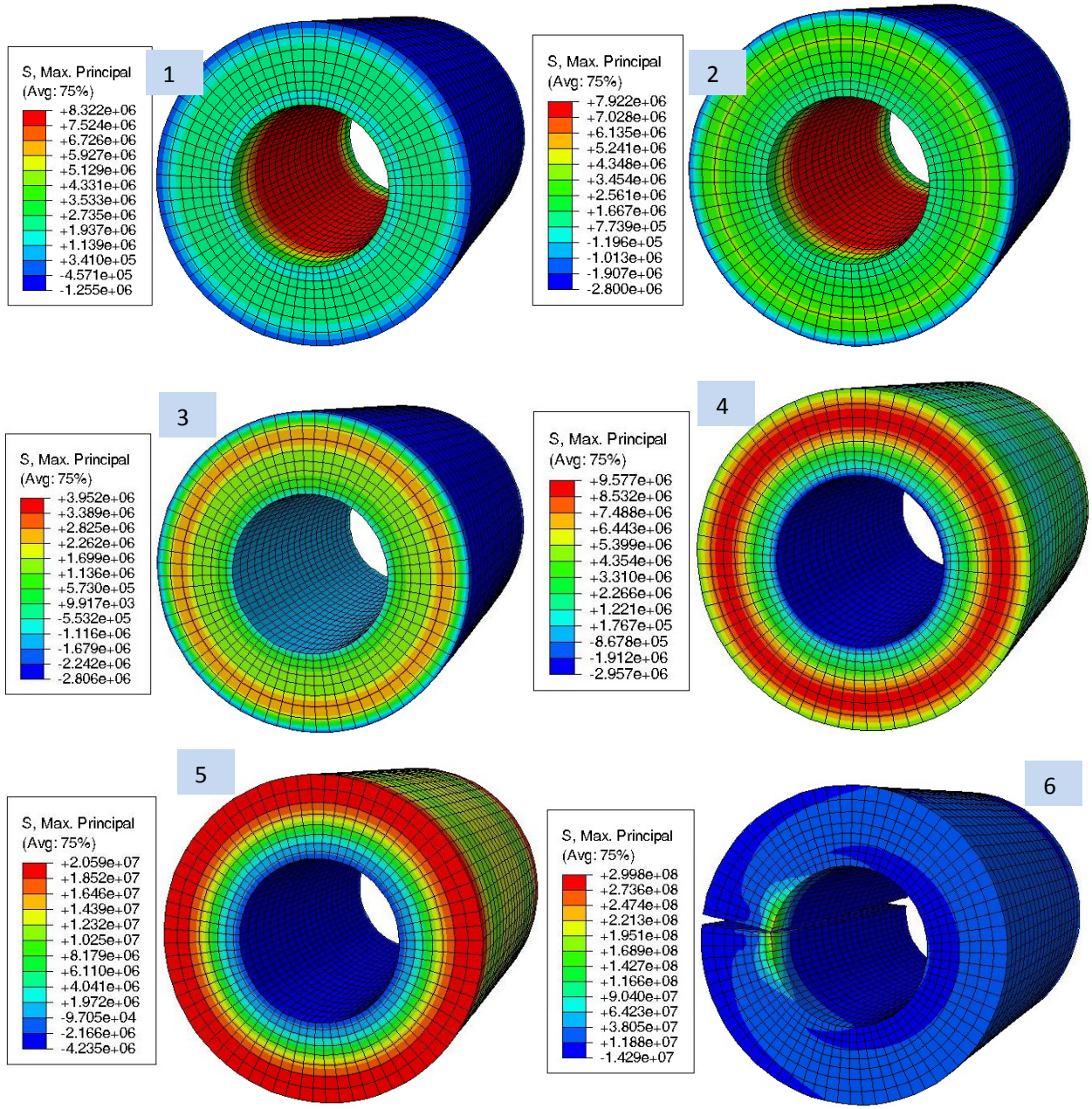

Figure 8.6: Distribution of maximum principal stress at the end of 5, 10, 15, 20, 25 and 30 years, shown in pictures numbered 1, 2, 3, 4, 5 and 6, respectively for Case 1 (σ_f = 13.9 MPa, G_{IC} = 102.5 J/m^2).

Figure 8.7 shows the variation of the hoop stress with time at the inner and outer surfaces of the brick for Case 1. It can be seen that the sudden temperature rise at the start of reactor operation caused the development of thermal stresses in the graphite brick. The thermal stresses are compressive at the inner surface and tensile at the outer surface. Due to irradiation creep and irradiation effects, the thermal stresses are released and at around 2 years the brick was under negligible stress. Then, continued irradiation resulted in tensile stresses in the inner region and compressive stresses in the outer region of the brick. The turn-around of stresses at the inner and outer surfaces took place at the 6th and 9th years,

respectively, and at these time points the magnitude of the stresses started decreasing. At the 12th year, the stresses at the inner surface changed from being tensile to compressive; and at the 17th year the stresses at the outer surface changed from being compressive to tensile and continued to increase until failure.

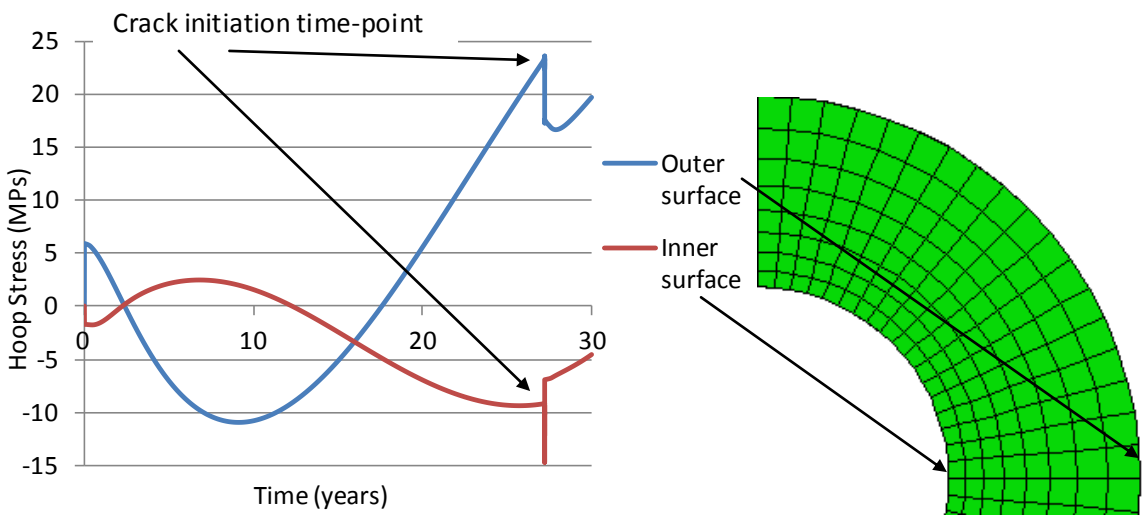

Figure 8.7: Variation of hoop stress with time at the inner and outer surfaces of the brick for Specimen 1 (σ_f = 13.9 MPa, G_{IC} = 102.5 J/m^2).

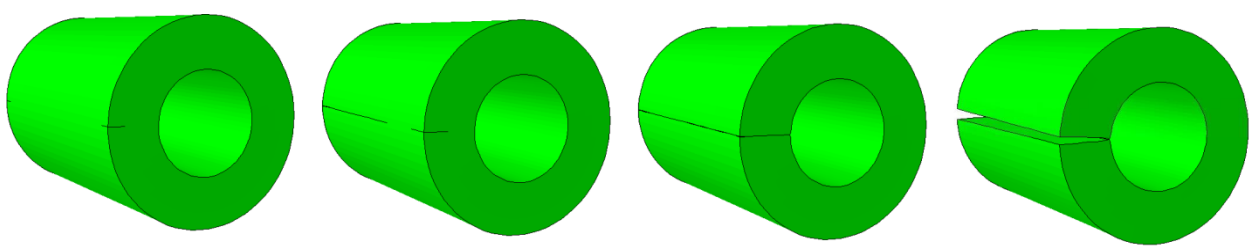

Figure 8.8: Crack propagation with time through a graphite brick model.

Figure 8.8 shows the crack propagation through the thickness of the graphite brick. Since the crack initiation time was found to be very close to the time at which the crack penetrated through more than half of the thickness of the brick, the failure time was taken to be equal to the crack initiation time.

Table 8.2 lists the crack initiation time for all the specimens. It was found that the shortest crack initiation time happened with Specimen 28, which had the lowest strength in the group. The crack in this specimen initiated at the 7th year at the inner surface. After crack initiation, the stresses at the inner surface decreased and turned compressive later on. Thus, the crack was arrested within the small region where it appeared and did not propagate within the first 30 years. For all the other specimens, cracking occurred at the outer surface of the brick and propagated towards the inner surface. Crack initiation at the outer surface can be explained from Figure 8.7, which shows that the maximum principal stress occurs at

the outer surface of the brick, making it most susceptible to fracture. It can be noted from Table 8.2 that the brick specimens with higher strengths had longer lives.

Table 8.2: Fracture toughness, strength and the corresponding crack initiation time for all specimens.

Specimen number	G (J/m^2)	Strength (Pa)	Crack initiation time (years)
1	102.47	13887552.87	27.2
2	112.05	14080373.8	27.3
3	107.68	11881528.27	25.7
4	103.8	10713307.57	24.8
5	97.3	9276372.197	23.8
6	91.779	13531179.51	26.9
7	106.93	11729788.11	25.6
8	114.44	12118053.11	25.8
9	114.19	14748369.47	27.9
10	112.01	12616799.76	26.2
11	99.588	13359223.65	26.8
12	112.07	10618339.73	24.8
13	100.55	12716674.09	26.3
14	112.27	11890412.62	25.7
15	94.808	13341876.42	26.8
16	110.38	11592666.2	25.5
17	113.17	12908567.45	26.4
18	112.13	11364914.11	25.3
19	105.61	11200021.4	25.2
20	108.26	10894350.74	25
21	110.35	12189317.59	25.9
22	99.964	13826740.88	27.1
23	106.21	13050776.05	26.5
24	106.89	9573306.627	24
25	95.701	13409348.67	26.8
26	111.5	10402105.93	24.6
27	102.31	11851814	25.7
28	102.41	6743920.79	6.3
29	109.86	13869423.34	27.2
30	106.55	12218937.04	25.9

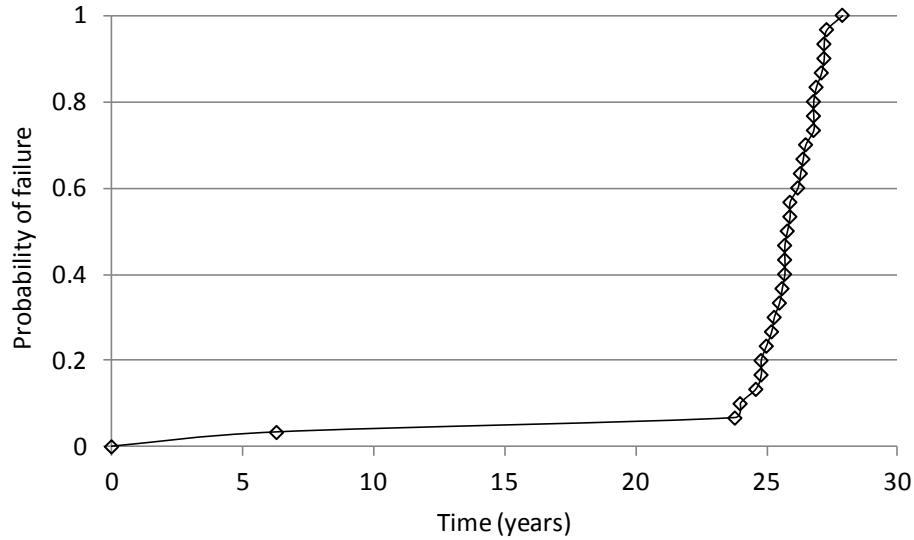

Figure 8.9: Failure probability of ATR-2E graphite brick vs. time

Finally, the failure probability of the ATR-2E graphite brick as a function of time was obtained according to Equation (3), as shown in Figure 8.9. It can be seen that most of the brick specimens failed during the period of 24-27 years and the failure probability was low (0.067) up till 23.8 years and rose steeply thereafter.

These results are in good agreement with the results of 2D failure analysis presented in the 8th quarterly report [5] for the same component. For 2D failure analysis a sudden increment in the temperature was considered which resulted in high thermal stresses leading to failure of two components within the first year. However, for the analysis presented herein the rise in the temperature happened over the period of one day. It lead in smaller thermal stresses and consequently no failure occurred due to thermal stresses.

8.1.3 Summary

Thirty different sets of values of strength and critical fracture energy for ATR-2E graphite were randomly generated based on the Weibull distribution. Linear spatial distributions of dose and temperature in the brick were assumed and the dependence of strength on irradiation dose was considered. For each of the thirty cases, stresses and cracking were simulated for the cylindrical graphite brick. For 29 cases, cracking initiated at the outer surface of the brick and propagated rapidly through the thickness towards the inner surface. Most of the bricks failed between 24 and 27 years. The failure probability of ATR-2E graphite bricks was found to be low up till 23.8 years and rise steeply thereafter. The results for 3D failure analysis presented herein were found to be in good agreement with the results for 2D failure analysis presented in the 8th quarterly report [5] for the same component.

8.2 MONTE CARLO 3D FAILURE ANALYSIS OF A PRISMATIC REFLECTOR BRICK

A Prismatic reactor core ATR-2E graphite brick was modeled using the commercial finite element software ABAQUS. Figure 8.10 shows the location of the brick in the prismatic reactor core and its dimensional details. For simplification the fuel handling hole and the dowel pin holes were not included in the brick model. The brick model is shown in Figure 8.11. The internal stresses caused by temperature and irradiation were predicted using the user-defined subroutine UMAT [1]. The XFEM technique was employed simultaneously with UMAT to simulate crack initiation and propagation which would happen when the internal stresses reached the critical limit.

Monte Carlo failure analysis of the brick was performed by using 30 sets of strength and fracture toughness values (see Appendix) to consider the variations in material properties. These 30 sets of data were generated according to the mean values of strength and fracture toughness and their statistical characteristics of ATR-2E obtained from experiments [3]. The predicted failure time of the 30 samples were then used to evaluate the failure probability of the brick as a function of time.

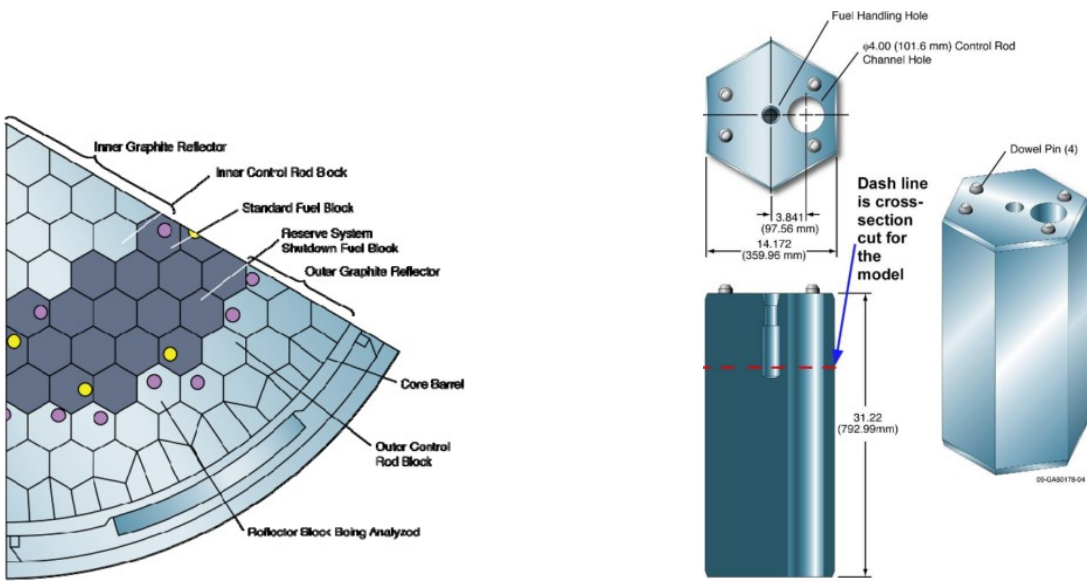

Figure 8.10: Location and dimensional details of prismatic reflector brick considered for failure analysis (source: [6])

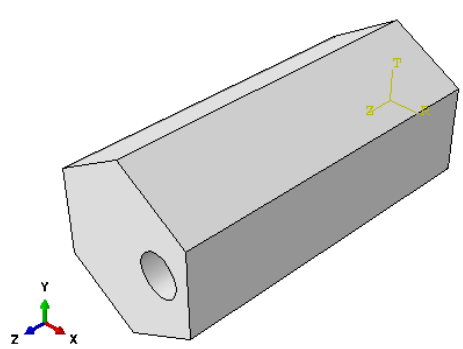

Figure 8.11: A Prismatic reactor core brick model.

8.2.1 FE Simulation

The brick was meshed with 32,224 C3D8 (continuum 3D 8-node linear isoparametric) elements as shown in Figure 8.12. Figure 8.12 also shows the boundary conditions on the model. The irradiation dose distribution was based on the operating conditions for a reflector block in the Ft. St. Vrain reactor as presented in [6]. Due to unavailability of temperature distribution data for the prismatic reflector brick, a temperature distribution based on simple assumptions was used for the numerical analysis (see Figure 8.13).

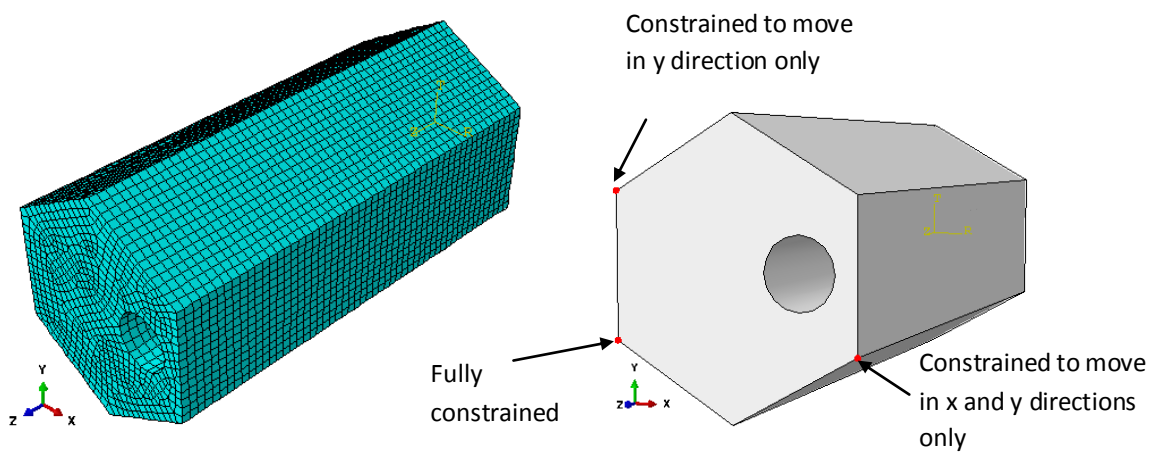

Figure 8.12: Mesh of 3D FE model (left) and boundary conditions on the brick (right).

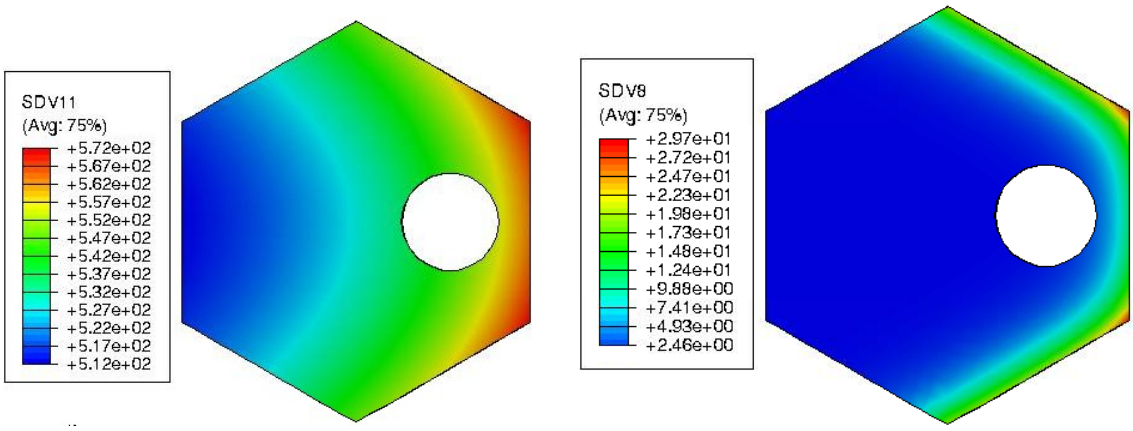

Figure 8.13: Temperature distribution (left) and irradiation dose distribution ($x10^{20}$ n/cm^2) (right) in the prismatic reactor core brick at the end of 6 years.

The brick was considered to be made of ATR-2E graphite. The constitutive model for the brick included irradiation creep strain, thermal strain, dimensional change strain and elastic strain. Further details about the constitutive model are provided in [2]. The material data for ATR-2E were obtained from the work conducted by Haag [3]. These included the variations of dimensional change strain,

coefficient of thermal expansion and Young's Modulus with dose and temperature. The creep modulus was assumed to be a constant.

To simulate fracture of the brick using XFEM, the maximum principal stress criterion was selected as the damage initiation criterion. The incorporated damage evolution law was based on fracture energy and the linear softening law was used. Thirty different sets of random values of strength (σ_f) and critical stress intensity factor (K_{IC}) were generated based on the Weibull distribution (See Appendix). The mean values and the corresponding Weibull modulus of σ_f and K_{IC} used for generating the random values are given in Table 8.3.

Table 8.3: Mean values and the corresponding Weibull modulus of σ_f and K_{IC} used for generating the random values of strength and the critical strength intensity factor.

	Mean value	**Weibull modulus**
Strength (σ_f)	12.5 MPa	9
Critical stress intensity factor (K_{IC})	1.0 MPa√m	35

The critical fracture energy (G_{IC}) was calculated from the critical stress intensity factor K_{IC} using the Irwin relationship given in Equation 8.2.

The variation of strength with irradiation was incorporated in the work presented herein. Data on the dependence of strength on irradiation dose for ATR-2E graphite was not available. Therefore, a trend similar to that found for IG-110 graphite [4] was assumed, as shown in Figure 8.14. An ABAQUS-based user-subroutine, USDFLD, was coded for implementing the irradiation-dependence of strength in the finite element analysis. The variation of fracture toughness with irradiation was not considered.

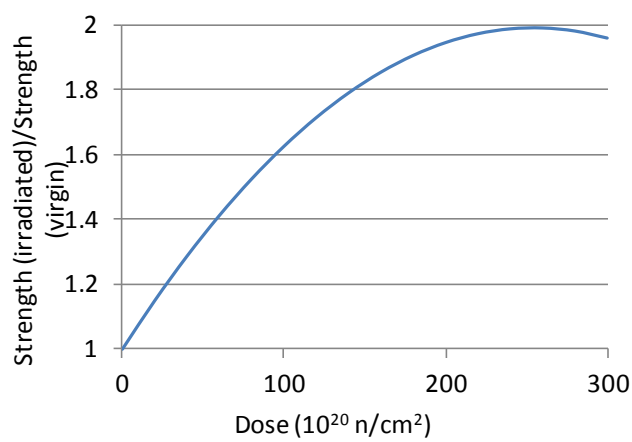

Figure 8.14: Variation of strength with irradiation dose [4]

Failure of the brick for the thirty cases was simulated and the failure probability of the graphite brick was evaluated as a function of time using Equation 8.3.

8.2.2 Results and Discussion

The finite element model was run in ABAQUS for each of the thirty sets of fracture energy and strength. Figure 8.15 shows the maximum principal stress distribution in the graphite brick at the end of 1.5, 3.0, 4.5, 6.0, 7.5 and 9.6 years for Case 7 (σ_f = 11.7 MPa, G_{IC} = 106.93 J/m^2).

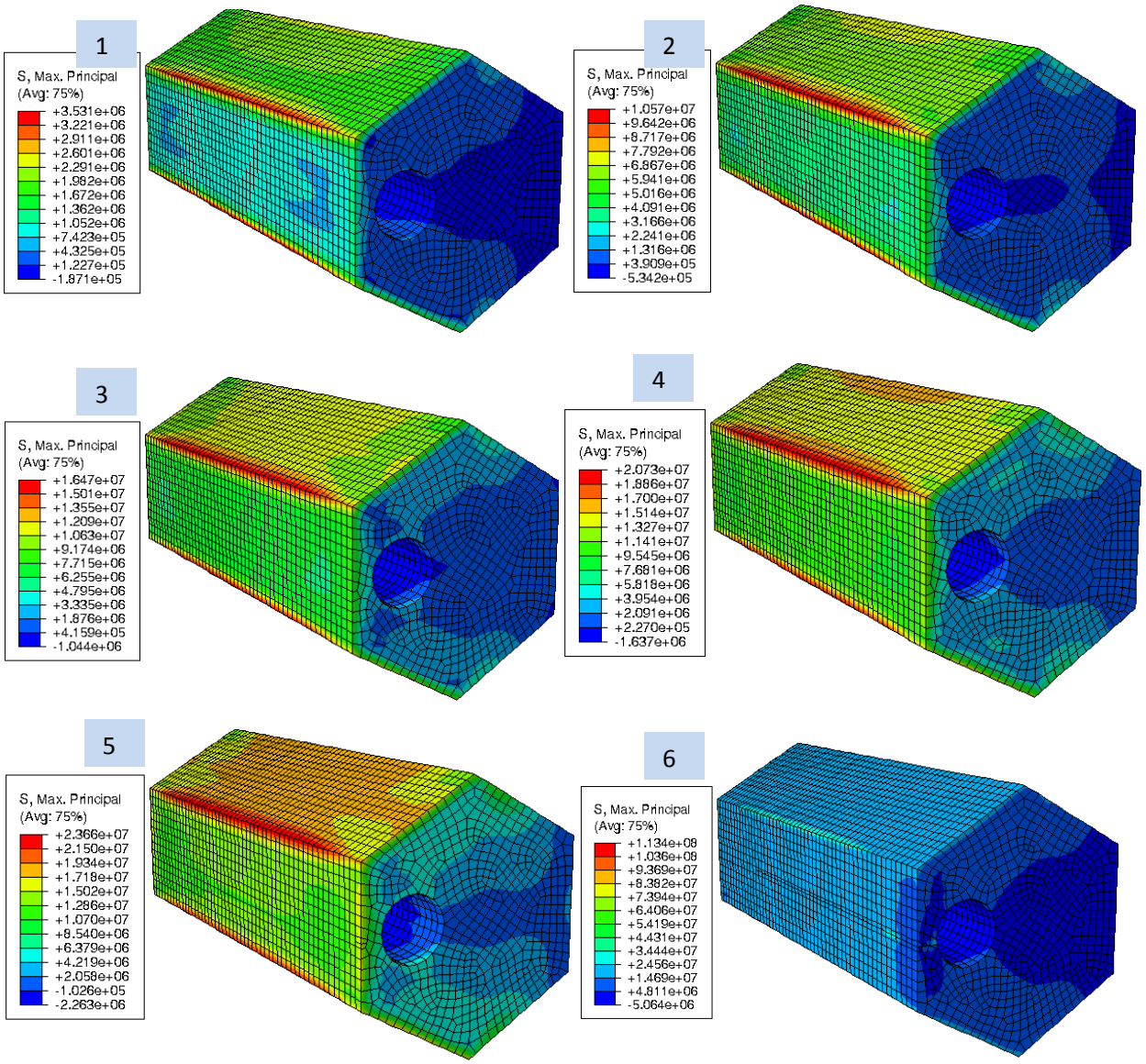

Figure 8.15: Distribution of maximum principal stress at the end of 1.5, 3.0, 4.5, 6.0, 7.5 and 9.6 years, shown in pictures numbered 1, 2, 3, 4, 5 and 6, respectively for Case 7 (σ_f = 11.7 MPa, G_{IC} = 106.93 J/m^2).

Figure 8.16 shows the variation of the maximum principal stress with time at two locations of the brick for Case 7. The maximum principal stress was greater at element A than the stress at element B

during the entire reactor operation time. This difference in the stresses can be attributed to the fact that element A is nearer to the fuel brick and therefore receives greater dose of irradiation than element B. Figure 8.16 also shows some kinks in stress-time curve for element A. These kinks are due to crack initiation and propagation. The stress-time curve for element B does not show such kinks because of the farther location of element B from the crack location.

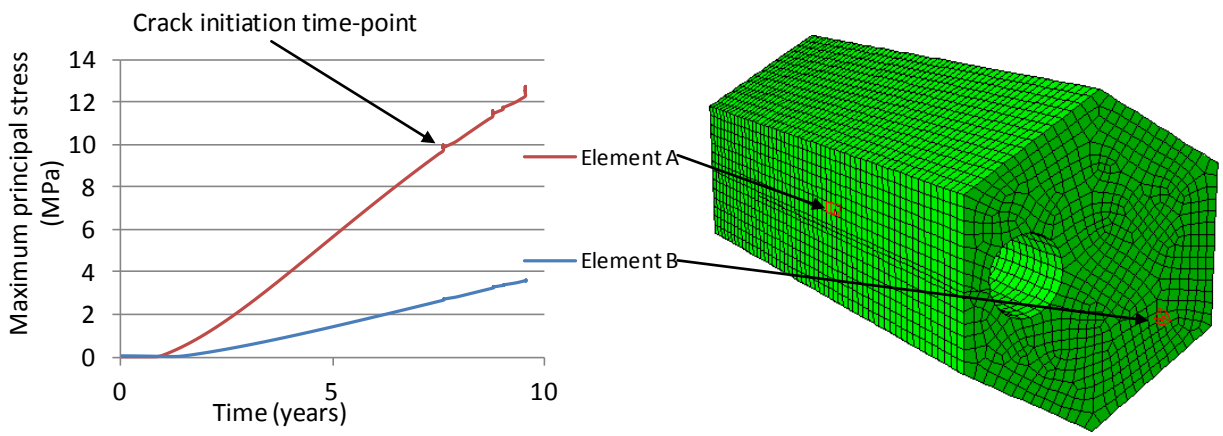

Figure 8.16: Variation of maximum principal stress with time at the inner and outer surfaces of the brick for Specimen 7 (σ_f = 11.7 MPa, G_{IC} = 106.93 J/m^2)

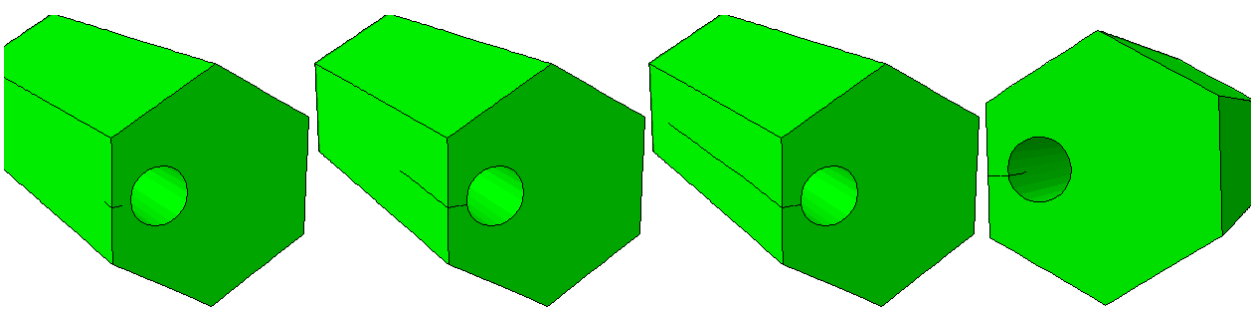

Figure 8.17: Crack propagation with time through a graphite brick model.

Figure 8.17 shows the crack propagation through the length and thickness of the graphite brick. The failure time was taken to be equal to the crack initiation time.

Table 8.3 lists the crack initiation time for all the specimens. It was found that the shortest crack initiation time happened with Specimen 28, which had the lowest strength in the group. The crack in this specimen initiated at the 4th year. For all the specimens cracking occurred at the outer surface. For most of the specimens, crack initiated just ahead of the control rod channel of the brick and propagated along the longitudinal and radially-inward direction as shown in Figure 8.17. Crack initiation at the outer surface can be explained from Figure 8.16, which shows that the maximum principal stress occurs at the outer surface of the brick, making it most susceptible to fracture. In a few specimens, cracking occurred at the outer longitudinal edge of the specimen as shown in Figure 8.18.

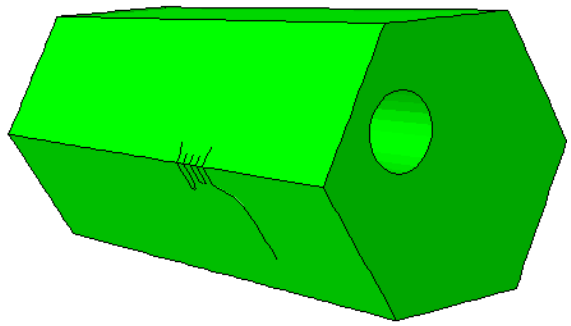

Figure 8.18: Crack on the outer edge of the graphite brick model (Specimen 28).

In the numerical analysis, not only was the variation in strength of the brick specimens incorporated, the strength was also assumed to be dependent on the irradiation dose which was non-uniformly distributed over the brick specimen and also varied with time. Therefore, the different locations of the cracks in some specimens were due to the dissimilar strengths of the specimens. It can be noted from Table 8.3 that the brick specimens with higher unirradiated strengths had longer lives.

Table 8.3: Fracture toughness, strength and the corresponding crack initiation time for all specimens.

Specimen number	G (J/m^2)	Strength (Pa) (un-irradiated)	Crack initiation time (years)
1	102.47	13887552.87	9.4
2	112.05	14080373.8	9.6
3	107.68	11881528.27	7.7
4	103.8	10713307.57	6.7
5	97.3	9276372.197	6.0
6	91.78	13531179.51	9.1
7	106.93	11729788.11	7.5
8	114.44	12118053.11	7.8
9	114.19	14748369.47	10.4
10	112.01	12616799.76	8.2
11	99.59	13359223.65	8.9
12	112.07	10618339.73	6.6
13	100.55	12716674.09	8.4
14	112.27	11890412.62	7.7
15	94.81	13341876.42	8.9
16	110.38	11592666.2	7.5
17	113.17	12908567.45	8.3
18	112.13	11364914.11	7.3
19	105.61	11200021.4	7.2
20	108.26	10894350.74	6.9
21	110.35	12189317.59	8.0
22	99.964	13826740.88	9.4
23	106.21	13050776.05	8.6

24	106.89	9573306.63	5.7
25	95.70	13409348.67	8.9
26	111.5	10402105.93	6.4
27	102.31	11851814	7.7
28	102.41	6743920.79	3.9
29	109.86	13869423.34	9.4
30	106.55	12218937.04	7.9

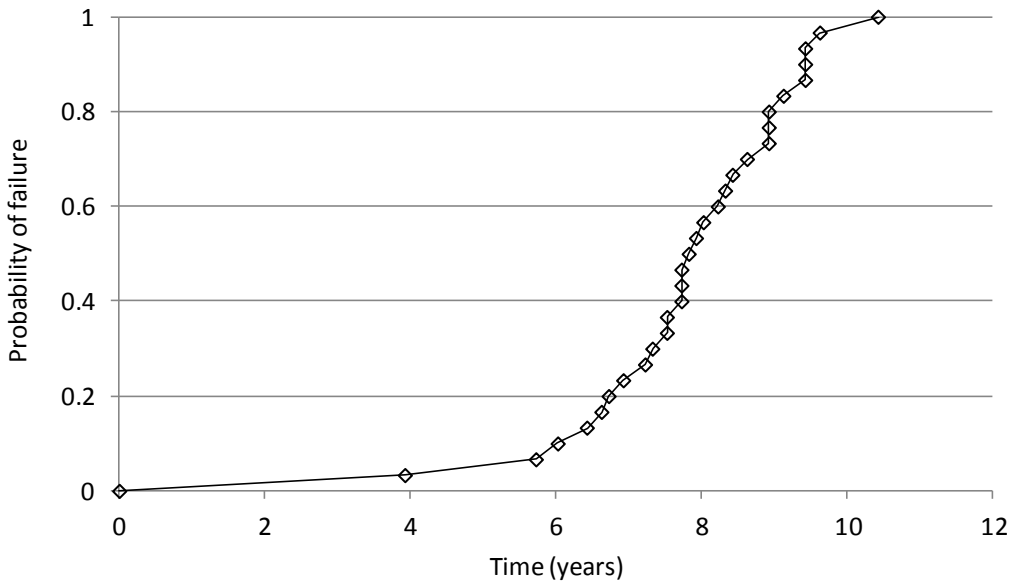

Figure 8.19: Failure probability of ATR-2E graphite brick vs. time

Finally, the failure probability of the ATR-2E graphite brick as a function of time was obtained according to Equation (2.2), as shown in Figure 8.19. It can be seen that most of the brick specimens failed during the period of 6-10 years and the failure probability was low (0.1) up till 6 years and rose steeply thereafter.

8.2.3 Summary

Thirty different sets of values of strength and critical fracture energy for ATR-2E graphite were randomly generated based on the Weibull distribution. Linear spatial distributions of dose and temperature in the brick were assumed and the dependence of strength on irradiation dose was considered. For each of the thirty cases, stresses and cracking were simulated for the Prismatic reactor graphite brick. For most cases, cracking initiated at the outer surface of the brick, near the control rod channel and propagated rapidly along the longitudinal and radially-inward direction of the brick specimen. Most of the bricks failed between 6 and 10 years. The failure probability of ATR-2E graphite bricks was found to be low up till 6 years and rise steeply thereafter.

8.3 REFERENCES

[1] Gyanender Singh, Haiyan Li, Alex Fok. Modeling the Residual Stresses in VHTR Core Components, 10th quarterly report for NEUP-875: Failure Predictions for VHTR Core Components using a Probabilistic Continuum Damage Mechanics Model.

[2] Gyanender Singh, Haiyan Li, Alex Fok. Modeling the Residual Stresses in VHTR Core Components, 4th quarterly report for NEUP-875: Failure Predictions for VHTR Core Components using a Probabilistic Continuum Damage Mechanics Model.

[3] Gerd Haad, Properties of ATR-2E Grpahite and Property Changes Due to Fast Neutron Irradiation, Institute for Safety Research and Reactor Technology.

[4] S. Ishiyama, T.D. Burchell, J.P. Strizak and M. Eto, The Effect of High Fluence Neutron Irradiation on the Properties of a Fine-Grained Isotropic Nuclear Graphite, Journal of Nuclear Materials, 230, 1-7, (1996).

[5] Gyanender Singh, Haiyan Li, Alex Fok. Assessing the Viability of Extended Finite Element Method (XFEM) for Modeling Fracture in Graphite, 8th quarterly report for NEUP-875: Failure Predictions for VHTR Core Components using a Probabilistic Continuum Damage Mechanics Model.

[6] Modeling Mechanical Behavior of a Prismatic Replaceable Reflector Block, Robert L. Bratton, Idaho National Laboratory, Next Generation Nuclear Plant Project, INL/EXT-09-15868, 2009.

9. CHARACTERIZATION OF MECHANICAL PROPERTIES OF COMPOSITE

9.1 GRAPHITE FIBER TEST

9.1.1 Method

In the first part of this task, the mechanical properties of the carbon fibers of a C/C composite were evaluated. The Young's modulus and hardness of individual fibers (as shown in Figure 9.1) were measured through nano-indentation using a MTS nanoindenter XP at the Characterization Facility of the University of Minnesota). The machine worked by driving a diamond indenter into the specimen surface and dynamically collecting the applied force and displacement data.

Several pieces of fiber yarns were randomly selected and mounted into a Teflon ring with an orthodontic resin (DENTSPLY International Inc., US), as shown in Figure 9.2. The surface of the resin block was then polished on a variable speed grinder/polisher (ECOMET 3, Buehler, US), and finished by alumina powder of 1 μm. The finished surface was examined under a microscope to ensure that some fiber cross sections were exposed on the surface, as shown in Figure 9.3.

The finished samples were fixed onto a holder in the nanoindenter, and 15 test points were selected for the nanoindentation test. The Young's modulus and hardness of the fibers were derived from the load vs. displacement curves.

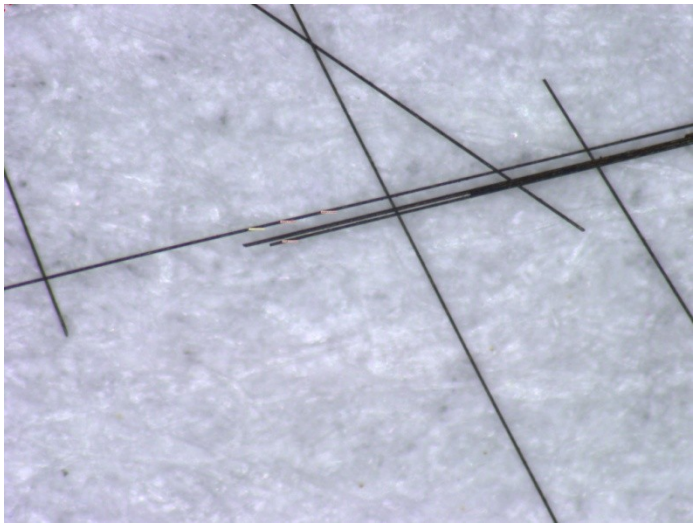

Figure 9.1 Microscopic image of the carbon fibers (with a diameter of around 10 microns)

Figure 9.2 Fibers mounted within acrylic resin (in the area circled in red)

9.1.2 Results and discussion

Except Test 3, for which no data was recorded because of incorrect operation of the machine, 14 valid data sets were recorded. Figure 9.3 shows the recorded load-unload curves for all tests. Figures 9.4 and 9.5 show the changes in Young's modulus and hardness with indenter displacement for each test point, respectively. The results are also listed in Table 9.1, where the average Young's modulus and hardness over a defined displacement range on the loading curves (from 1000nm to 1800nm, being indicated by the two green points) are provided. It also includes the Young's modulus and hardness obtained from the unloading curves.

The mean values and standard deviations, in brackets, for Young's modulus and hardness were 4.388GPa (1.007GPa) and 0.33GPa (0.189GPa), respectively. The hardness obtained from the unloading step was very close to that from the loading step; while the Young's modulus obtained from the unloading step was much smaller than that from the loading step.

The measured Young's modulus of the carbon fibers through nanoindentation was much smaller than the reported value of around 300 GPa. A likely reason could be the much lower Young's modulus or stiffness of the acrylic resin used as the mounting material. Because the fibers were surrounded by a big volume of acrylic resin, the total displacement caused by the compressive force of the indenter included a large amount of elastic or plastic deformation of the acrylic resin.

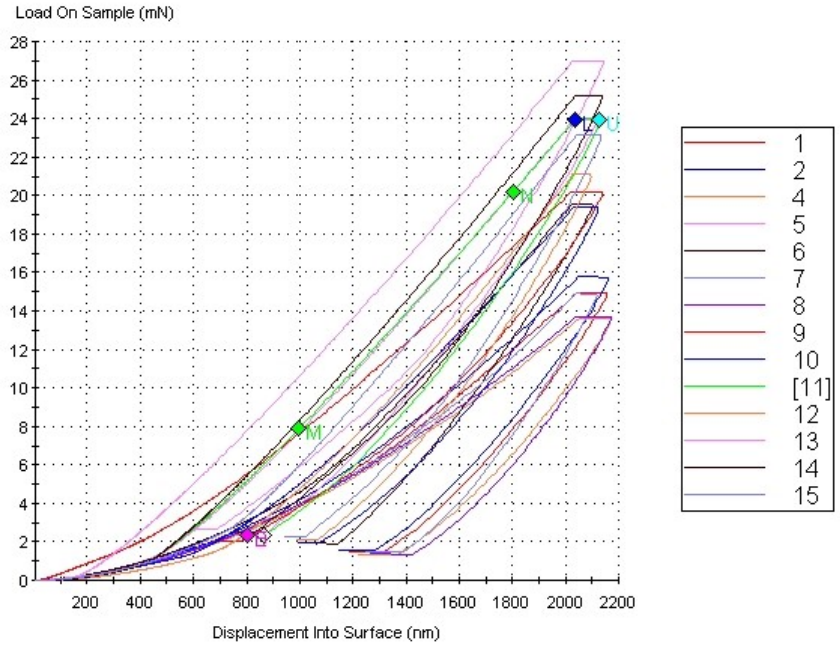

Figure 9.3 Load/unload curves from nanoindentation of carbon fibers mounted in a resin block

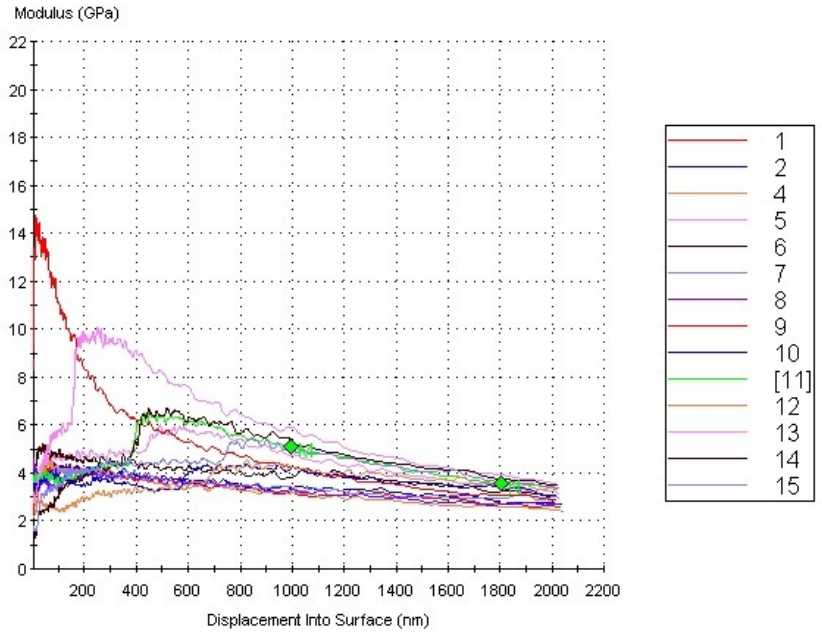

Figure 9.4 Young's modulus of carbon fibers as a function of indenter displacement

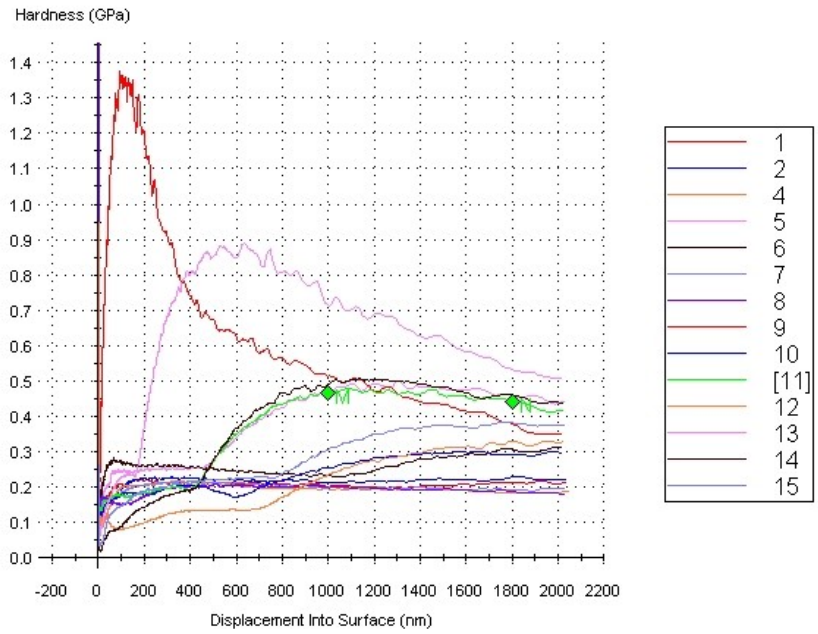

Figure 9.5 Hardness of carbon fibers as a function of indenter displacement

Table 9.1: Young's modulus and hardness of carbon fibers from nanoindentation tests.

Test	E Average Over Defined Range (GPa)	H Average Over Defined Range (GPa)	Modulus From Unload (GPa)	Hardness From Unload (GPa)
1	3.377	0.209	2.078	0.207
2	3.527	0.219	2.119	0.222
3	****	****	0	****
4	3.309	0.199	1.953	0.179
5	5.372	0.411	2.617	0.499
6	4.011	0.239	2.462	0.332
7	3.491	0.206	2.336	0.2
8	3.468	0.203	2.225	0.167
9	4.761	0.571	2.315	0.362
10	4.218	0.213	2.487	0.307
11	4.362	0.465	2.742	0.438
12	4.14	0.173	2.671	0.359
13	6.541	0.822	2.955	0.52
14	5.915	0.438	2.857	0.459
15	4.936	0.249	2.773	0.39
Mean	4.388	0.33	2.471	0.331
Std. Dev.	1.007	0.189	0.311	0.122
% COV	22.95	57.37	12.59	36.71

9.2 EVALUATION OF MECHANICAL PROPERTIES OF COMPOSITES THROUGH FINITE ELEMENT SIMULATION

A finite element (FE) model for a C/C woven composite was developed and employed to predict the mechanical properties of the composite and its internal stresses caused by dimensional change of the carbon fibers resulted from neutron irradiation.

The test material was a piece of C/C woven composite plate (Sigrabond®, SGL Group, Meitingen, Germany). The dimensions of the plate were measured as 50 mm × 44 mm × 2.6 mm. The weaving method of the composite was twill weave. Each weft tow passed over two and then under two warp tows. Similarly, each warp tow passed over and then under two weft tows; see Fig. 1. Each tow (weft or warp) contained 3000 graphite fibers.

(a)

(b) 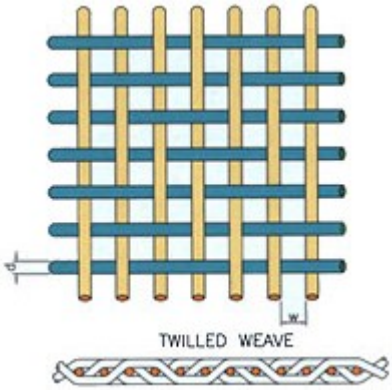

Fig. 9.6: C/C woven composite and its weaving pattern.

9.2.1 Micro-Computed Tomography

In order to model the composite with the FE method, the dimensions and shapes of the weft and warp tows were required. To this end, the composite plate was scanned with a micro-CT scanner. Fig. 9.7 shows CT images of the plate, from which the widths of the weft and warp tows were measured as 1.7mm and 1.4mm, respectively. It can be seen that there was a 0.3mm-wide gap between adjacent warp tows, while the gap between adjacent weft tows was very small and could be ignored. The thickness of each tow could not be identified from the micro-CT images, because the binding material showed very similar grayscale values to the fibers since it was also made of graphite; see Fig 9.7b. The binding material could be seen between tows, but it did not fill the voids completely.

In order to model the composite with FE method, the dimensions and shapes of the weft and warp tows were required. To this end, the composite plate was scanned with a micro-CT scanner. Fig. 9.7 shows the section pictures, from which the widths of weft and warp tows were measured as 1.7mm and

1.4mm, respectively. It can be seen that there was a 0.3mm-wide gap between each two adjacent warp tows, while the gap between each two adjacent weft tows was very small and regarded as 0. The thickness of each tow was not able to be identified from the micro-CT images, because the binding material showed very similar grayscale with the fibers since it is also made of graphite, see Fig 9.7b. Binding material could be seen between tows, but it did not fill all the voids completely.

(a)

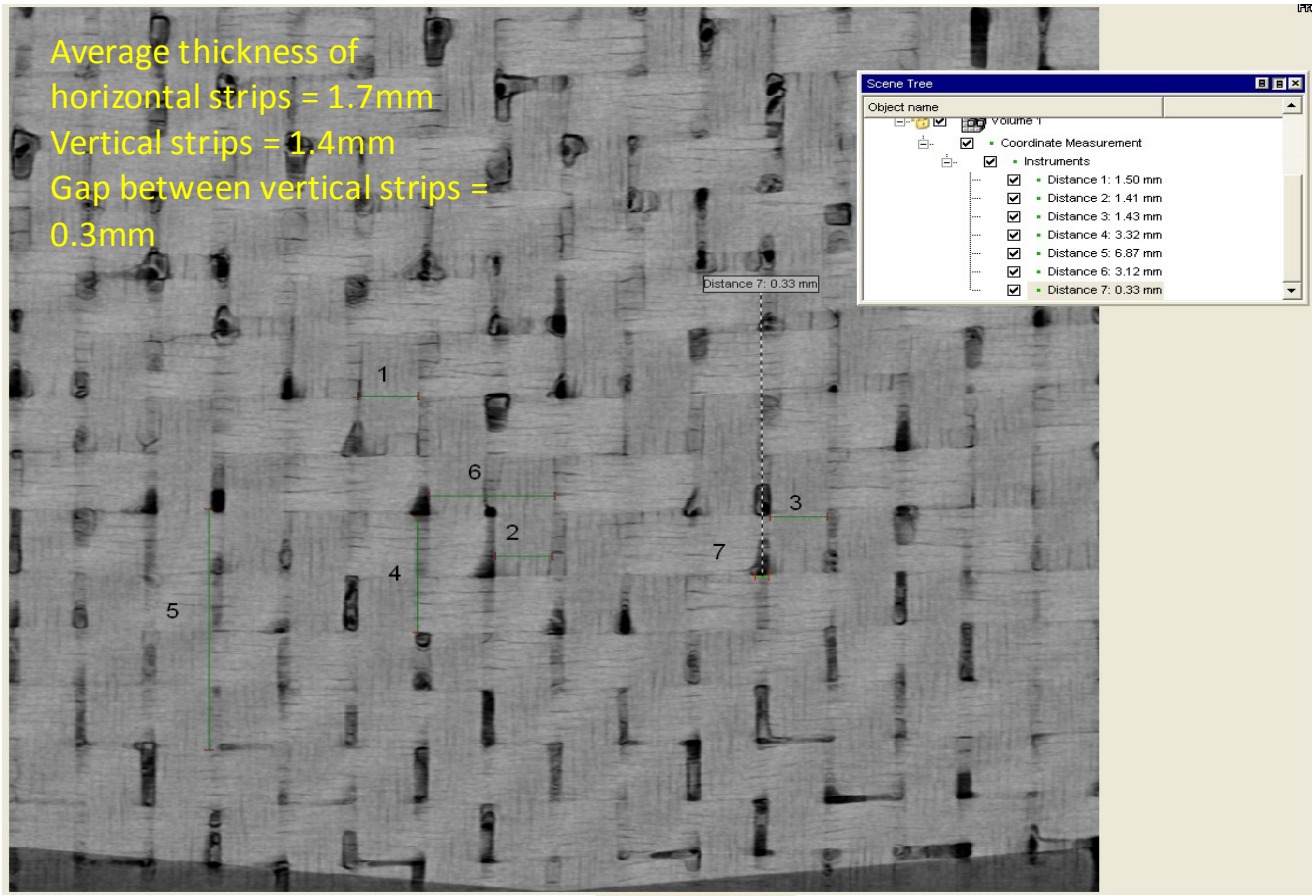

(b)

Fig. 9.7 Plane section (a) and cross section (b) of the composite plate obtained from micro-CT.

The cross section of the composite was then observed under a microscope to measure the thickness and wave pattern of each tow. As shown in Fig. 9.8a, a ruler was placed beside the specimen for calibration. The average wave length of a tow was measured as about 6.8mm, which was four times of the width of a weft tow. The average thickness of a tow was measured as 0.13 mm (Fig. 9.8b), which was also the wave amplitude. In total, the composite plate contained 11 plies.

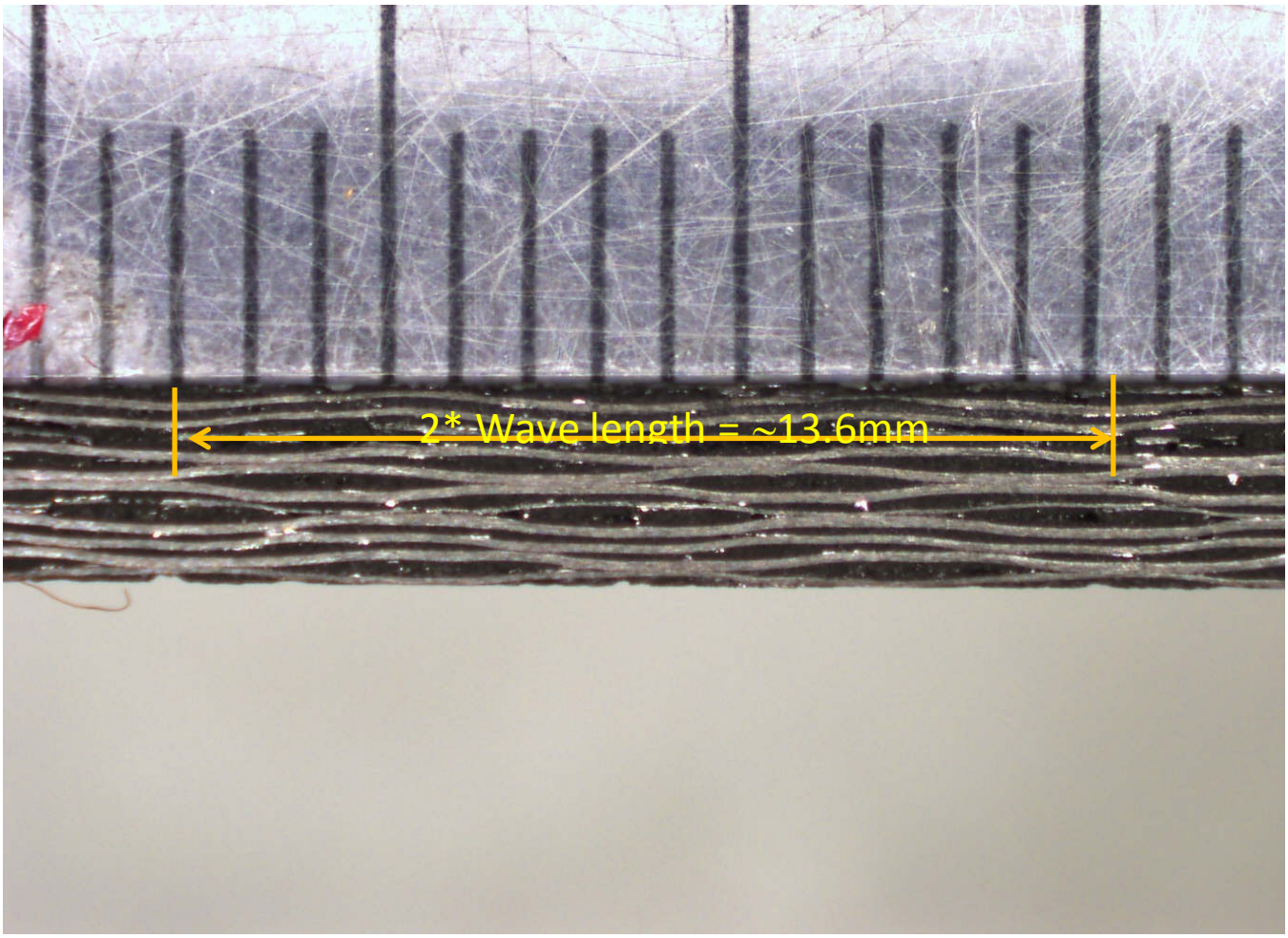

Fig. 9.8a Measurement of the tow thickness and wave pattern under a microscope

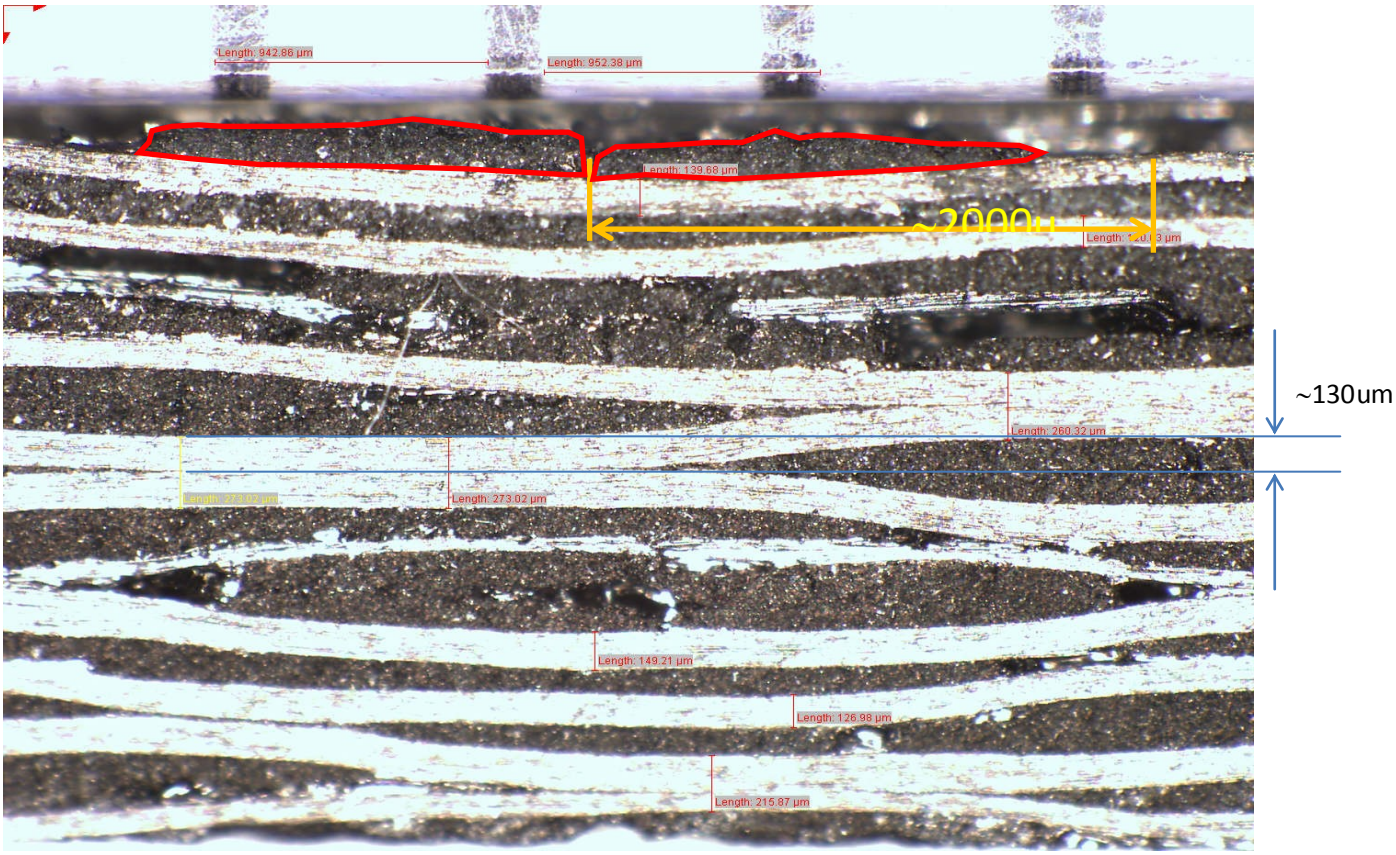

Fig. 9.8b Measurement of the tow thickness and wave shape under microscope

9.2.2 Young's modulus of a single tow

According to the manufacturer, there were 3000 carbon fibers in each tow. Fig. 4a shows a SEM picture of the cross section of the composite plate, from which the cross-sectional area (A_{tow}) of each tow was measured as about 0.163mm^2. A closer view of the cross section (Fig. 4b) showed that the diameter of each fiber was about 6.6µm. Therefore, the volume fraction of fibers (V_{fibers}) in each tow can be calculated with Equation (1) below:

$$V_{\text{fibers}} = \frac{3000 \cdot \pi \cdot r^2}{A_{\text{tow}}} = \frac{3000 \cdot \pi \cdot 3.3^2}{163000} = 0.63 \tag{9.1}$$

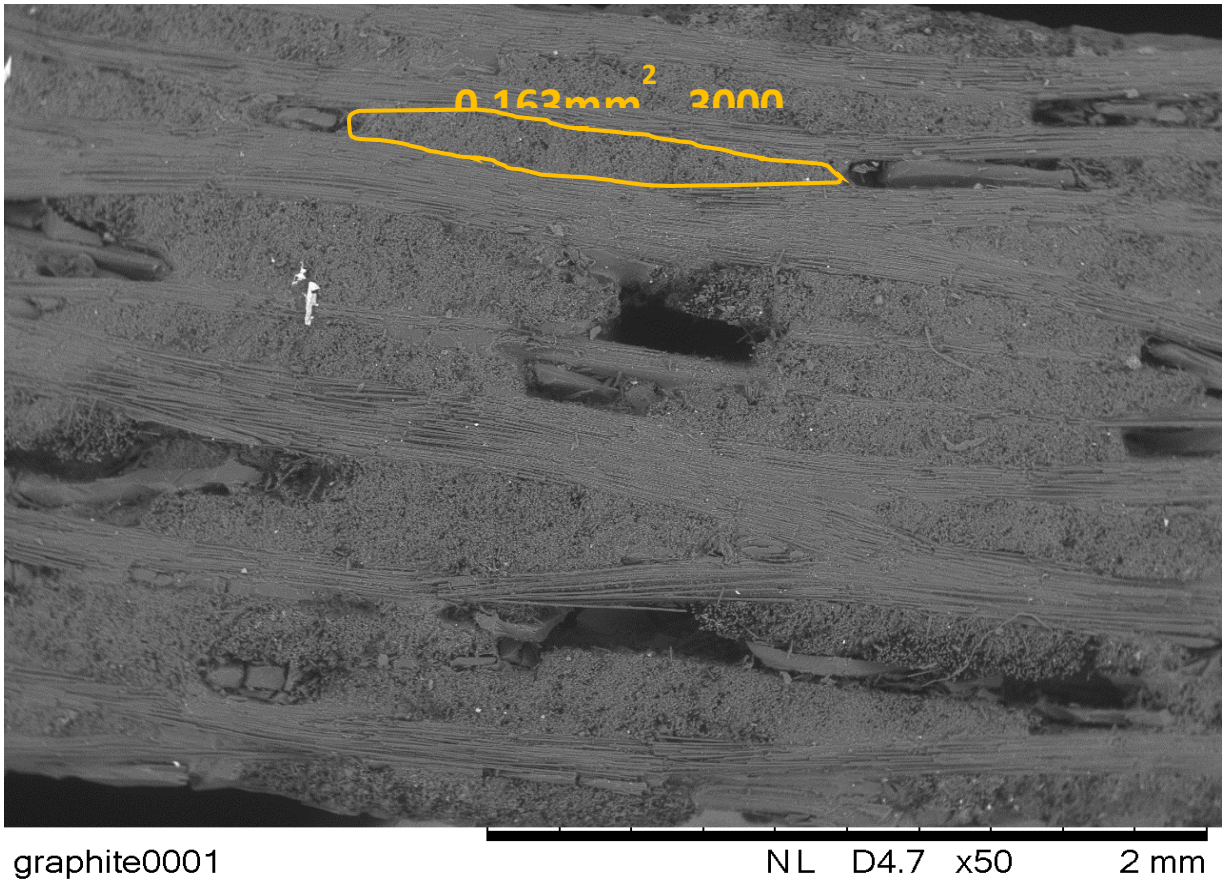

a)

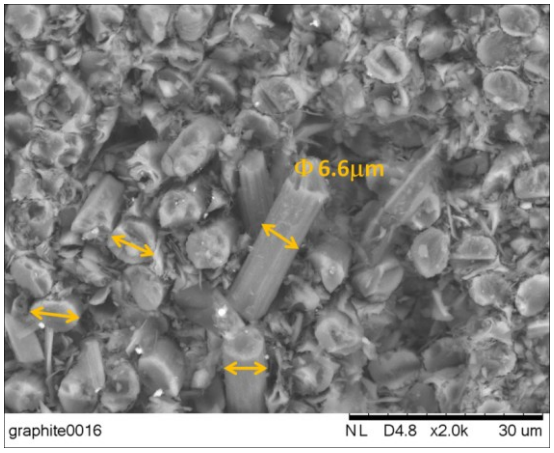

(b)

Fig. 9.9: SEM images of the composite plate, showing the structure of tows (a) and fibers (b)

Each tow can be regarded as a fiber reinforced composite structure, so its material properties are highly anisotropic. The strength and Young's modulus in the direction parallel to the fibers is higher than those in the transverse direction. The Young's modulus in the axial direction (parallel to the fibers) was calculated using the law of mixture:

$$P_C = P_F \cdot V_F + P_M \cdot V_M \tag{9.2}$$

where:

- P represents the property of the material, e.g. Young's modulus;
- V represents the volume fraction of the material;
- C represents the composite material;
- F represents the reinforcement material, e.g. fibers;
- M represents the matrix material, e.g. binder.

It was assumed that the Young's modulus of the binder and fiber were 10GPa [1] and 300GPa [2], respectively. Using the law of mixture, the Young's modulus of a single tow in its axial direction can be calculated as:

$$\begin{aligned} E_{\text{tow,axial}} &= V_{\text{fiber}} \cdot E_{\text{fiber}} + V_{\text{binder}} \cdot E_{\text{binder}} \\ &= 0.63 \cdot 300\text{GPa} + 0.37 \cdot 10\text{GPa} \\ &= 189 + 3.7 \\ &= 192.7\text{GPa} \end{aligned} \tag{9.3}$$

where $E_{\text{tow,axial}}$ is the Young's modulus of the tow in the axial direction, V_{fiber} and V_{binder} are the volumetric fractions of fiber and binder in a tow, respectively; E_{fiber} and E_{binder} are the Young's modulus of fiber and binder, respectively.

In the direction perpendicular to the fibers, the inverse rule of mixtures [3] can be applied, and the Young's modulus was calculated according to Equation (4) below:

$$\frac{1}{E_{\text{tow,transverse}}} = \frac{V_{\text{Fiber}}}{E_{\text{Fiber}}} + \frac{V_{\text{Binder}}}{E_{\text{Binder}}} \tag{9.4}$$

where $E_{\text{tow,transverse}}$ is the transverse Young's modulus of a tow, which was calculated as 15.6 GPa.

9.2.3 Finite element model

A finite element model was built based on a unit cell (4 x 4 tows) of a single ply of the woven composite, as shown in Fig. 9.10. With a small overhang at the end of each tow, the dimensions of the model were 7mm in length, 7mm in width and 0.26mm in thickness. The FE commercial software ABAQUS 6.11 was employed to evaluate the mechanical properties of the ply.

In order to model the curvatures and twists in the tows properly, a pre-analysis was conducted with the following processes: (1) Moving the overlapping tows away from each other in opposite directions at the points of contact, as shown in Fig. 9.11 and (2) stretching the tows back to their initial positions with

contacts among the tows modeled. With this method, the natural curvature and twist of each tow were obtained, as shown in Fig. 9.10.

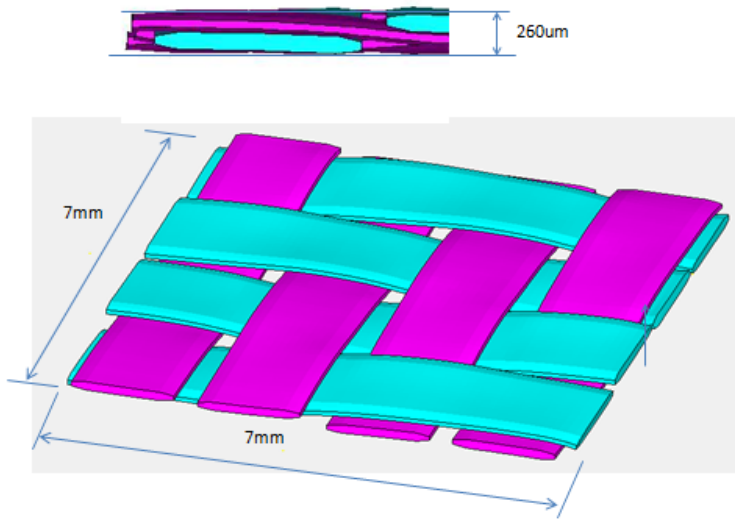

Fig. 9.10: Finite element model of the woven graphite fiber composite

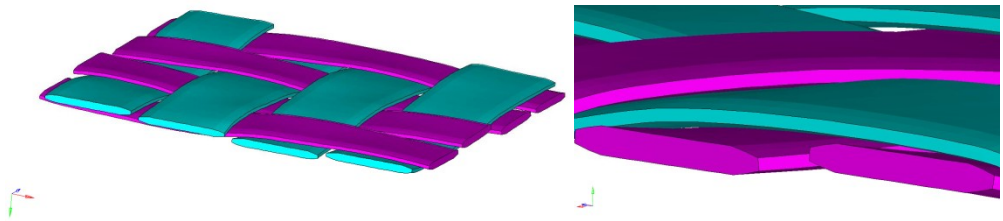

Fig. 9.11: FE model for pre-analyzing to obtain the naturally adapted condition

An orthotropic material constitutive model was used for each tow. Equation (5) gives the stiffness matrix (D) for such a material, where Axis 1 was defined as the direction parallel to the fibers.

$$\begin{Bmatrix} \sigma_{11} \\ \sigma_{22} \\ \sigma_{33} \\ \sigma_{12} \\ \sigma_{13} \\ \sigma_{23} \end{Bmatrix} = \begin{bmatrix} D_{1111} & D_{1122} & D_{1133} & 0 & 0 & 0 \\ & D_{2222} & D_{2233} & 0 & 0 & 0 \\ & & D_{3333} & 0 & 0 & 0 \\ & & & D_{1212} & 0 & 0 \\ & sym & & & D_{1313} & 0 \\ & & & & & D_{2323} \end{bmatrix} \begin{Bmatrix} \varepsilon_{11} \\ \varepsilon_{22} \\ \varepsilon_{33} \\ \gamma_{12} \\ \gamma_{13} \\ \gamma_{23} \end{Bmatrix} = [D^{el}] \begin{Bmatrix} \varepsilon_{11} \\ \varepsilon_{22} \\ \varepsilon_{33} \\ \gamma_{12} \\ \gamma_{13} \\ \gamma_{23} \end{Bmatrix}$$

For an orthotropic material the engineering constants define the **D** matrix as

$$\begin{aligned}
D_{1111} &= E_1(1-\nu_{23}\nu_{32})\Upsilon, \\
D_{2222} &= E_2(1-\nu_{13}\nu_{31})\Upsilon, \\
D_{3333} &= E_3(1-\nu_{12}\nu_{21})\Upsilon, \\
D_{1122} &= E_1(\nu_{21}+\nu_{31}\nu_{23})\Upsilon = E_2(\nu_{12}+\nu_{32}\nu_{13})\Upsilon, \\
D_{1133} &= E_1(\nu_{31}+\nu_{21}\nu_{32})\Upsilon = E_3(\nu_{13}+\nu_{12}\nu_{23})\Upsilon, \\
D_{2233} &= E_2(\nu_{32}+\nu_{12}\nu_{31})\Upsilon = E_3(\nu_{23}+\nu_{21}\nu_{13})\Upsilon, \\
D_{1212} &= G_{12}, \\
D_{1313} &= G_{13}, \\
D_{2323} &= G_{23},
\end{aligned}$$

where

$$\Upsilon = \frac{1}{1-\nu_{12}\nu_{21}-\nu_{23}\nu_{32}-\nu_{31}\nu_{13}-2\nu_{21}\nu_{32}\nu_{13}}. \tag{9.5}$$

The following Poisson's ratios were assumed:

$$\nu_{12} = \nu_{13} = 0.2; \nu_{23} = \nu_{32} = 0.2$$

Other Poisson's ratios are not independent properties and they were calculated as follows:

$$\frac{\nu_{ij}}{E_i} = \frac{\nu_{ji}}{E_j} \tag{9.6}$$

Thus the following Poisson's ratios were obtained:

$$\nu_{21} = \nu_{31} = 0.01625$$

and the constants in matrix D were determined as:

$$\begin{aligned}
&\mathbf{D}_{1111} = 194.3; \mathbf{D}_{2222} = 16.33; \mathbf{D}_{3333} = 15.55 \\
&\mathbf{D}_{1122} = 3.94; \mathbf{D}_{1133} = 3.94; \mathbf{D}_{2233} = 3.32 \\
&\mathbf{D}_{1212} = 6.5; \mathbf{D}_{1313} = 6.5; \mathbf{D}_{2323} = 6.5
\end{aligned} \tag{9.7}$$

9.2.4 Prediction of Young's modulus

Based on the predicted Young's moduli for a single tow in Section 9.2.2 and the stiffness matrix in Section 9.2.3, the FE model in Fig. 9.10 was used to predict the bulk Young's modulus of a composite ply.

As shown in Fig. 9.12, the boundary conditions applied included: (1) Along Edges A and B, the four cyan warp tows were constrained in the vertical (normal to the ply plane) direction. Coupling

constraints in the axial direction was also defined to ensure that they would have the same elongation and their end surfaces would remain in the same plane. (2) Along edge C, the four pink weft tows were constrained in the vertical and axial directions; and (3) along edge D, the four pink weft tows were constrained in the vertical direction and their movements in the axial direction were coupled.

A 100N tensile force was applied on Edge D.

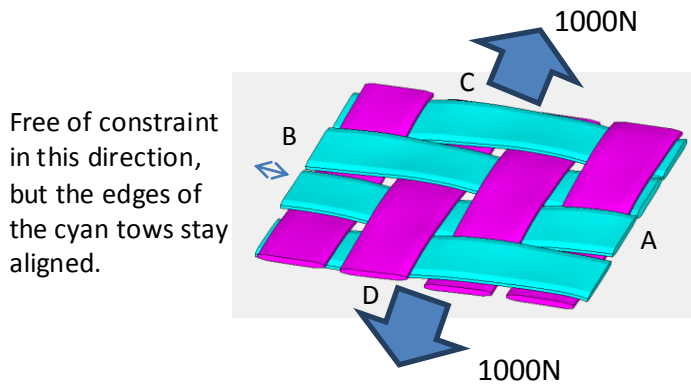

Fig. 9.12: Loads and boundary conditions in the FE model for calculating the Young's modulus of a composite ply

The load and elongation of the four pink tows were recorded at each increment of the analysis. Fig. 9.13 plots the equivalent stress in terms of the equivalent strain. Regression analysis of those points gave the equivalent Young's modulus of a single ply of the composite E_{ply} = 63.59 GPa. This value was very close to the flexural modulus of 60-70GPa provided by the manufacturer [4].

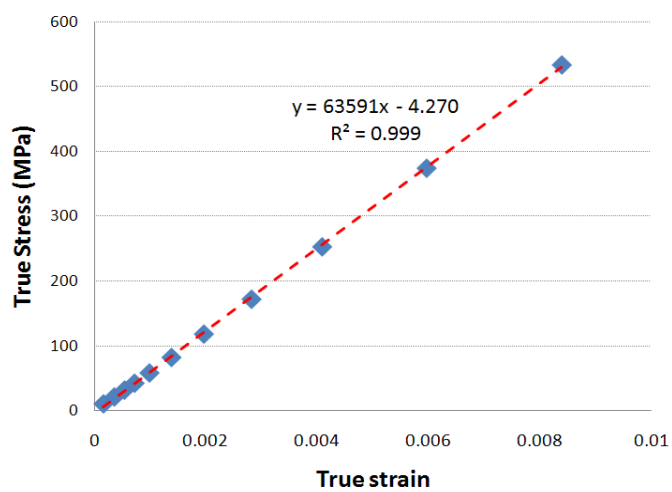

Fig. 9.13: Equivalent stress-strain curve for a single ply of composite under tension

9.3 Prediction of Residual Stresses Within the Composite Caused by Shrinkage of Graphite Fibers

Neutron irradiation can induce dimensional changes in the carbon fibers – they will shrink in the axial direction and expand in the transverse direction. The internal stresses within the composite caused by the dimensional changes in the fibers were simulated with the same FE model. Due to the lack of data on the dimensional changes of carbon fibers, an estimation of 1% shrinkage in the axial direction and 1% expansion in the transverse direction was made for the FE analysis.

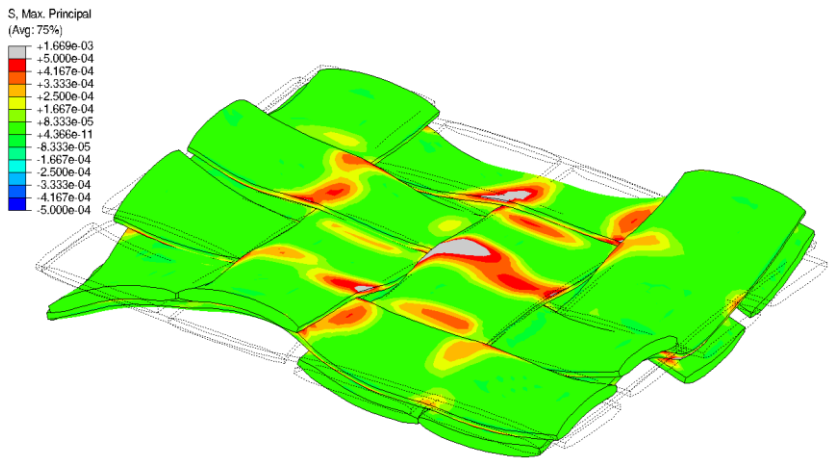

Fig.9.14 Maximum principal stress (x10^{12} Pa) in the composite ply due to dimensional changes in the carbon fibers (Deformation was scaled up by 5 times).

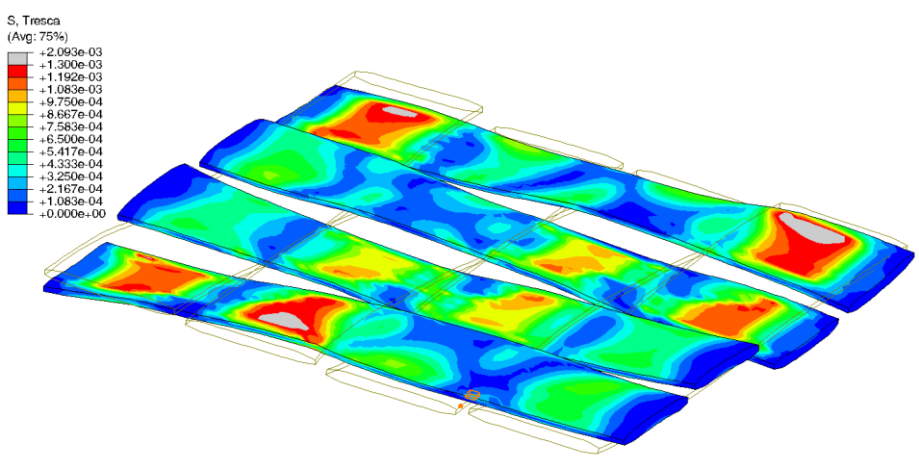

Fig. 9.15 Tresca stress (maximum shear stress) (x10^{12} Pa) in the bonding areas between the weft and warp tows (The warp tows were outlined only).

Fig. 9.14 shows the maximum principal stress distribution within the composite ply. It can be seen that the local maximum principal stress can reach up to 1.7 GPa due to severe bending of the tows. The binding material was subjected to shear stress due to relative sliding movements of the tows, and the maximum shear stress (Tresca stress) can be up to 2.093 GPa, as shown in Fig. 9.15.

According to the manufacture's document [4], the flexural and tensile strengths for the composite are 140-180 MPa and 300-350 MPa, respectively. The tensile strength for a single fiber was measured as 1.8 GPa [5]. There is no data available on the shear strength of the binder. The predicted residual stresses caused by the dimensional changes of the fibers could undermine the integrity of the composite structure.

9.4 REFERENCES

1) Joyce MR, Marrow TJ, Mummery P, Marsden BJ. Observation of microstructure deformation and damage in nuclear graphite. Engineering Fracture Mechanics 2008;75:3633-3645.
2) Minus M, Kumar S. The processing, properties, and structure of carbon fibers. JOM 2005;57:52-58.
3) E S. The transverse elastic modulus of fiber-reinforced composites as defined by the concept of interphase. Journal of Applied Polymer Science 1993; 48:13
4) SGL Group TCC. Carbon Fiber-Reinforced Carbon and Graphite: High-Temperature Applications. Brochure 2008.
5) Haiyan Li, Gyanender Singh and Alex Fok. Measurement of Tensile Strength and Young's Modulus of Graphite Fibers, 7th quarterly report for NEUP-875: Failure Predictions for VHTR Core Components using a Probabilistic Continuum Damage Mechanics Model.

10. EXTENSION OF UMAT FOR COMPOSITES

A user-defined subroutine UMAT was developed for predicting the mechanical behavior of an orthotropic composite structure under irradiation. The UMAT was verified by modeling the mechanical behavior of a plate under a) pure mechanical loading and b) irradiation. The numerical solution was compared with the analytical solution for each case.

10.1 VERIFICATION OF UMAT FOR COMPOSITE

10.1.1 Constitutive Relationship for a Composite Material

The constitutive relationship for an orthotropic composite material under the conditions of plane stress is given as:

$$\begin{bmatrix} \sigma_x \\ \sigma_y \\ \sigma_{xy} \end{bmatrix} = \begin{bmatrix} K_{11} & K_{12} & 0 \\ K_{12} & K_{22} & 0 \\ 0 & 0 & K_{33} \end{bmatrix} \begin{bmatrix} \varepsilon_x \\ \varepsilon_y \\ \gamma_{xy} \end{bmatrix} \qquad (10.1)$$

where

$$K_{11} = \frac{E_x}{1 - \nu_{xy}\nu_{yx}}$$

$$K_{12} = \frac{\nu_{xy}E_y}{1 - \nu_{xy}\nu_{yx}} = \frac{\nu_{yx}E_x}{1 - \nu_{xy}\nu_{yx}}$$

$$K_{22} = \frac{E_y}{1 - \nu_{xy}\nu_{yx}}$$

$$K_{33} = G_{xy}.$$

In the above relations E_x and E_y are the Young's moduli in the x and y directions respectively; ν_{xy} and ν_{yx} are the Poisson's ratios; G_{xy} is the modulus of rigidity. The UMAT was verified by using it to model the mechanical behavior of a plate under irradiation using UMAT and comparing the numerical solution with the corresponding analytical solution.

The elastic moduli of the composite material were assumed to be dependent upon irradiation as shown in Figure 10.1. The Poisson's ratios, however, were assumed to be constant ($\nu_{xy} = 0.4$, $\nu_{yx} = 0.2$).

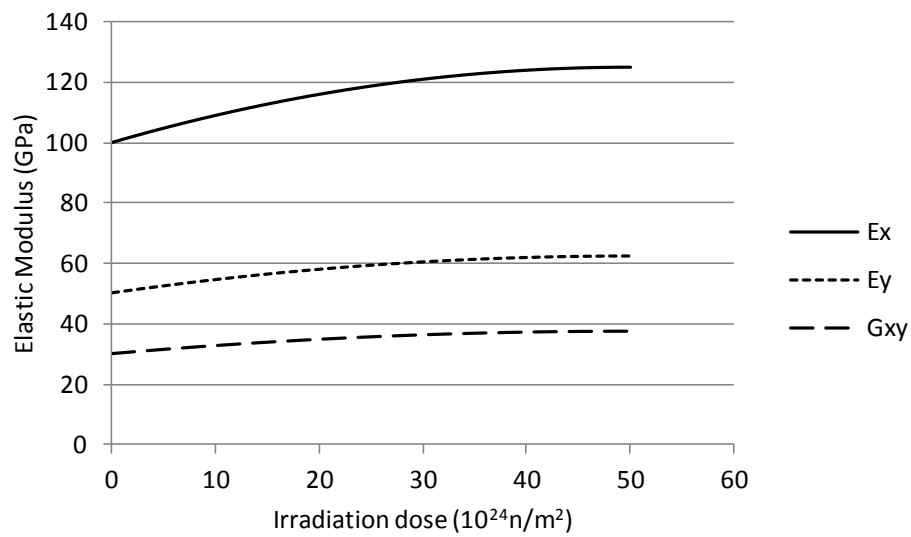

Figure 10.1: Assumed variation of the elastic properties of orthotropic composite material subjected to irradiation.

10.1.2 Verification of UMAT

10.1.2.1 Problem Set-Up

A thin composite plate under the conditions of plane stress was considered. The composite plate was constrained at all the edges as shown in Figure 10.2 and was subjected to irradiation. The irradiation dose was assumed to be uniformly distributed over the plate. Also, the irradiation dose (γ) was assumed to increase linearly with time (t) as given in Equation 10.2 below.

$$\gamma = 50t \qquad (10.2)$$

where t is in years and γ is measured in $10^{24}n/m^2$. The creep strains were ignored to simplify the problem, thus, making it possible to obtain the analytical solution. The assumed variation of the dimensional change strain with irradiation dose was based on [3] and is shown in Figure 10.3. The plate was assumed to be at a constant temperature but the dependence of the coefficient of thermal expansion on the irradiation dose [3] was incorporated in the analysis. Figure 10.4 shows the assumed variation of the coefficient of thermal expansion with the irradiation dose.

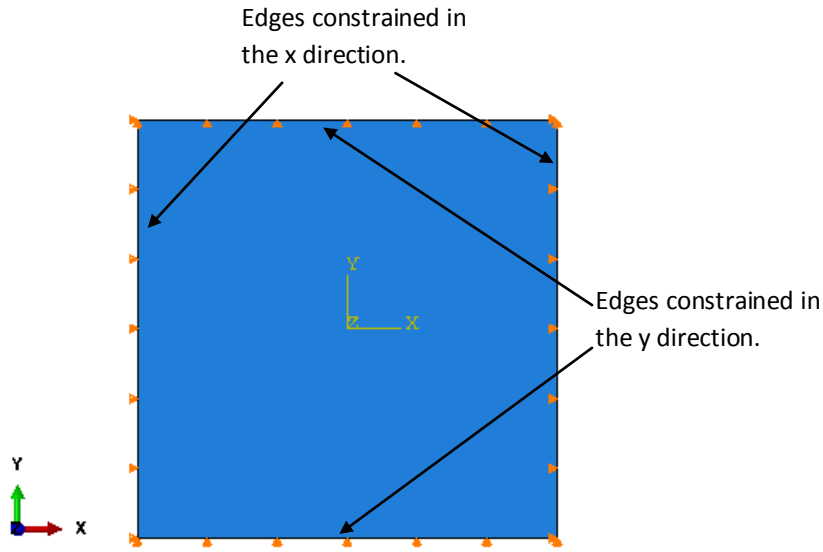

Figure 10.2: Boundary conditions on the composite plate.

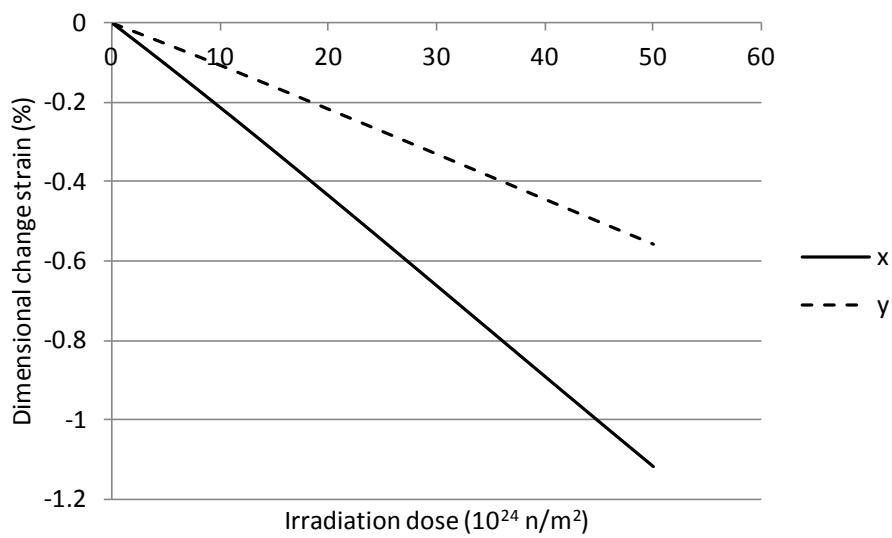

Figure 10.3: Assumed variation of the dimensional change strain with irradiation dose in the x and y directions for the composite (based on [3]).

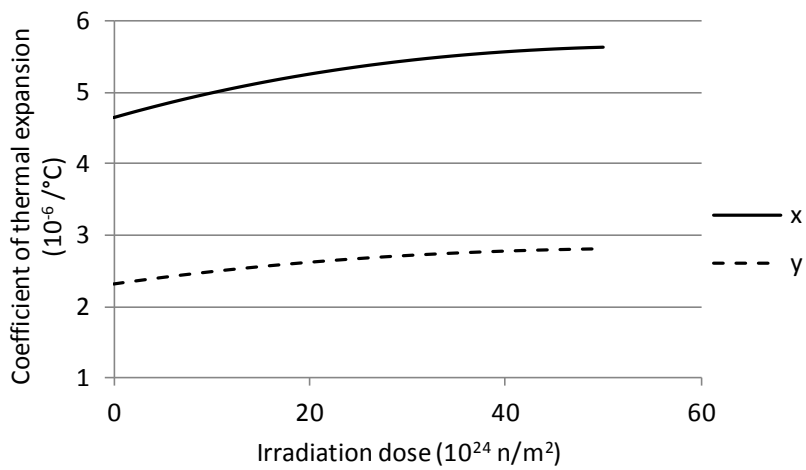

Figure 10.4: Assumed variation of the coefficient of thermal expansion with irradiation dose in the x and y directions for the composite material (based on [3]).

10.1.2.2 Comparison of Numerical and Analytical Solution

The model was analyzed in ABAQUS using the UMAT and the stresses were evaluated at the end of one year. The problem was also solved analytically. The total strain was composed of the elastic strain (ε^e), the dimensional change strain (ε^{dc}) and the thermal strain (ε^{th}). The incremental elastic strain can be written as shown in equations 10.3 and 10.4.

$$d\varepsilon_x^{total} = d\varepsilon_x^e + d\varepsilon_x^{dc} + d\varepsilon_x^{th} \qquad (10.3)$$

$$d\varepsilon_y^{total} = d\varepsilon_y^e + d\varepsilon_y^{dc} + d\varepsilon_y^{th} \qquad (10.4)$$

The plate was constrained on all four sides. Therefore, $\varepsilon^{total} = 0$ in both the x and y directions. Since dimensional change strain (ε_x^{dc} and ε_y^{dc}) and the thermal strain (ε_x^{th} and ε_y^{th}) are known functions of irradiation dose (γ) (see Appendix for details), the elastic strain (ε_x^e and ε_y^e) can be obtained using equations 10.3 and 10.4 as a function of irradiation dose. The incremental elastic strains (ε_x^e and ε_y^e) can be written as:

$$d\varepsilon_x^e = d\varepsilon_x^e\,(\gamma) \qquad (10.5)$$

$$d\varepsilon_y^e = d\varepsilon_y^e\,(\gamma) \qquad (10.6)$$

Using equations 10.1 to 10.6 we obtain Equation 10.7.

$$\begin{bmatrix} d\sigma_x \\ d\sigma_y \\ d\sigma_{xy} \end{bmatrix} = \begin{bmatrix} K_{11}(\gamma) & K_{12}(\gamma) & 0 \\ K_{12}(\gamma) & K_{22}(\gamma) & 0 \\ 0 & 0 & K_{33} \end{bmatrix} \begin{bmatrix} d\varepsilon_x^e(\gamma) \\ d\varepsilon_y^e(\gamma) \\ 0 \end{bmatrix} \qquad (10.7)$$

Equation 10.7 was solved by integration and the stresses were calculated at the end of one year. Table 10.1 shows a comparison between the numerical and the analytical solution. The analytical solution was found to be in good agreement with the numerical solution.

Table 10.1: Comparison of numerically and analytically evaluated stresses for the composite plate.

	Numerical Solution (x 10^8 Pa)	Analytical Solution (x 10^8 Pa)	Error (%)
σ_x	15.23	15.23	0
σ_y	6.23	6.23	0
σ_{xy}	0	0	0

10.1.3 Summary

A user-defined subroutine UMAT was developed for predicting the mechanical behavior of a reactor component made of composite material. The UMAT was verified by comparing the predictions about the mechanical behavior of a composite plate under two different types of loading (pure mechanical loading and exposure to irradiation) with the predictions based on the analytical solution. For both cases, the numerical solution was found to be in good agreement with the analytical solution.

10.2 Stress Analysis of a Composite Control Rod

10.2.1 Methods

A control rod was modeled using the commercial finite element software ABAQUS. Figure 10.1 shows the location of the brick in the prismatic reactor core which contains the control rod under consideration. The control rod was assumed to be made of orthotropic SiC-SiC composite reinforced with Hi-Nicalon Type-S fibers [1]. Figure 10.2 shows a schematic diagram of the control rod.

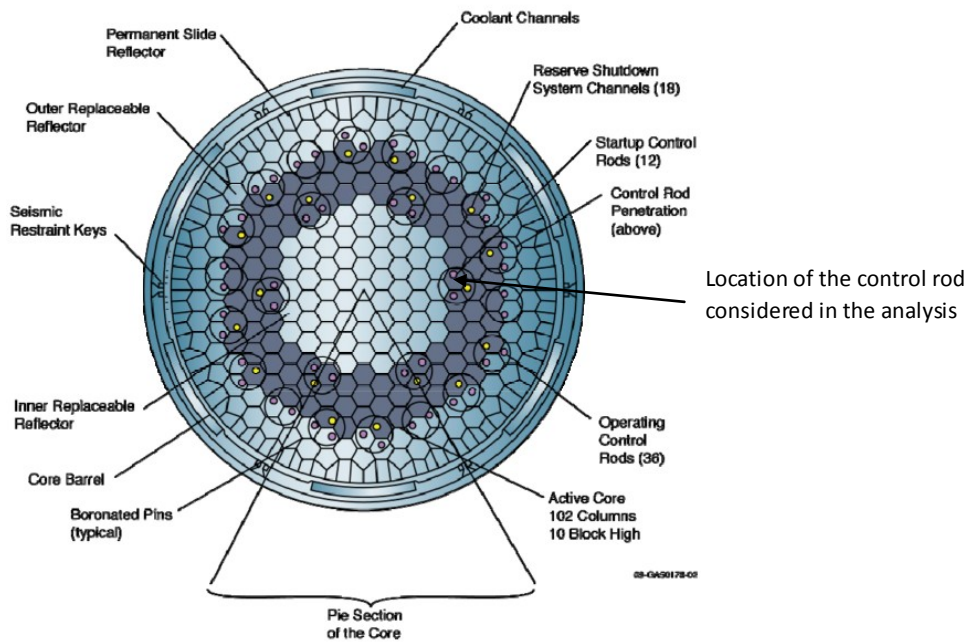

Figure 10.1: Location of the control rod considered for stress analysis (source: [3])

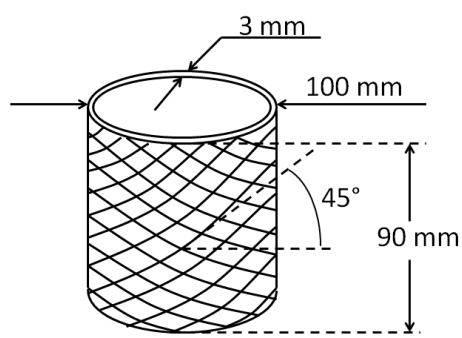

Figure 10.2: Schematic diagram of a composite control rod.

The constitutive relationship for an orthotropic composite material under the condition of plane stress is given as [1]:

$$\begin{bmatrix} \sigma_x \\ \sigma_y \\ \sigma_{xy} \end{bmatrix} = \begin{bmatrix} K_{11} & K_{12} & 0 \\ K_{12} & K_{22} & 0 \\ 0 & 0 & K_{33} \end{bmatrix} \begin{bmatrix} \varepsilon_x \\ \varepsilon_y \\ \gamma_{xy} \end{bmatrix}$$

where

$$K_{11} = \frac{E_x}{1 - \nu_{xy}\nu_{yx}}$$

$$K_{12} = \frac{\nu_{xy}E_y}{1 - \nu_{xy}\nu_{yx}} = \frac{\nu_{yx}E_x}{1 - \nu_{xy}\nu_{yx}}$$

$$K_{22} = \frac{E_y}{1 - \nu_{xy}\nu_{yx}}$$

$$K_{33} = G_{xy}$$

The values of the material properties used in performing the analysis are provided in Appendix. The properties in directions x and y were assumed to be equal. The stress analysis was performed using the user-defined subroutine UMAT developed earlier [4].

The control rod was meshed with 874 S4R (4-node doubly curved shell) elements as shown in Figure 10.3 (a). Figure 10.3 (a) also shows the boundary conditions on the model. The irradiation dose distribution was based on the operating conditions for a Prismatic fuel block as presented in [2]. Due to the unavailability of data regarding the dependence of composite properties on temperature, a uniform temperature distribution of 800°C was assumed in the control rod. Figure 10.3 (b) shows the local direction of fibers (1 and 2) in the composite control rod.

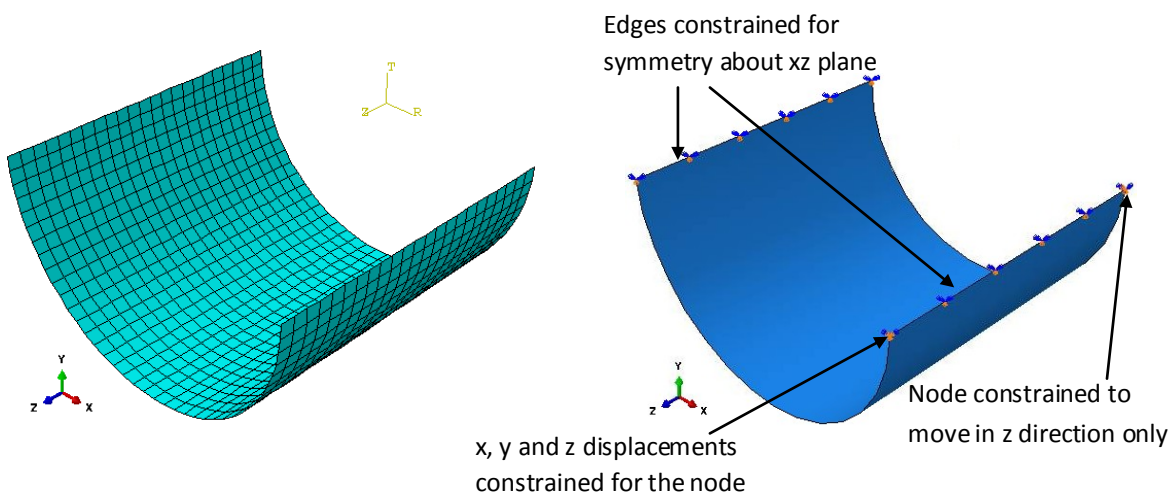

Figure 10.3 (a): Mesh of the FE model (left) and boundary conditions on the control rod (right).

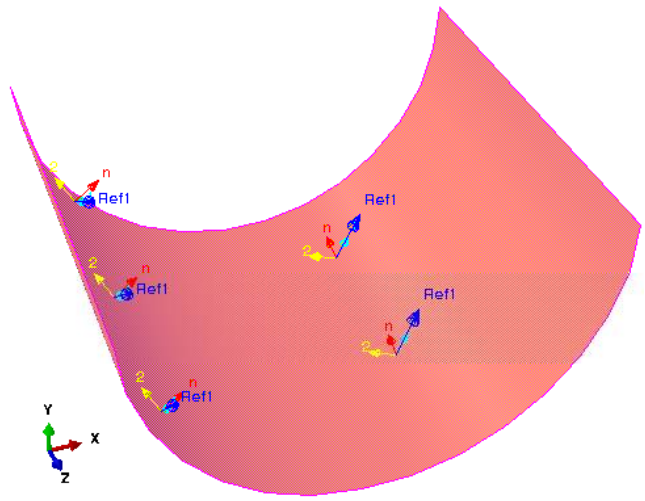

Figure 10.3 (b): Fiber directions 1 and 2 in the composite control rod (±45° from the axial direction and in the circumferential plane of the control rod)

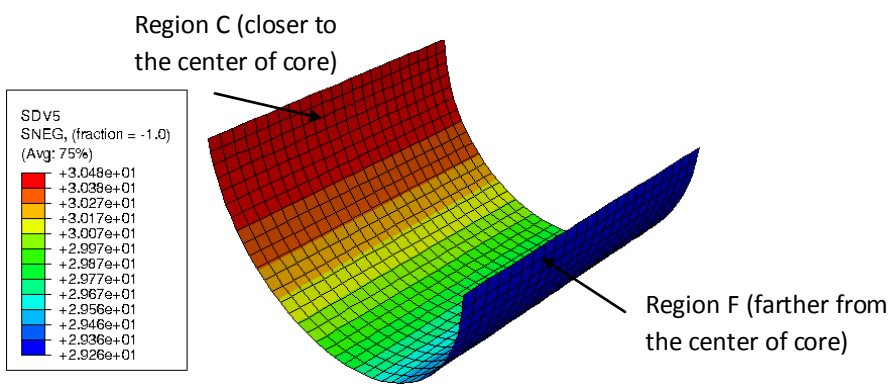

Figure 10.4: Irradiation dose distribution ($x10^{20}$ n/cm^2) in the prismatic reactor core brick at the end of 3.5 years.

The control rod was considered to be made of orthotropic SiC-SiC composite reinforced with Hi-Nicalon Type-S fibers. This particular composite has been found to be stable up to a dose level of 8 dpa while other composites (C/C composite and SiC/SiC composite with different reinforcement) lose their strength with an increase in dose [6]. The constitutive model for the composite included irradiation creep strain, thermal strain, dimensional change strain and elastic strain. Further details about the constitutive model are provided in [4]. The dimensional change strain and Young's modulus data were obtained from the work conducted by Newsome [2] (see Figure 10.5). The creep modulus was assumed to be a constant, 1.28×10^{-13} ($Pa\text{-}10^{20} n/cm^2$) based on [7]. The coefficient of thermal expansion was set as 4.4×10^{-6} /K [8]. Due to the unavailability of data for higher level of irradiation dose the analysis was performed for 3.5 years of reaction operation time.

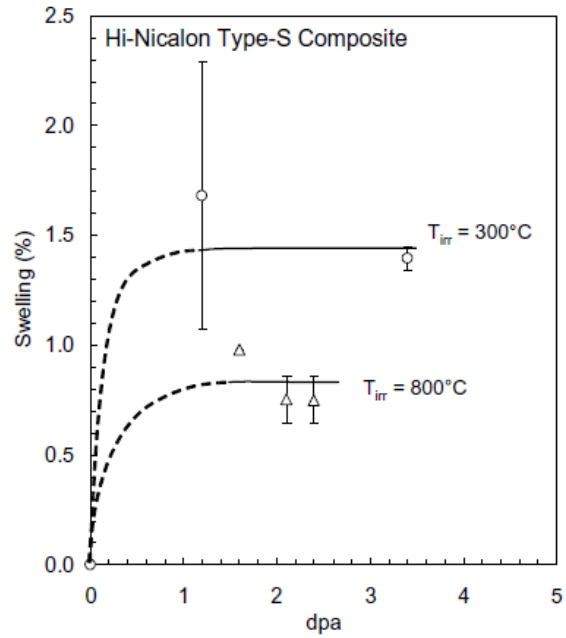

Figure 10.5: Swelling of SiC-SiC composite reinforced with Hi-Nicalon Type-S fibers under irradiation [2].

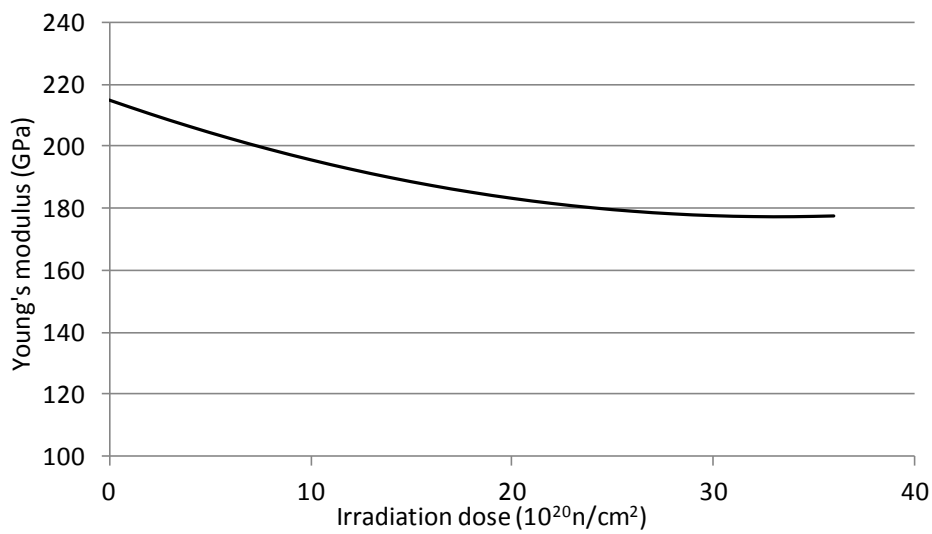

Figure 10.6: Variation of Young's modulus in x and y directions for SiC-SiC composite reinforced with Hi-Nicalon Type-S fibers under irradiation [2].

10.2.2 Results and Discussion

The finite element model was run in ABAQUS. Figure 10.7 (a) shows the distribution of stress in direction-1 (σ11) in the control rod at the end of 1, 1.9, 2.7 and 3.5 years (see Figure 10.3 (b) for directions). Figure 10.7 (b) shows the corresponding distribution of maximum principal stress in the

control rod. The variation of the maximum principal stress with time at three different locations in the control rod is shown in Figure 10.8.

The distribution of stress in Figure 10.7(a) shows stress-gradients both in the circumferential as well as axial direction. It can be also noted that in the beginning of reactor operation, a region C of the control rod, which is nearer to the center of the core, has compressive stresses and a region F, which is far from the center of the core, has tensile stresses (see Figure 10.4 for regions C and F). However, this distribution of stresses reverses after 1.9 years, i.e., region C of the control rod exhibits tensile stresses and region F shows compressive stresses.Figure 10.7 (b) shows that about 40-50% of the control rod had compressive stresses during the beginning of reactor operation and after about 2 years of operation.

Since the start of the reactor region C of the control rod accumulates greater irradiation dose and therefore expands more relative to region F. Region F restricts the expansion of region C which leads to the development of compressive stresses in region C. Later on, after about 1.5 years, the dimensional change strain (see Figure 10.5) and the compressive stresses in region C are relieved due to creep. Meanwhile, the region F of the control rod expands due to accumulated irradiation dose. The continued expansion in region F becomes greater than that in region C of the control rod. This leads to development of compressive stresses in region F and tensile stresses in region C. The greatest maximum principal stress during the reactor operation time of 3.5 years occurred soon after the start of the reactor (0.2 years) and was found to be 3 x 105 Pa; its location is shown in picture 1 of Figure 10.7 (b).

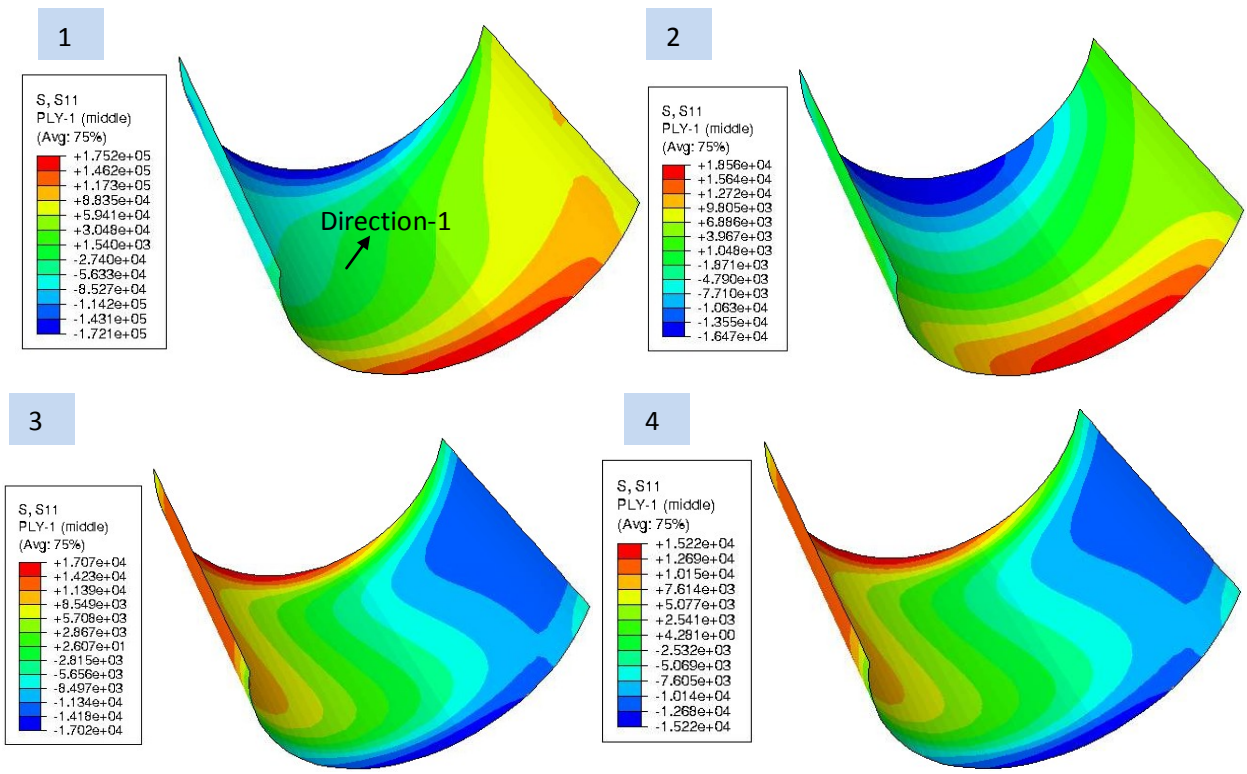

Figure 10.7 (a): Distribution of stress in direction-1 at the end of 1, 1.9, 2.7 and 3.5 years, shown in pictures numbered 1, 2, 3 and 4 respectively.

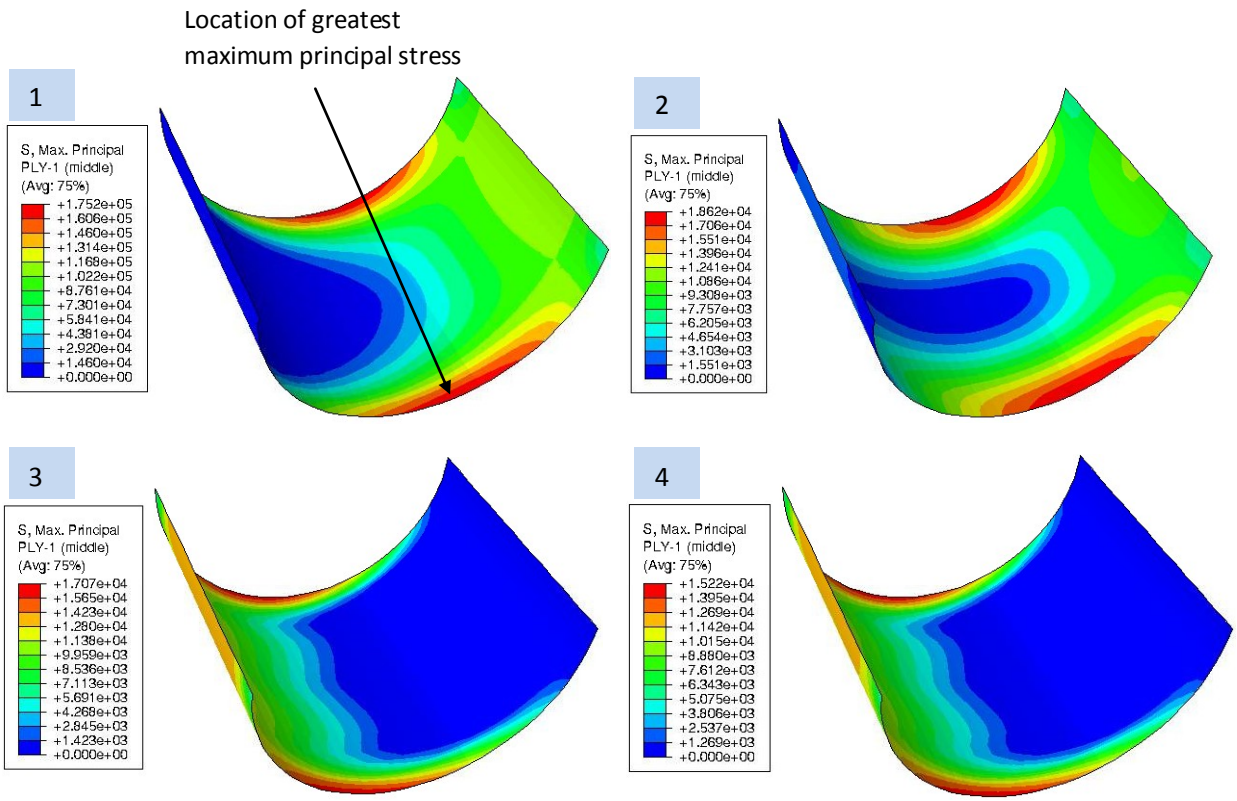

Figure 10.7 (b): Distribution of maximum principal stress at the end of 1, 1.9, 2.7 and 3.5 years, shown in pictures numbered 1, 2, 3 and 4 respectively.

Figure 10.8 shows the variation of the maximum principal stress with time at three different locations of the control rod. It can be noted that element C shows the greatest rise in the maximum principal stress. This can be attributed to its being located farthest to the core center and thus exposed to less irradiation dose than other elements. Elements B and C experience tension initially and undergo compression after about 2 years. It can also be noted that element A is in compression initially and undergoes tension after about 1.8 years.

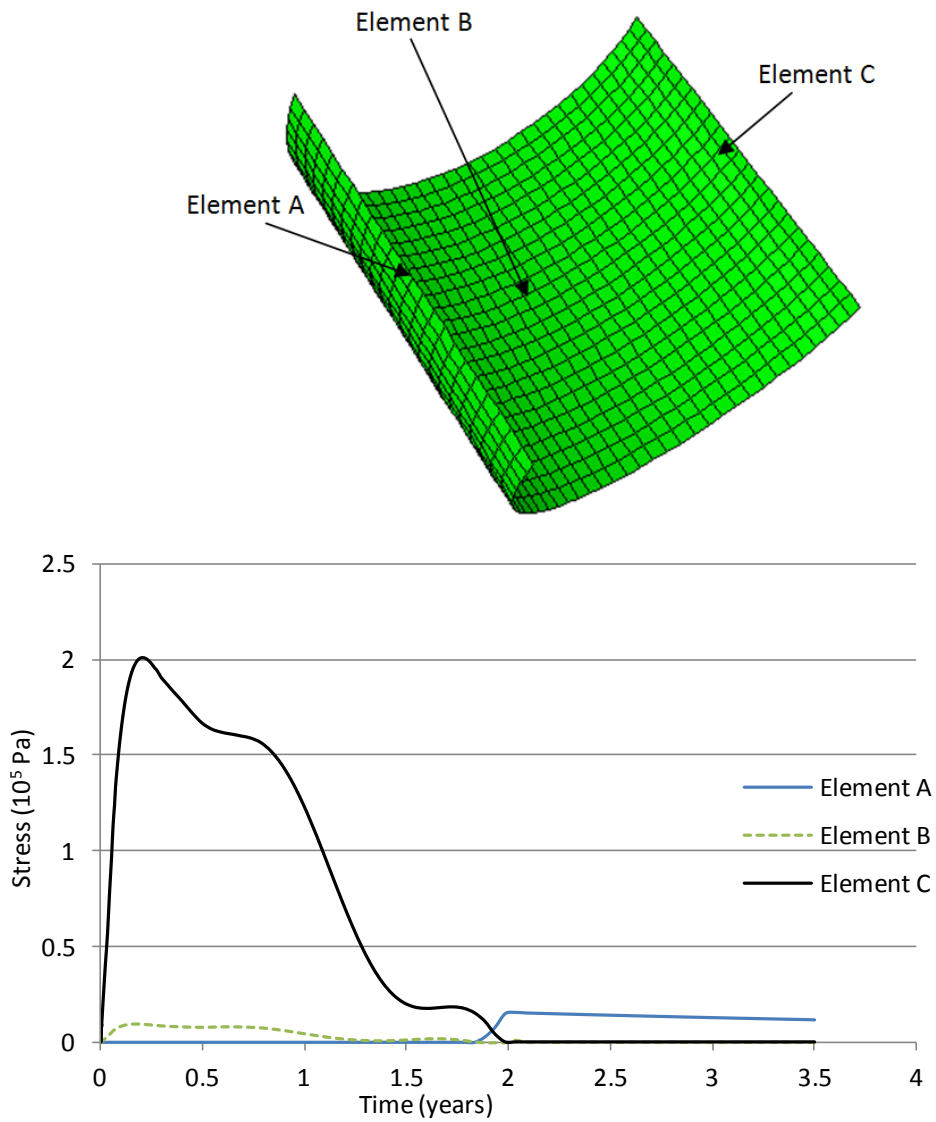

Figure 10.8: Variation of maximum principal stress with time at three different locations of the control rod.

10.2.3 Summary

Finite element analysis of a composite control rod was performed to evaluate the stress distribution and its variation with time. The operation time of 3.5 years was considered for the analysis. Stresses of the order of 10^5 Pa were found to develop in the rod. It was also observed that not only the magnitude of the stresses changed but the nature of the stresses also changed, i.e., compressive stresses turned tensile and vice versa in certain regions of the control rod.

10.3 REFERENCES

[1] Arun Shukla and James Dally, Experiemental Solid Mechanics, College House Enterprises, LLC.

[2] G. Newsome, L.L. Snead, T. Hinoki, Y. Katoh and D. Peters, Evaluation of Neutron Irradiated Silicon Carbide and Silicon Carbide Composites, Journal of Nuclear Materials, 371, 76-89, 2007.

[3] Modeling Mechanical Behavior of a Prismatic Replaceable Reflector Block, Robert L. Bratton, Idaho National Laboratory, Next Generation Nuclear Plant Project, INL/EXT-09-15868, 2009.

[4] Gyanender Singh, Haiyan Li, Alex Fok. Monte Carlo 3D Failure Analysis of a Prismatic Reactor Core Brick & Verification of UMAT for Predicting Behavior of a Composite Material Structure Under Irradiation, 11th quarterly report for NEUP-875: Failure Predictions for VHTR Core Components using a Probabilistic Continuum Damage Mechanics Model.

[5] Subhasish Mohanty, Rajeev Jain, Saurin Majumdar, Timothy J. Tautges and Maukateswara Srinivasan, Coupled Field Structural Analysis of HTGR Fuel Brick Using Abaqus, Proceedings of ICAPP' 12, Paper 12352, Chicago, USA, June 24-28, 2012.

[6] W.E. Windes, P.A. Lessing, Y. Katoh, L.L. Snead, E. Lara-Curzio, J. Klett, C. Henager, R.J. Shinavski, Structural Ceramic Composites for Nuclear Application, INL/EXT-05-00652, 2005.

[7] Enhanced Irradiation Creep in SiC: Data Summary and Planned Experiments, C.A. Lewinsohn, M.L. Hamilton, G.E. Youngblood, R.H. Jones, F.A. Garner, S.L. Hecht and A. Kohyama, J. Nucl. Mater. 253 36, 1998.

[8] http://homepages.cae.wisc.edu/~blanchar/

10.4 APPENDIX

Appendix A: VERIFICATION OF UMAT

γ: irradiation dose (10^{20}n/cm^2)
E_x : Young's modulus in the x direction (Pa)
E_y : Young's modulus in the y direction (Pa)
G_{xy} : modulus of rigidity (Pa)
ε^{dc} : dimensional change strain
ε^{th} : thermal strain
α: coefficient of thermal expansion of irradiated composite (/°C)
α_o: coefficient of thermal expansion of un-irradiated composite (/°C)
ΔT: difference in the temperature of the composite from room temperature (°C)

$E_x = 100\text{x}10^9(1+0.25 \text{ x } (2-\gamma/50) \text{ x } \gamma/50)$
$E_y = 50\text{x}10^9(1+0.25 \text{ x } (2-\gamma/50) \text{ x } \gamma/50)$
$G_{xy} = 30\text{x}10^9(1+0.25 \text{ x } (2-\gamma/50) \text{ x } \gamma/50)$

$\varepsilon_x^{dc} = -9.033 \times 10^{-12} \times \gamma^4 + 6.812 \times 10^{-9} \times \gamma^3 - 6.397 \times 10^{-7} \times \gamma^2 - 2.077 \times 10^{-4} \times \gamma$

$\varepsilon_y^{dc} = (-9.033 \times 10^{-12} \times \gamma^4 + 6.812 \times 10^{-9} \times \gamma^3 - 6.397 \times 10^{-7} \times \gamma^2 - 2.077 \times 10^{-4} \times \gamma)/2$

$\alpha_x = 4.65 \times 10^{-6} \times (1 - 2.804 \times 10^{-10} \times \gamma^4 + 3.023 \times 10^{-7} \times \gamma^3 - 9.676 \times 10^{-5} \times \gamma^2 + 8.345 \times 10^{-3} \times \gamma)$

$\alpha_y = 2.32 \times 10^{-6} \times (1 - 2.804 \times 10^{-10} \times \gamma^4 + 3.023 \times 10^{-7} \times \gamma^3 - 9.676 \times 10^{-5} \times \gamma^2 + 8.345 \times 10^{-3} \times \gamma)$

$d\varepsilon^{th} = d\alpha\ (\Delta T)$

Appendix B: ANALYSIS OF CONTROL ROD

ΔT: change in temperature

ν_{xy} , ν_{yx}: Poisson's ratios

$\nu_{xy} = \nu_{yx} = 0.16$

$E_x = (0.034\gamma^2 - 2.259\gamma + 215) \times 10^9$

$E_y = (0.034\gamma^2 - 2.259\gamma + 215) \times 10^9$

$G_{xy} = 4.617 \times 10^{10}$

$\varepsilon^{th} = \alpha\Delta T$

$\varepsilon^{dc} = q1\ \gamma^6 + q2\ \gamma^5 + q3\ \gamma^4 + q4\ \gamma^3 + q5\ \gamma^2 + q6\ \gamma)/3$ (γ<=12, T=300C)

$= 0.005$ (γ>12, T=300C)

$= (p1\ \gamma^8 + p2\ \gamma^7 + p3\ \gamma^6 + p4\ \gamma^5 + p5\ \gamma^4 + p6\ \gamma^3 + p7\ \gamma^2 + p8\ \gamma)/3$ (γ<=17, T=800C)

$= 0.00272$ (γ>17, T=800C)

Values of constants in the polynomial:

p1 = -1.554e-11;	p2 = 1.691e-09;
p3 = -7.634e-08;	p4 = 1.858e-06;
p5 = -2.655e-05;	p6 = 0.0002287;
p7 = -0.001199;	p8 = 0.003979;
q1 = -3.693e-08;	q2 = 1.993e-06;
q3 = -4.323e-05;	q4 = 0.0004831;
q5 = -0.002959;	q6 = 0.009756;